



Mohamed Khider University of Biskra
Faculty of Exact Sciences and Natural and Life Sciences
Material Sciences Department

MASTER MEMORY

Field of Material Sciences

Physics

Specialty : Energetic Physics and Renewable Energies

Réf. : Entrez la référence du document

Presented by:
Ben Dagga Kamilia

Le : 27/6/2022

Study of Schottky barrier solar cell based on $\text{Cu}(\text{In}, \text{Ga})\text{Se}_2$ (CIGS) material.

Jury:

Mr	Meftah Afak	Professor	M ^{ed} Khider University of Biskra	President
Mse	Meftah Amjad	Professor	M ^{ed} Khider University of Biskra	Supervisor
Mse	Laznek Samira	MCB	M ^{ed} Khider University of Biskra	Examiner

Academic Year: 2021/2022

Acknowledgement

First and foremost, praises and thanks to “ALLAH”, the Almighty, for His showers of blessings throughout my research work to complete the research successfully.

*I would like to thank my advisor **Pr. Meftah Amjad** for his valuable guidance and support during my dissertation and I am benefited a lot from her profound knowledge.*

*I would not forget to thank the members of the jury, **Dr. Meftah Afak** and **Dr. Laznek Samira** who have kindly accepted to read and examine our work.*

I also thank my family and my friends

Finally, my thanks go to all the people who have supported me to complete the research work directly or indirectly.

Dedication

I dedicate this work:

*I am extremely grateful to my parents “**Ben dagga lakhder**” and “**Souici tourkia**” for their love, prayers, caring and sacrifices for educating and preparing me for my future.*

*I also thank my brothers (**Mahdi , Hittal, Masoud, Rabeh, Isbat, Firas, Aderian**), and my only sister (**Zahra**).*

*I would like to thank my husband ‘**khaled**’*

*and I thank my friends (**Ahlam , Asma, Khadidja , Chaima, Kaouthar, djamila chawk, sana,**)*

KAMILIA

Abstract

We have investigated a Schottky barrier solar cell based on n-type CIGS material. The anode metal; situated on the top of the cell, satisfy the Schottky contact condition. The cathode (Al), however, is defined to be Ohmic contact. Two samples were investigated; in the sample (A), the cathode is situated on the bottom of the cell, and in sample (B), the two cathode electrodes are located on the top of the cell. With using platinum (Pt) as anode metal ($\phi_m = 6.35 \text{ eV}$), the cell thickness increase in the range $[0.5- 8\mu\text{m}]$ showed an optimal conversion efficiency η around 21,98% for the sample (B) with thickness $d \sim 3\mu\text{m}$, for the sample (A), the better η is around 27,48 % for a thickness more larger ($d \sim 8 \mu\text{m}$). The doping concentration effect of the CIGS base layer (N_d) in the range $[10^{12} - 10^{19} \text{ cm}^{-3}]$, with the cell thickness d of $1.2 \mu\text{m}$, showed an optimal value of doping $N_d \cong 10^{15} \text{ cm}^{-3}$ which provided a conversion efficiency $\eta \cong 20.48\%$ for sample (A), and $\eta \cong 21.80\%$ for sample (B). Three choices were considered for the anode metal: Pt ($\phi_m = 6.35 \text{ eV}$), Au ($\phi_m = 5.47 \text{ eV}$) and Ni ($\phi_m = 5.22 \text{ eV}$), showing that the cell approached the ideal case of p⁺-n junction for the first choice. The second choice made the cell operating as standard Schottky barrier solar cell. The third choice, however, was the worst choice because it reduced significantly the solar cell performances.

List of figures

Figure number	Titles	Page number
I.1	PN junction fabrication by converting a layer of P-type semiconductor into N type with donor impl	4
I.2	The rectifying <i>IV</i> characteristics of a PN junction [10].	4
I.3	Band scheme representation of PN junction [11].	5
I.4	Solar cell work principle.	6
I.5	Solar irradiance spectrums versus wavelength [16]	8
I.6	(a) Light can produce a current in PN junction at $V = 0$. (b) Solar cell <i>IV</i> product is negative, indicating power generation [19]	9
I.7	Ideal solar cell.	10
I.8	Photovoltaic cell equivalent circuit.	10
I.9	$J - V$ curves characteristic of solar cells [23]	11
I.10	<i>EQE</i> graph for different materials used in solar cells [27]	14
I.11	Schematic diagram of a Schottky junction solar cell showing the flow of electrons to the external load represented by the green rectangle adapted from [30]. Photon of light shone at the metal and semiconductor junction to facilitate electron flow	15
I.12	Simplified band diagram of a metal and n-type semiconductor Schottky solar cell depicting the thermionic emission across the Schottky junction under illumination condition adapted and drawn from [30].	16
I.13	The energy band diagram of metal/n-type semiconductor junction which reveals the band bending process after the metal semiconductor junction comes into contact adapted from [32]	17
I.14	Metal and n-type Schottky junction solar cells in positive DC voltage bias and negative DC voltage bias conditions on the left and the right respectively Adapted from [32]	19
I.15	Types of photovoltaic solar cells [14]	22
II.1	Chalcopyrite crystal structures of CIGS [after 60]	26
II.2	Band-gap energies (E_g) vs. the lattice constant (a) of the Cu(In, Ga,Al)(S, Se) ₂ alloy system [59].	27
II.3	Different types of absorber band gap profiles:(a) Uniform band gap, (b) Front grading (Space charge region grading),(c) back surface grading, (d) Double grading [57]	29
II.4	Standard layer structure of CIGS solar cells, layers not at scale [67]	30

II.5	Schematic diagram of :(a) CIGS-based Schottky barrier solar cell, (b) the corresponding band diagram under sunlight illumination and zero bias.	32
III.1	Screenshot from Deckbuild	35
III.2	Atlas statement hierarchy, from [82,p.34].	36
III.3	Mesh example for Schottky barrier solar cell based on n-type CIGS material	37
III.4	Tonyplot screenshot showing the layout of the x and y-coordinate system in Atlas for Schottky barrier solar cell based on n-type CIGS material.	39
III.5	Electrode positions of the Schottky barrier solar cell based on n-type CIGS material	40
III.6	Simulated $J - V$ characteristics of the Schottky barrier solar cell based on n-type CIGS material, in the dark and illumination conditions with AM1.5 spectrum	46
III.7	Simulated $P - V$ characteristics of the Schottky barrier solar cell based on n-type CIGS material, in illumination conditions with AM1.5 spectrum	46
IV.1	Structure of the Schottky barrier solar cell based on CIGS : (a) sandwich configure (sample A), (b) coplanar configuration (sample B)	48
IV.2	Two dimensional (2D) mesh of the Schottky barrier solar cell based on CIGS: (a) sandwich configure (sample A), (b) coplanar configuration (sample B)	49
IV.3	Optical spectre of: (a) absorption coefficient (α) and (b) index of refraction (n) in the different layers of the studied Schottky barrier solar cell based on CIGS	50
IV.4	Local tunneling generation rate representation of the universal Schottky tunneling model [82]	53
IV.5	Band diagram of the Schottky barrier solar cell based on CIGS (sample A)with platinum (Pt) anode metal ($\phi_m = 6.35 eV$): (a) at thermal equilibrium, (b) at short circuit condition	55
IV.6	Carrier density distributions in the Schottky barrier solar cell based on CIGS (sample A) at thermal equilibrium and short circuit condition	56
IV.7	Simulated $J - V$ and $P - V$ characteristics of the Schottky barrier solar cell based on CIGS with platinum (Pt) anode metal ($\phi_m = 6.35 eV$), under the AM1.5 standard spectrum and $T = 300^{\circ}K$: (a) sample (A), (b) sample (B)..	57
IV.8	Photovoltaic output parameters evolution with the cell thickness increase for the two samples (A) and (B) of the simulated Schottky barrier solar cell based on CIGS	58

IV.9	Doping concentration effect of the CIGS base layer on the photovoltaic output parameters of the simulated Schottky barrier solar cell with (Pt) anode metal for the two samples (A) and (B).	60
IV.10	Doping concentration effect of the CIGS base layer on the photovoltaic output parameters of the simulated Schottky barrier solar cell (sample B) for three cases of the anode metal: Pt ($\phi_m = 6.35 \text{ eV}$), Au ($\phi_m = 5.47 \text{ eV}$) and Ni ($\phi_m = 5.22 \text{ eV}$).	63

List of Tables

Table number	Titles	Page number
I.1	Current state of the art single junction solar cells [51]	24
IV.1	Brief description of the employed models in simulation[82]	51
IV.2	Input parameters of the studied Schottky barrier solar cell based on CIGS simulated by Silvaco-Atlas [82]	52
IV.3	Comparison between the photovoltaic output parameters of the samples (A) and (B) of the simulated Schottky barrier solar cell based on CIGS with platinum (Pt) anode metal ($\phi_m = 6.35 \text{ eV}$).	58
IV.4	Photovoltaic output parameters evolution with the cell thickness increase for the two samples (A) and (B) of the simulated Schottky barrier solar cell based on CIGS.	59
IV.5	Doping concentration effect of the CIGS base layer on the photovoltaic output parameters of the simulated Schottky barrier solar cell with (Pt) anode metal for the two samples (A) and (B).	60
IV.6	Doping concentration effect of the CIGS base layer on the photovoltaic output parameters of the simulated Schottky barrier solar cell (sample B) for three cases of the anode metal: Pt ($\phi_m = 6.35 \text{ eV}$), Au ($\phi_m = 5.47 \text{ eV}$) and Ni ($\phi_m = 5.22 \text{ eV}$).	64
IV.7	Estimation of the thermionic emission current density (J_{th}) versus the Schottky barrier height (ϕ_B)	64

List of Symbols

Symbol	Definition	Unit
E	Photon energy	eV
I_s	The diode saturation current	A
V	the voltage of the cell	V
K	Boltzmann constant	$(J/^\circ K)$
T	Absolute temperature	$^\circ K$
I_L	The photo-generation current	A
q	Electron Charge	C
E_g	band-gap energy of the semiconductor	eV
η	Conversion efficiency	%
n	the refractive index	–
P_{in}	the input power	$mW.cm^{-2}$
V_{mp}	The maximum power point voltage	V
I_{mp}	The maximum power point current	A
FF	Fillfactor	%
E_C	Conduction band energy edge	eV
E_V	Valence band energy edge	eV
E_f	Fermi level	eV
h	The Planck constant	$(J.S)$
J_{ph}	The density of the photo-current	(A/cm^2)
J_{sc}	Short circuit current density	(A/cm^2)
V_{oc}	Open circuit voltage.	Volt
ν	Wave frequency	Hz
I	Current supplied by the photovoltaic cell	A
I_{SH}	Current through shunt resistance	A
P_{max}	Maximum power	W
x_{tot}	Cell width	μm
R_s	Series resistance	Ω
R_{SH}	Shunt (parallel) resistance	Ω
α	the absorption coefficient	cm^{-1}
χ_{sc}	Electron affinity of semiconductor	eV
μ_n	Electron mobility	$cm^2V^{-1}s^{-1}$
μ_p	Hole mobility	$cm^2V^{-1}s^{-1}$
ϕ_m	Work function of the metal	eV
ϕ_b	Schottky barrier height	eV
N_d	the density of donors in the n-type semiconductor	cm^{-3}

CdTe	Cadmium Telluride	-
CIGS	Copper-Indium-Gallium-Selenide	-
AM 1.5	Standard terrestrial solar spectrums 'Air Mass 1.5'	-

Table of contents

<u>Acknowledgement</u>	II
<u>Dedication</u>	III
<u>Abstract</u>	IV
<u>List of figures</u>	V
<u>List of tables</u>	VIII
<u>List of symbols</u>	IX
<u>General introduction</u>	1
Chapter I : Photovoltaic and solar cells	
I.1.Introduction.....	3
I.2.Photovoltaic effect.....	3
I.2.1.PN junction.....	3
I.2.2.Solar cells.....	6
I.2.3.Solar radiation.....	7
I.2.4.Characteristics of a PN junction solar cell.....	8
I.2.5.Equivalent electrical circuit of a solar cell.....	10
I.2.6.Figures of merit of a solar cell.....	11
I.2.6.1.Short circuit current (I_{sc}).....	12
I.2.6.2.Open-circuit voltage (V_{oc}).....	12
I.2.6.3.The maximum power (P_{max}).....	12
I.2.6.4.Fill factor (FF).....	12
I.2.6.5.Power conversion efficiency (η).....	13
I.2.6.6.The quantum efficiency.....	13
I.3.Schottky barrier solar cell.....	14

I.4. Generations of solar cells.....	20
I.4.1. First Generation solar cells.....	20
I.4.2. Second Generation solar cells.....	20
I.4.3. Third Generation solar cells.....	21
I.4.4. Fourth-generation solar cells.....	21
I.5. Different types of solar cells.....	21
I.5.1. Silicon semiconductor type solar cells.....	21
I.5.1.1. Monocrystalline solar cell.....	22
I.5.1.2. Polycrystalline solar cell.....	22
I.5.1.3. Amorphous solar cell.....	23
I.5.2. Other types of solar cell.....	23
I.6. Thin film solar cells	23

Chapter II: CIGS-based solar cells

II.1. Introduction.....	25
II.2. CIGS material properties.....	25
II.2.1. Structural and Compositional Properties.....	25
II.2.2. Optical Properties and Band Gap Grading.....	27
II.3. The conventional (standard) CIGS solar cell structure.....	29
II.4. Schottky barrier solar cell based on CIGS material.....	31

Chapter III : Silvaco-Atlas Software

III.1. Introduction.....	33
III.2. Numerical modelling software SILVACO-ATLAS.....	33
III.3. DECKBUILD.....	34
III.4. Main steps of the numerical simulation of Schottky barrier solar cell based on CIGS material using Silvaco-Atlas.....	36
III.4.1. Building the device.....	36
III.4.2. Defining the Structure.....	37

III.4.3.Regions.....	38
III.4.4.Electrodes.....	39
III.4.5. Doping.....	41
III.4.6.Modifying Parameters	41
III.4.7.Numerical Solutions.....	41
III.4.8.Obtaining Solutions.....	42
III.4.9.Results.....	43
III.4.10.Tonyplot.....	43
III.4.11.Luminous.....	44
III.4.12.Solar cell simulation.....	44
Chapter IV :Study Of Schottky Barrier Solar Cell Based On CIGS Material	
IV.1.Introduction.....	47
IV.2. Description of the studied Schottky barrier solar cell based on CIGS.....	47
IV.3.Schottky Contact and the Universal Schottky Tunneling (UST) Model.....	53
IV.4. Results and discussion.....	54
IV.5.Conclusion.....	65
General conclusion.....	67
References.....	70
Abstract.....	78
ملخص.....	79

General introduction

General introduction

Thin-film solar cells are considered the second generation of photovoltaics, they are expanding in the photovoltaic market due to their competitive cost with the traditional silicon cell [1]. This is due to the thin-film using less material than the silicon solar cells. In order to absorb the same amount of sun light the silicon solar cell requires 100–200 μm of material and the thin-film solar cells only requires a few micrometers of material [1].

The group I-III-VI chalcopyrite $(\text{Ag,Cu})(\text{In,Ga})(\text{S,Se})_2$ semi-conductor alloys, commonly known as CIGS, are particularly suitable absorber materials for solar cells. Their direct band gaps range from ~ 1 to 2.7 eV [2], they are advantageous for application in multi junction solar cells, since the gap of the different layers can be tuned by varying the ratio of In and Ga, and/or S and Se. They have high absorption coefficients and favourable intrinsic defect properties that enable high minority carrier lifetimes, and solar cells the refrom are intrinsically stable in operation [2]. Their first reported efficiency was a 12% single-crystal device in the mid 1970 s[3]. Subsequently, CIGS thin-film absorbers, processing, and contacts have improved dramatically, yielding 23.3% small-area thin-film cells [4,5].

In this study, we will investigate the Schottky barrier solar cell based on n-type Copper Indium Gallium Selenide $(\text{Cu}(\text{In,Ga})\text{Se}_2$: CIGS) material, exposed to the AM1.5 standard spectrum at ambient temperature (300 $^\circ\text{K}^\circ$) . The anode metal, situated on the top of the cell, should satisfy the Schottky contact condition by having a work function (ϕ_m) higher than the electron affinity (χ_{sc}) of the semiconductor (n-type CIGS).The metals used in this study to satisfy this condition are respectively Pt ($\phi_m = 6.35$ eV), Au ($\phi_m = 5.47$ eV) and Ni ($\phi_m = 5.22$ eV) [6].The cathode (Al) is defined to be neutral (Ohmic contact). Two solar cells will be considered in this study; for the first one (sample A), the cathode is situated on the bottom of the cell giving a sandwich configuration. For the second one (sample B), two cathode electrodes are located on the top of the cell giving a coplanar configuration. The investigation will be achieved using the numerical simulation software SILVACO-ATLAS, which allows the calculation of all the internal parameters of the solar cell such as the distribution of the band diagram, the electron and holes concentrations...etc. The external parameters will also be calculated such as the current

density-voltage ($J - V$) and the provided power – voltage ($P - V$) characteristics under illumination, which allow the extraction of the photovoltaic output parameters of the solar cell namely the short circuit current density J_{sc} , the open circuit voltage V_{oc} , the fill factor FF , the maximum power P_{max} provided by the cell and the photovoltaic conversion efficiency η of the cell. For the two considered solar cells, we will investigate the thickness variation effect of the n-type CIGS layer in the range [0.5- 8 μ m], the n-type doping concentration (N_d) effect of the CIGS layer in the range [$10^{12} - 10^{19}cm^{-3}$], and the work function (ϕ_m) effect by changing the anode metal (Pt, Au and Ni).

In addition to the general introduction and conclusion, the thesis is organized in four chapters as follow:

In chapter I, we will give an introductory overview of the important concepts in photovoltaic. It ranges from the basic solar cell functioning to the different technologies of solar cells. The characteristics of the solar cell based on PN junction and Schottky barrier junction will also be presented.

In chapter II, we will give a short overview on the present knowledge of CIGS-based thin film solar cells. We will focus on three points: (i) Description of the basic material properties such as crystal and optical properties. (ii) Description of the classic (standard) CIGS solar cell structure. (iii) Description of the Schottky barrier solar cell based on n-type CIGS material.

In chapter III, we will present a description of Silvaco-Atlas simulation software; which we will use to investigate the electrical characteristics of the Schottky barrier solar cell based on CIGS material.

In chapter IV, we will present a detailed description of the investigated Schottky barrier solar cell based on n-type CIGS material, then, we will present and discuss the main results obtained in our study.



Chapter I :

Photovoltaic and Solar Cells

I.1.Introduction

Solar energy is the most promising source of energy of modern area. It has a biggest advantage over the conventional power generation systems that the sunlight can be directly converted into solar energy with the help of solar cells. This type of electrical energy production methods is cost effective, generates no toxic materials and follows green approach. The sun light can easily compensate the energy drawn from the non-renewable sources of energy such as fossil fuels and petroleum deposits inside the earth. The fabrication of solar cells has passed through a large number of improvement steps from one generation to another. Silicon based solar cells were the first-generation solar cells grown on Si wafers, mainly single crystals. Further development to thin films, dye sensitized solar cells and organic solar cells enhanced the cell efficiency. The development is hindered by the cost and efficiency [7, 8].

This chapter gives an introductory overview of the important concepts in photovoltaic. It ranges from the basic solar cell functioning to the different technologies of solar cells. The characteristics of the solar cell based on PN junction and Schottky barrier junction are also presented.

I.2.Photovoltaic effect

The photovoltaic effect is the process by which sunlight is converted into electrical energy. This occurs when a semiconducting material absorbs a photon's energy and generates an electron-hole pair. If the photon's energy is sufficiently large, the charge carriers will move to a higher energy state. Semiconducting materials arranged as a p-n junction collect these energetic charge carriers and facilitate their movement as electrical current. This is the process by which all photovoltaic solar cells operate. Mastery of this process has had a profound impact on global energy generation. The Cu(In,Ga)Se_2 or CIGS thin-film solar cell, through advances in device characterization, processing, and materials, has achieved photovoltaic conversion efficiency of over 22% [9].

I.2.1.PN junction

As illustrated in Figure I.1, a PN junction can be fabricated by implanting or diffusing

donors into a P-type substrate such that a layer of semiconductor is converted into N type. Converting a layer of an N-type semiconductor into P type with acceptors would also create a PN junction [10].

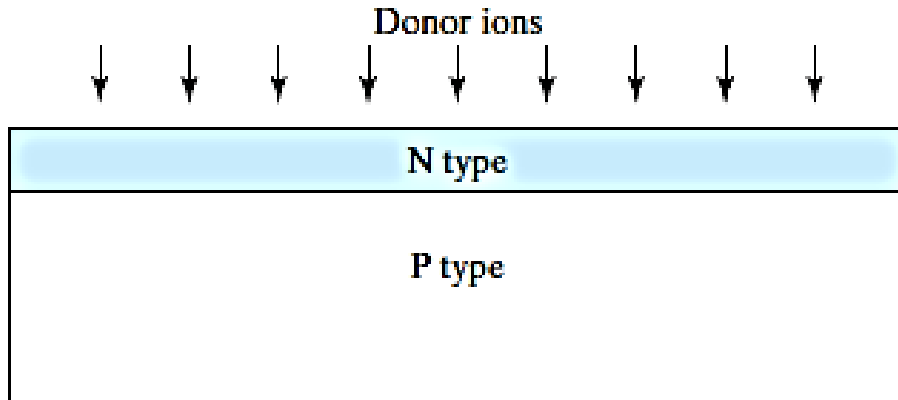


Figure I.1: PN junction fabrication by converting a layer of P-type semiconductor into N-type with donor implantation or diffusion [10].

A PN junction has rectifying current–voltage (I – V or IV) characteristics as shown in Figure I.2.

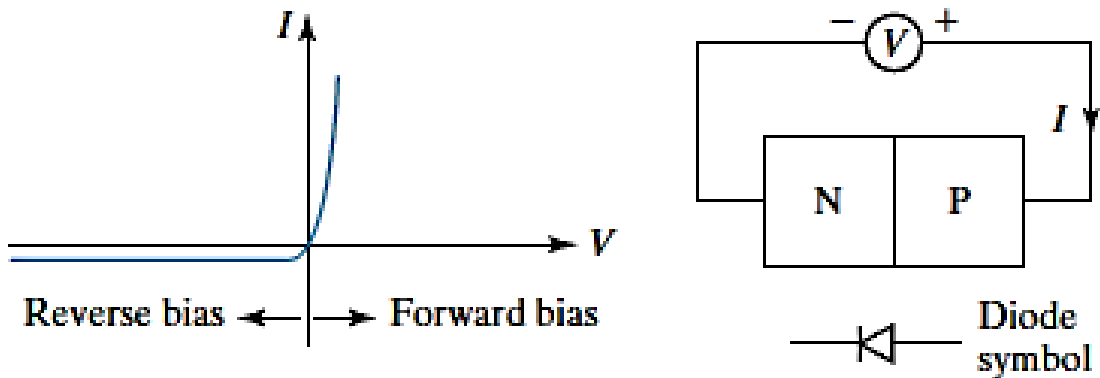


Figure I.2: The rectifying IV characteristics of a PN junction [10].

As a device, it is called a rectifier or a diode. The PN junction is the basic structure of solar cell, light-emitting diode, and diode laser, and is present in all types of transistors. In addition, PN junction is a vehicle for studying the theory of the depletion layer, the quasi-equilibrium boundary condition, the continuity equation, and other tools and concepts that are important to the understanding of electronic and optoelectronic devices [10].

Using special technological processes as said above, we can assemble two semiconductor materials; one P-type doped, and the other N-type doped, to obtain the so-called PN junction, like presented in Figure I.3.

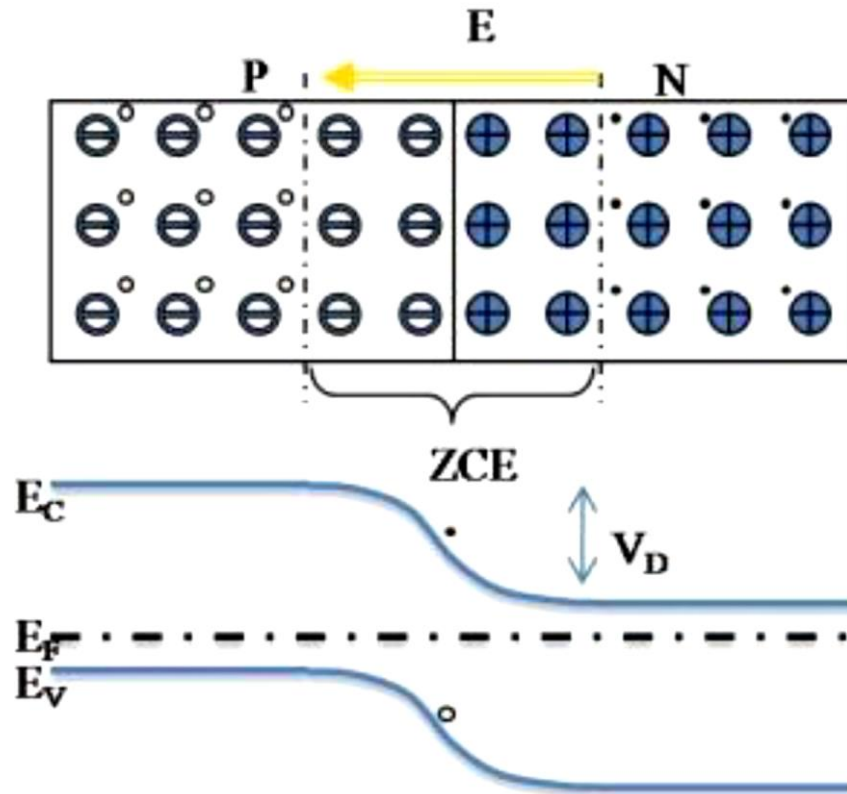


Figure I.3: Band scheme representation of PN junction [11].

When the two types of semiconductors come into contact, a concentration gradient of charge carriers is created between the two materials. Electrons from the n-type material migrate to the p-type material and combine with holes, leaving behind a positively charged ion. Holes from the p-type material migrate to the n-type material to combine with electrons, leaving behind negatively charged ions (Figure I.3). This is known as diffusion current. The accumulation of charged ions in each material creates an electric field which is referred to as the "built-in field". The region the built-in field extends over is called the space-charge region (SCR). The SCR is stabilized when the drift current caused by the built-in field equals the diffusion current. The Fermi level (E_F) alignment at thermal equilibrium induces the band bending and a potential barrier (V_D) is established [11].

There are two types of PN junctions:

- Step junction (step junction): the transition from the P-type region to the N-type region 'takes place on an infinitely fine thickness.

- Gradual junction (linearly graded junction): the transition from the P-type region to the N-type region takes place according to a linear law [12].

Shockley's equation explains the general characteristics of forward and reverse biasing regions of diode [13]. The diode current equation is given as:

$$I_D = I_S \left[\exp\left(\frac{qV_D}{nk_B T}\right) - 1 \right] \quad (\text{I.1})$$

where I_D is the diode current, I_S is reverse saturation current, V_D is diode voltage, n is semiconductor constant, depends on the construction and operating conditions (1 to 2, usually taken as 1), k_B is Boltzmann's constant, T is absolute temperature in kelvin and q is magnitude of electronic charge [14].

I.2.2.Solar cell

The heart of the solar energy generation system is the solar cell which is a device that converts the sunlight energy into electrical energy through the photovoltaic effect (Figure I.4).

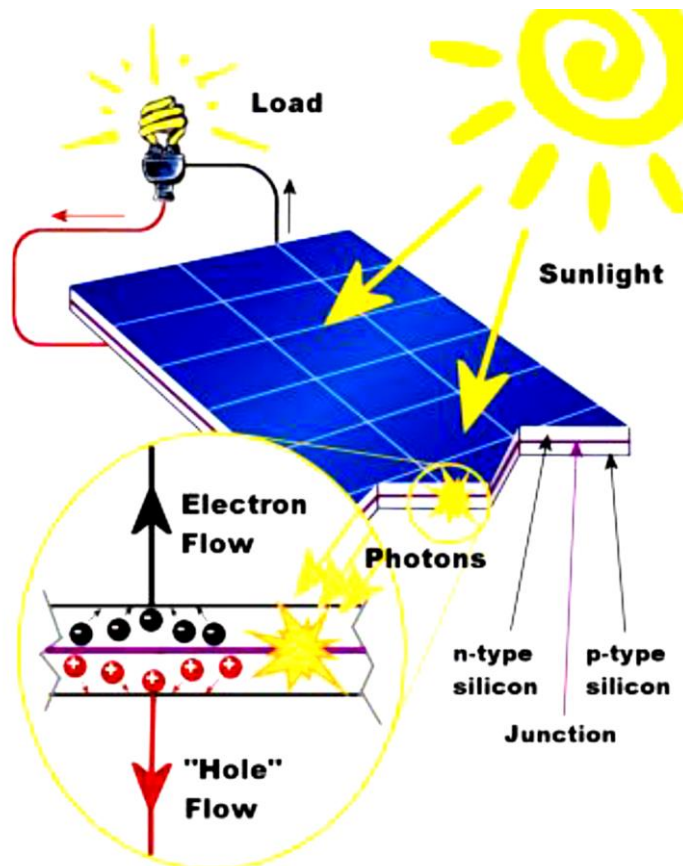


Figure I.4: Solar cell work principle.

Solar cell consists of three major elements namely [15]:

- 1-The semiconductor material which absorbs photons (whose energy is greater than the gap) and generates an electron–hole pair.
- 2- The junction formed with in the semiconductor, which separates the photo-generated carriers (electrons and holes) electrons to the negative terminal and holes to the positive terminal.
- 3- The contacts on the front and back of the cell that allow the current to flow to the external circuit.

When the sunlight hits the semiconductor surface, an electron springs up and is attracted to wards the N-type semiconductor material. This will cause more negatives in the N-type and more positives in the P-type semiconductors, generating a higher flow of electricity. This is known as Photovoltaic effect. The amount of current generated by a Photovoltaic (PV) cell depends on its efficiency, its size (surface area) and the intensity of sunlight striking the surface. For example, under peak sunlight conditions a typical commercial PV cell with a surface area of about 25 square inches will produce about 2 watts peak power [15].

I.2.3.Solar radiation

A solar cell having a PN junction or Schottky barrier structure can convert sunlight directly into electricity. Precise incident solar irradiance power under different conditions are used for the calculation of power conversion efficiency of a solar cell [16]. The radiant energy particularly electromagnetic energy emitted by the sun is solar radiation [17]. Figure I.5 illustrates the solar irradiance spectra for two air-mass (*AM*) conditions [14].The upper curve is the *AM0* solar irradiance spectrum and is measured above the earth's atmosphere. Under *AM0* conduction the irradiant power of the sun is $136.61\text{mW}/\text{cm}^2$. The lower curve is the *AM1* solar irradiance spectrum characterizes the sunlight on the earth's surface when the sun is at its zenith angle. Under *AM1* condition total incident power of sunlight $92.5\text{ mW}/\text{cm}^2$. *AM1.5G* (global) is the standard spectrum at the earth's surface. *AM1.5G* spectrum ($\theta = 48.2^\circ$) has been normalized to give $100\text{mW}/\text{cm}^2$. For the calculation of solar cell power conversion efficiency in the terrestrial environment, *AM1.5G* spectrum is the most suitable incident solar irradiance. To calculate the power

conversion efficiency of the solar cell, specifying the exact *AM* condition is very important [16].

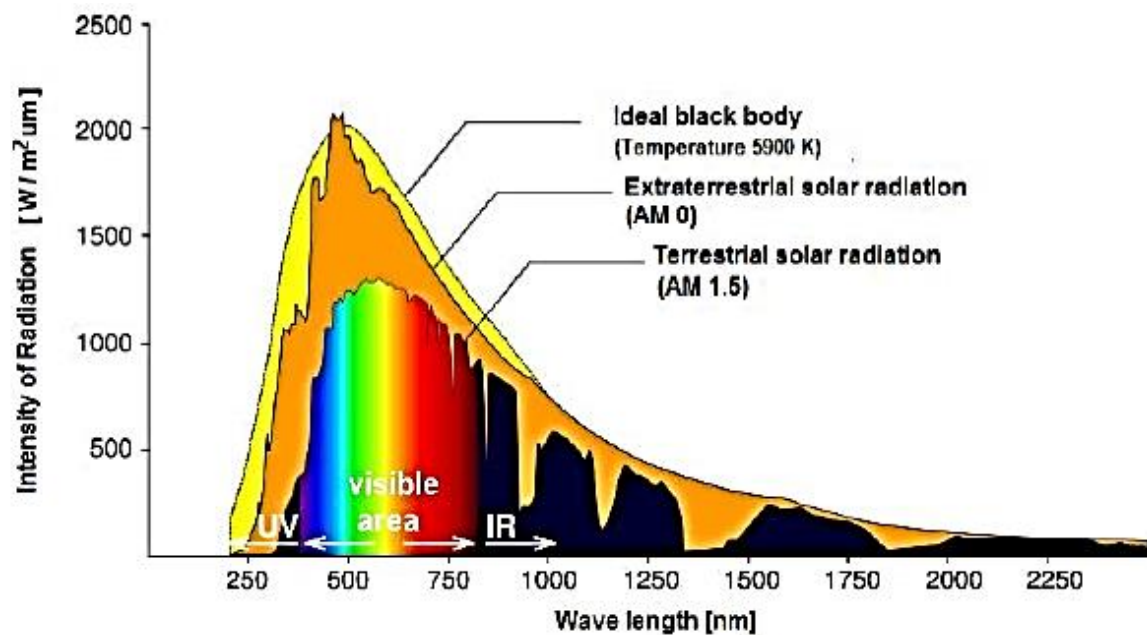


Figure I.5: Solar irradiance spectrums versus wavelength [16].

I.2.4.Characteristics of a PN junction solar cell

The solar cell characteristics are measured in standard test conditions (STC) to allow for location-independent and unbiased comparisons. STC for solar cells specifies a cell temperature of 25°C and total irradiance of 1000 W/m² with an air mass 1.5 (AM1.5G) spectrum. These correspond to the irradiance and spectrum of sunlight incident on a clear day upon a sun-facing 37°-tilted surface with the sun at an angle of 41.81° above the horizon [18].

Commonly made of silicon, solar cells, also known as photovoltaic cells, can convert sunlight to electricity with 15 to 30% energy efficiency [10]. A solar cell's structure is identical to a PN junction diode but with finger-shaped or transparent electrodes so that light can strike the semiconductor (Figure I.6).

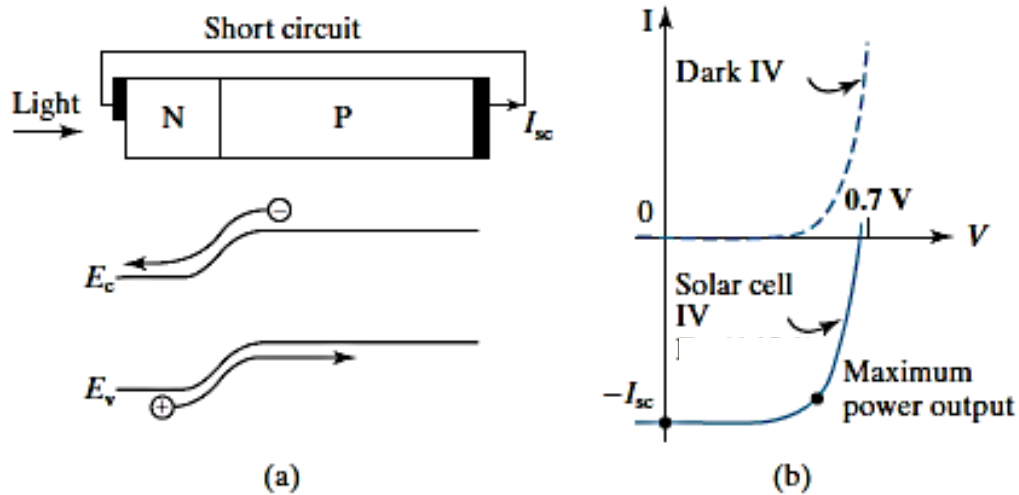


Figure I.6: (a) Light can produce a current in PN junction at $V = 0$. (b) Solar cell IV product is negative, indicating power generation [19].

Light is also a driving force that can produce a diode current without voltage, i.e., with the two diode terminals short-circuited so that $V = 0$. Figure I.6 shows that when light shines on the PN junction, the minority carriers that are generated by light within a diffusion length (more or less) from the junction can diffuse to the junction, be swept across the junction by the built-in field, and cause a current to flow out of the P terminal through the external short circuit and back into the N-terminal. This current is called the short-circuit current, I_{sc} . I_{sc} is proportional to the light intensity and to the cell area, of course [10].

The total diode (solar cell) current is the sum of the current generated by the voltage (I_D) and that generated by light (I_{sc}).

$$I = I_D - I_{sc} = I_S \left[\exp\left(\frac{qV}{nk_B T}\right) - 1 \right] - I_{sc} \quad (1.2)$$

The negative sign indicates that the direction of I_{sc} (Figure I.6(a)) is opposite to that of the voltage-generated current (I_D). The solar cell IV curve is shown in Figure I.6(b). Solar cell operates in the fourth quadrant of the IV plot. Since I and V have opposite signs, solar cell generates power. Each silicon solar cell produces about 0.6 V. Many cells are connected in series to obtain the desired voltage. Many such series strings are connected in parallel into a solar cell panel. There is a particular operating point on the IV curve (Figure I.6(b)) that maximizes the output power, $[I \times V]$. A load-matching circuit ensures that the cell operates at that point [10].

I.2.5. Equivalent electrical circuit of a solar cell

To understand the working principle of a solar cell, it is appropriate to make a model which is electrically equivalent. The ideal solar cell simplest model is given in Figure I.7 and consists of a constant current source and parallel connected diode. Constant current source works like a generator to push the electrons to the external circuit. Photo current I_L ($I_L \cong I_{sc}$) is generated due to the photovoltaic effect. Photo current depends on the intensity of the available sunlight, I_L of a current source is directly proportional to solar radiation. It means that with an increase of intensity of available sunlight, I_L must be increased. I_D is the diode dark current of a solar cell [20].

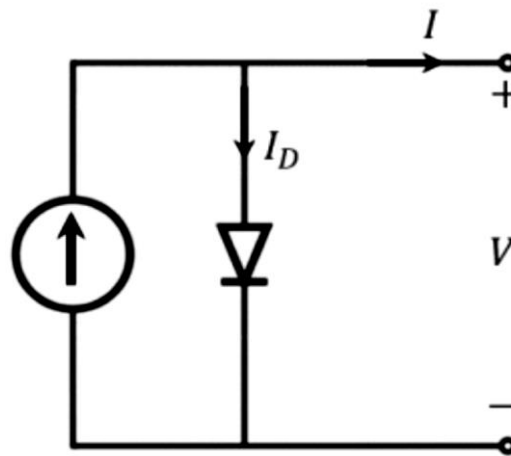


Figure I.7: Ideal solar cell.

Practically photovoltaic cells are not ideal. So, shunt and series resistance components are added to the equivalent circuit. The subsequent equivalent circuit is given in Figure I.8.

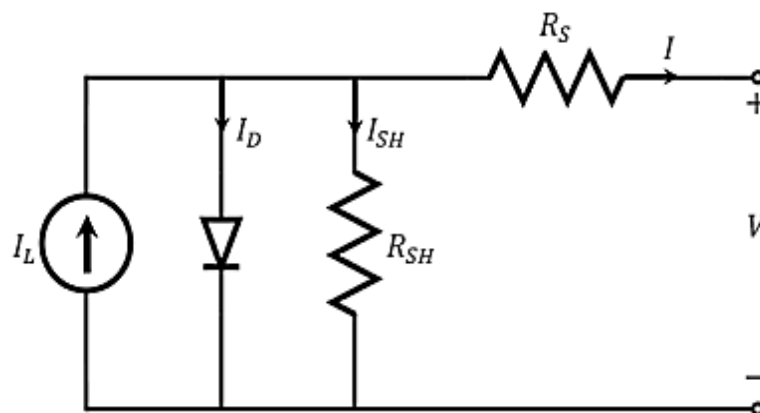


Figure I.8: Photovoltaic cell equivalent circuit.

From the schematic of a solar cell equivalent circuit, it is exemplified that the output current of a photovoltaic cell is the difference of photogenerated current, diode current, and shunt resistance current given in Eq.(I.3) [21].

$$I = I_L - I_D - I_{SH} \quad (I.3)$$

The voltage across these components governed the flow of currents..

$$V_D = V + IR_S \quad (I.4)$$

Where V_D is the voltage across shunt resistance (R_{SH}) and diode, V is the output terminal voltage and the voltage across the series resistance is IR_S :

I_D is the dark diode current from Shockley diode equation (Eq. I.1).

Current flows through shunt resistance can be calculated from ohms law

$$I_{SH} = \frac{V_D}{R_{SH}} \quad (I.5)$$

By substituting these values in Eq.(I.3), we get:

$$I = I_L - I_S \left[\exp\left(\frac{q(V+IR_S)}{nk_B T}\right) - 1 \right] - \left(\frac{V + IR_S}{R_{SH}} \right) \quad (I.6)$$

1.2.6. Figures of merit of a solar cell

Solar cells are easily characterized with characteristic current density - voltage ($J - V$) curves (Figure I.9). Furthermore, to reliably compare different devices there is some Figures of Merit that allow to assess the performance of solar cells. [22].

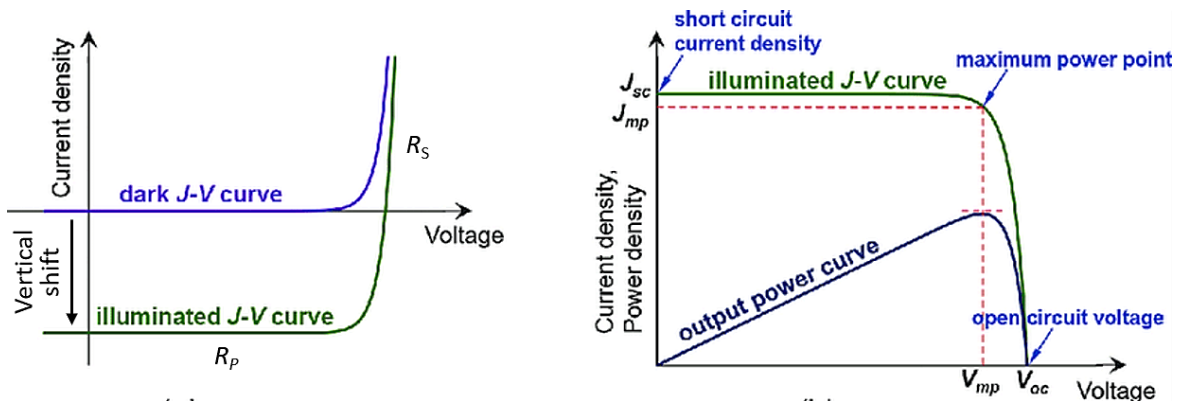


Figure I.9: $J - V$ curves characteristic of solar cells [23].

$J - V$ curves provide most of the following performance parameters: short-circuit current density J_{sc} , which is the current for 0V applied voltage; open-circuit voltage V_{oc} which represents the voltage for no current passing through the solar cell; fill factor FF , which indicates how close, in percentage, the solar cell is from its maximum potential power considering the V_{oc} and J_{sc} and light to power conversion efficiency η , which relates to the solar cell conversion efficiency. Additionally, it is possible to extract from $J - V$ curves the current and voltage of the solar cell working in its maximum power point, J_{mp} and V_{mp} respectively, as well as the R_s and R_{SH} resistances [22], [24].

I.2.6.1. Short circuit current (I_{sc})

The short-circuit current I_{sc} is the current of a solar cell under standard illumination conditions when the load has zero resistance (terminals are shorted together). In this case, the voltage at the terminals is zero. It means that for an ideal solar cell, the short circuit current is equal to the photogeneration current I_L :

$$I_{sc}(V = 0) = I_L \quad (I.7)$$

I.2.6.2. Open-circuit voltage (V_{oc})

The open circuit voltage V_{oc} is the maximum voltage that can generate the cell. It is the voltage between the terminals of a solar cell under standard illumination conditions when the load has infinite resistance that is open, in this situation, the current flowing through the cell is zero ($I = 0$). V_{oc} is given by the relation:

$$V_{oc} = \frac{nk_B T}{q} \ln \left(\frac{I_L}{I_S} + 1 \right) \quad (I.8)$$

I.2.6.3. The maximum power (P_{max})

The operating point is imposed by the load resistance and not by the cell it self. A judicious choice of the load resistance will thus make it possible to obtain the maximum power P_{max} , either

$$P_{max} = I_{mp} \times V_{mp} \quad (I.9)$$

I.2.6.4. Fill factor (FF)

The fill factor or FF gives us an overview of the cell quality. It is the ratio between the maximum power provided P_{max} and the ideal power ($V_{oc} \times I_{sc}$) (The surface of the largest

rectangle), where V_{mp} and I_{mp} are the voltage and current value corresponding to the operating point P_{max} for which the power is maximum. The following relation gives the FF :

$$FF = \frac{P_{max}}{V_{oc} \times I_{sc}} = \frac{I_{mp} \times V_{mp}}{V_{oc} \times I_{oc}} \quad (I.10)$$

I.2.6.5. Power conversion efficiency (η)

From the output parameters (V_{oc} , I_{sc} and FF), it is possible to determine the power conversion efficiency of the cell. Termed as η or PCE , it is the most important parameter since it allows the evaluation of the performance of the PV cell. It is defined as the percentage associated with the ratio between the maximum power provided by the cell (P_{max}) and the input power (P_{in}) from the sun illuminating the cell; P_{in} is often taken as 1000 W/m^2 . η is calculated according to the following formula [25]:

$$\eta = \frac{P_{max}}{P_{in}} \times 100\% = \frac{I_{mp} \times V_{mp}}{P_{in}} \times 100\% = \frac{FF \times I_{sc} \times V_{oc}}{P_{in}} \times 100\% \quad (I.11)$$

Power conversion efficiency (η) is important since it determines how effectively the space occupied by a solar cell is being used and how much area must be covered with solar cells to produce a given amount of power. Since larger areas require more resources to cover with solar cells, higher (η) is often desirable. We can improve it by increasing the short circuit current I_{sc} , the open circuit voltage V_{oc} and the fill factor FF .

I.2.6.6 .The quantum efficiency

The quantum efficiency of a solar cell is defined as the ratio of the number of electrons in the external circuit produced by the number of an incident photon of a given wavelength. Thus, one can define external and internal quantum efficiency denoted by $EQE(\lambda)$ and $IQE(\lambda)$ respectively. They differ in the treatment of photons reflected from the cell; all photons impinging on the cell surface are taken into account in the value of the $EQE(\lambda)$ but only photons that are not reflected are considered in the value of $IQE(\lambda)$ [21]. The following relation gives the external quantum efficiency [24]:

$$EQE(\lambda) = \frac{1}{q} \times \frac{hc}{\lambda} \times \frac{I_{sc}(\lambda)}{P_{in}(\lambda)} \quad (I.12)$$

Where q is the unit charge, λ is the photon wavelength, h is Planck's constant, c is the speed of light in air, I_{sc} is short circuit current and P_{in} is incident light power.

It is worth noting that the EQE spectrum measured under nobias voltage can be used to calculate I_{sc} ($I_{ph} = I_{sc}$). If the internal quantum efficiency ($IQE(\lambda)$) is known, the total photogenerated current is given by[26]:

$$I_{ph} = q \int_{(\lambda)} \Phi(\lambda) \{1 - R(\lambda)\} IQE(\lambda) d\lambda \tag{I.13}$$

Where $\Phi(\lambda)$ is the photon flux incident on the cell at wavelength λ ; $R(\lambda)$ is the reflection coefficient from the top surface, and the integration is carried out over all wavelength λ , of light absorbed by the solar cell. The values of the internal and external quantum efficiency are routinely measured to assess the performance of a solar cell by using interference filters or monochromators [26]. EQE graph for different materials used in solar cells is presented in Figure I.10.

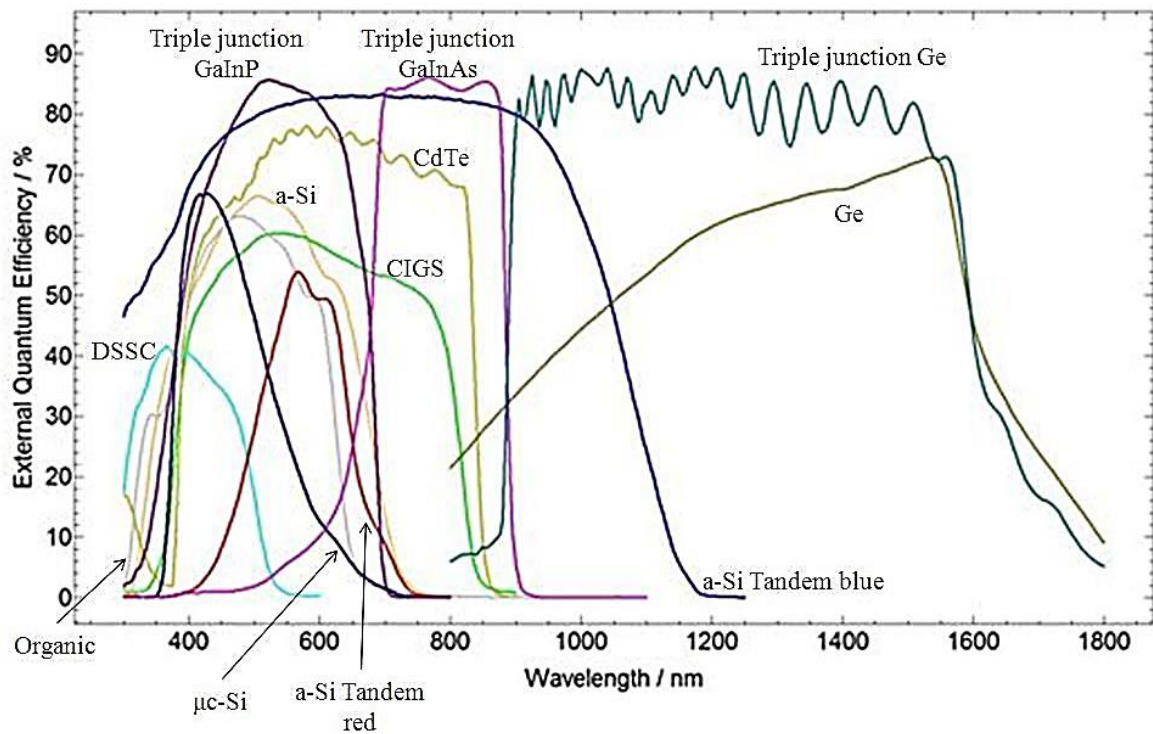


Figure I.10: EQE graph for different materials used in solar cells [27].

I.3.Schottky barrier solar cell

The choice of Schottky solar cells was informed by the simplicity of the design and fabrication process, coupled with a reduction in material cost compared to other forms of

silicon structures like pn and p-i-n structures [28]. When a metal and semiconductor are brought into electrical contact, a junction is formed. The junction can either behave as a Schottky contact or an Ohmic contact depending on the characteristics of the interface which is majorly influenced by the work function and electron affinity of the metal and semiconductor respectively [29-30]. Additionally, surface states can also affect the nature of the junction formed. Currently, Schottky solar cell present an attractive advantage over pn junction solar cell, such as lower forward turn-on voltage, coupled with the noncomplexity of the fabrication of these devices. FigureI.11 depicts the schematic diagram of a typical Schottky junction solar cell [28].

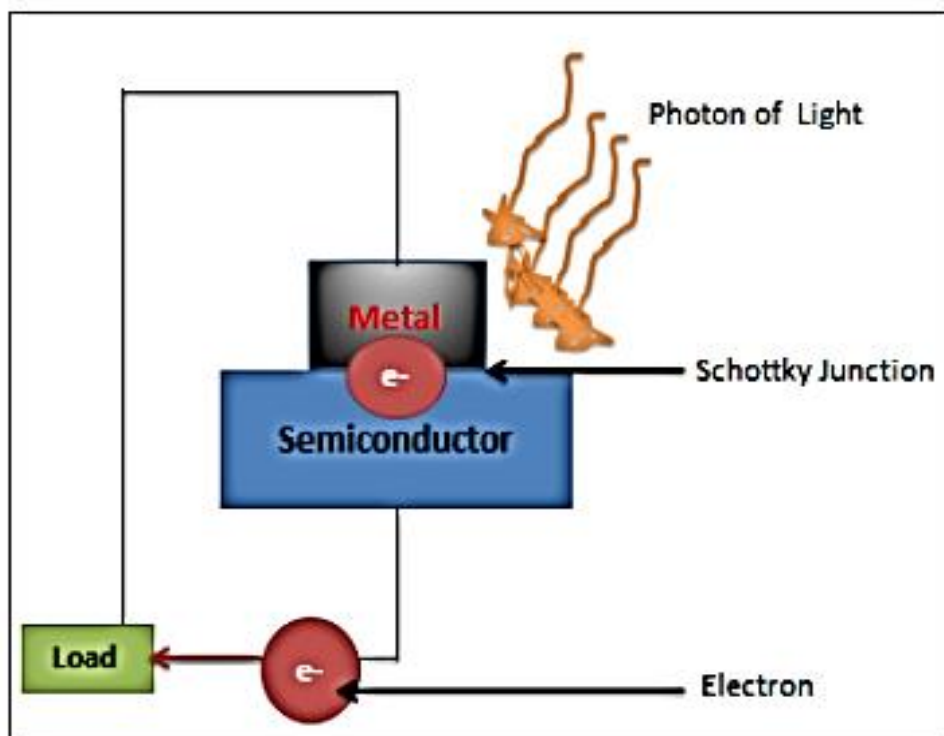


Figure I.11: Schematic diagram of a Schottky junction solar cell showing the flow of electrons to the external load represented by the green rectangle adapted from [30]. Photon of light shone at the metal and semiconductor junction to facilitate electron flow.

The operational principle of Schottky solar cells is such that, when photon absorption occurs in the Schottky solar cell, with energies greater than the band gap of the semiconductor, electron-hole pairs (EHP) are created in the device and charge separation occurs at the Schottky interface. There is a sweeping effect of the minority carriers (holes h) into the metal region, resulting in the charging of the semiconductor by the majority carriers left behind. The quasi-Fermi level of the majority carriers in the semiconductor

tends to shift as depicted in Figure I.12, and it will be observed that, the quasi-Fermi level of the electrons for instance an n-type semiconductor is some distance away from the junction and increases with illumination intensity. This quasi Fermi level becomes higher than the Fermi level of the metal. A photo-voltage is thereby produced in the external load connected to the solar cell, due, largely to the splitting of the Fermi energy level [30]. The tendency of the semiconductor layer to sustain the difference in the quasi-Fermi level in the Schottky junction is crucial to maintaining the photovoltaic to electrical energy conversion.

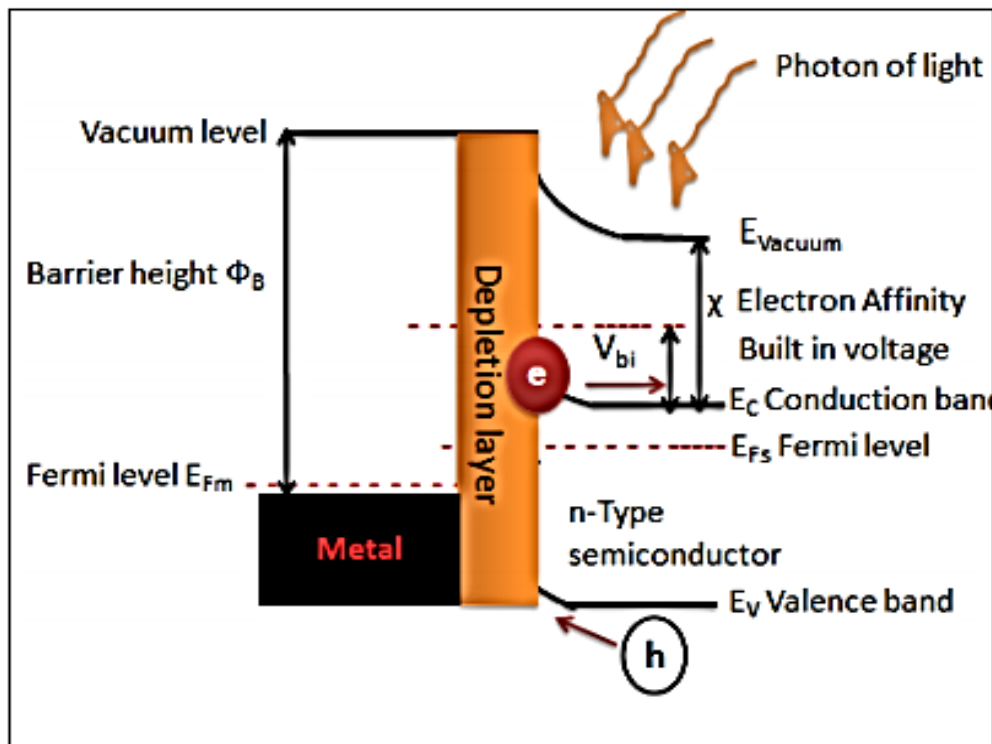


Figure I.12 Simplified band diagram of a metal and n-type semiconductor Schottky solar cell depicting the thermionic emission across the Schottky junction under illumination condition adapted and drawn from [30].

A Schottky junction is formed when the metal and semiconductor are brought into electrical contact with each other. Charge carrier (electrons or holes) will diffuse from the higher concentration region to a lower concentration region. This mechanism occurs due to the two way exchange of charge carriers between the metal and semiconductor. Thus at zero bias condition, some electrons will flow from the metal to the semiconductor and vice versa. However, since the height of the barrier is higher on the metal layer, more electrons will transfer from the semiconductor to the metal than in the opposite direction.

Under the condition of thermal equilibrium, the Fermi energy level of the Schottky junction is constant in each layer of the material, since no external electric DC bias voltage is applied across the solar cell [31]. This is shown in the diagram in Figure I.13.

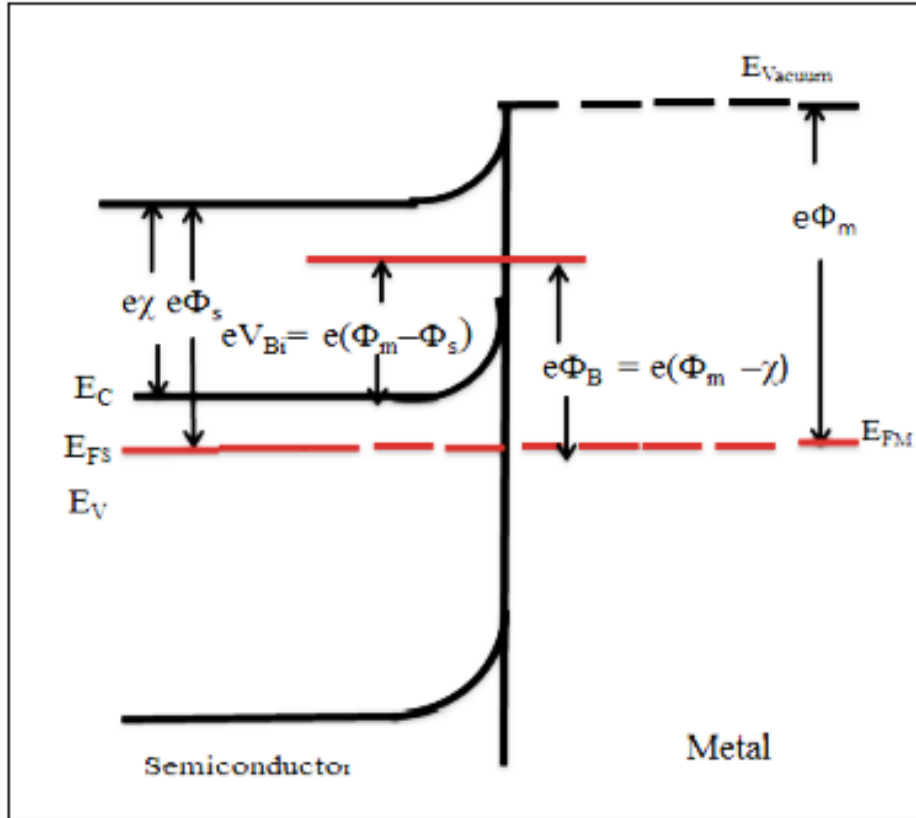


Figure I.13: The energy band diagram of metal/n-type semiconductor junction which reveals the band bending process after the metal semiconductor junction comes into contact adapted from [32].

If the work function of the semiconductor (Φ_s) is lower than that of the metal (Φ_m), presented by ($\Phi_s < \Phi_m$), electrons will flow from the semiconductor to the metallic layer, the reby leaving a region of uncompensated donor or positive charges ND^+ , resulting in the formation of a depletion region with a built in voltage (eV_{Bi}) in the semiconductor layer [32, 33].

The built-in-voltage formed, prevents the further migration of electrons from the semiconductor to the metal. The barrier created at the metal/semiconductor interface is the barrier height; which is the difference between the Fermi energy level of the metal (E_{FM}) and the band edge (E_C) where the majority carriers are located in the Schottky diode [33].

If χ_{sc} is the electron affinity of the semiconductor, consequently, the barrier height for n-type of Schottky junction can be computed using Eq.(I.14) :

$$q\phi_B = q(\phi_m - \chi_{sc}) \quad (I.14)$$

Or simply:

$$\phi_B = (\phi_m - \chi_{sc}) \quad (I.15)$$

If ϕ_B is expressed in eV.

The contact potential between the metal and semiconductors at thermal equilibrium creates a balance in charge carrier transport, so that the net current flow is zero. Under forward and reverse voltage bias conditions. The current flow depends on the type of bias and the amount of applied external potential [33]. Now, using an illustration of a metal-and n-type semiconductor diode in forward bias, the semiconductor layer is connected to the negative region, and a positive voltage is applied to the metal layer. The external potential applied opposes the built-in voltage with in the depletion layer. Hence, the Fermi levels are the refore no longer at equilibrium but shifted with respect to one another based on the magnitude of the applied voltage as shown on the left side in Figure I.14 [28]. With the application of a positive DC bias voltage seen on the left of Figure I.14, the Fermi energy level (E_{FM}) of the metal layer is lowered with respect to the Fermi level of the semiconductor layer (E_{FS}). As such, there is a reduction in the built-in-potential (V_{Bi}), and the depletion layer so that electrons from the semiconductor layer can migrate to metal layer having to surmount a lower barrier before reaching the metal. Consequently, if the applied voltage (V) is equivalent or greater than to the (V_{Bi}), then, a positive current termed the forward current begins to flow at the Schottky junction.

$$J_D = J_S \left\{ \exp \left[\frac{qV}{nk_B T} \right] - 1 \right\} \quad (I.16)$$

Where J_D is the current density in (A/cm^2) , J_S is the reverse saturation current density in (A/cm^2),(n) is the ideality factor of the diode and k_B is Boltzmann's constant.

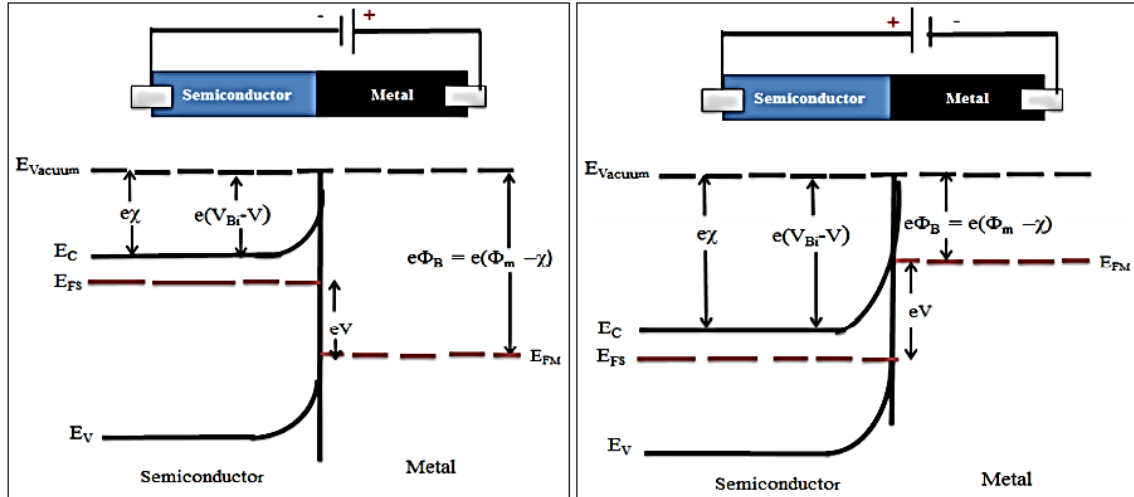


Figure I.14: Metal and n-type Schottky junction solar cells in positive DC voltage bias and negative DC voltage bias conditions on the left and the right respectively Adapted from [32].

On the application of a negative DC bias as shown on the right of Figure I.14, the Fermi level of the metal layer (E_{FM}) increases with respect to the Fermi level of the semiconductor layer (E_{FS}) making the depletion layer to widen and the built in electric field larger at the Schottky junction interface. The barrier height remains constant so small leakage current can flow in the junction which is totally not a function of the applied DC negative bias voltage [32]. Usually, the dominant transport mechanism in Schottky junctions is the thermionic emission mechanism. In this case, the reverse saturation current density is given by :

$$J_S = A^*T^2 \exp\left(\frac{-\phi_B}{k_B T}\right) \quad (I.17)$$

Where (A^*) is effective Richardson’s constant in $A\ cm^{-2}\ ^\circ K^{-2}$, T is the absolute temperature in $^\circ K$ and (ϕ_B) is the Schottky barrier height in eV .

Other mechanisms that are responsible for charge carrier transport in Schottky barrier solar cell are field-effect thermionic emission or tunnelling of charge carriers through the Schottky barrier and drift-diffusion of charge carriers from the semiconductor to the metal [32-33].

Under illumination, the photo-generated current density (J_{ph}) flows in the opposite direction to the forward current under dark conditions (diode). Therefore, the current through the solar cell under illumination is given by [34, 35]:

$$J_{ph} = J_{sc} - J_D = J_{sc} - J_S \left\{ \exp \left[\frac{qV}{nk_B T} \right] - 1 \right\} \quad (I.18)$$

Where J_{sc} denotes the short circuit current density of the solar cell under illumination.

If the reverse saturation current J_S is limited by thermionic emission, then :

$$J_{ph} = J_{sc} - J_D = J_{sc} - A^* T^2 \exp \left(\frac{-\phi_B}{k_B T} \right) \left\{ \exp \left[\frac{qV}{nk_B T} \right] - 1 \right\} \quad (I.19)$$

And the open circuit voltage V_{OC} can be deduced simply by setting $J_{ph} = 0$, which is:

$$V_{oc} \cong n \left[\left(\frac{k_B T}{q} \right) \ln \left(\frac{J_{sc}}{A^* T^2} \right) + \frac{\phi_B}{q} \right] \quad (I.20)$$

I.4. Generations of solar cells

Traditionally solar cells are separated into four generations [14].

I.4.1. First Generation solar cells

First generation (1G) of solar cells is mainly based on silicon wafers and typically the power conversion is about 15-20%. Generally, in comparison of non-silicon based solar cells, this solar cell technology is more efficient and of longer life but at the higher temperature, they are more peril to lose some part of their efficiency. Currently, four types of silicon-based photovoltaic cells are commercially used for the manufacturing of solar panels. These types are monocrystalline, polycrystalline, amorphous and hybrid solar cells [36,37].

I.4.2. Second Generation solar cells

Second generation (2G) of solar cells are based on amorphous silicon and non-silicon materials namely copper indium gallium selenide (CIGS) and cadmium telluride (CdTe), where typically the power conversion efficiency is about 10-15%. Use of silicon wafers are avoided in second generation solar cell and consumption of lower material reduces the production cost of 2G solar cells in comparison of the first-generation solar cell. This cell generation class is also known as thin film solar cells because of using only few micrometer thicknesses of different layer materials in comparison of crystalline silicon based cells. This type of technology is commercially using because of lower manufacturing cost and using less material. The second-generation solar cells production is still limited due to the use of rare elements and high-temperature treatments. So, the production cost is less than the first generation solar cell but still higher than other technologies [36,37].

I.4.3.Third Generation solar cells

In this new technology solar cells are made from the variety of new materials rather than using silicon such as solar inks using in printing technology, silicon wires, nanotubes, conductive plastics, and organic materials. The goal is to improve the commercially available solar cell by enhancing the efficiency and to reduce the cost to make them economical. So, more peoples will use this solar cell technology. Polymer solar cells are a subcategory of organic solar cells. Third generation solar cells are expensive high performance multi junction experimental solar cells. Mostly the work is done in laboratories and not commercially available. Currently new class of thin film solar cell sunder investigations are perovskite solar cells and quaternary compounds material based solar cells such as kesterite solar cells. These types of devices show an enormous potential with record power conversion efficiency of about 20% on a very small area. Polymer solar cells are fabricated by roll to roll (*R2R*) technology and can be compared to the newspaper printing. In the comparison of first and second-generation solar cells, third generation solar cells are limited but they have great potential. Recently research interest is significantly increases in polymer solar cells [38].

I.4.4.Fourth-generation Solar Cells

These are solar cells which are also called organic-inorganics because, they combine the flexibility of polymer thin films with the stability of inorganic nanostructured layers with a view targeted at maintaining the low cost of thin film photovoltaic [28], improving charge transport (carrier lifetime) ,enhancement in energy harvesting cross section of the solar cell and improved optical coupling by increasing the optical path length especially when metal nanoparticles (mNP) are incorporated within the layers of a perovskite solar cell (PSC) [36].An example of a fourth generation solar cell is a perovskite solar cell (PSC) that has incorporated within its layers carbon nanotubes (CNT), metal nanoparticles (mNP), nano hybrid materials or grapheme [39]. Further more, it has been established that, the incorporation of inorganic materials within active materials like PSC, has greatly improved the carrier life time of solar cell devices.

I.5.Different types of solar cells

Solar cells are divided into two major groups. They are silicon semiconductor type and non-silicon type. The details are as follows [14].

I.5.1.Silicon semiconductor type solar cells

There are three major types of silicon semiconductor photovoltaic cells, which are used to create panels (Figure I.15) [14].

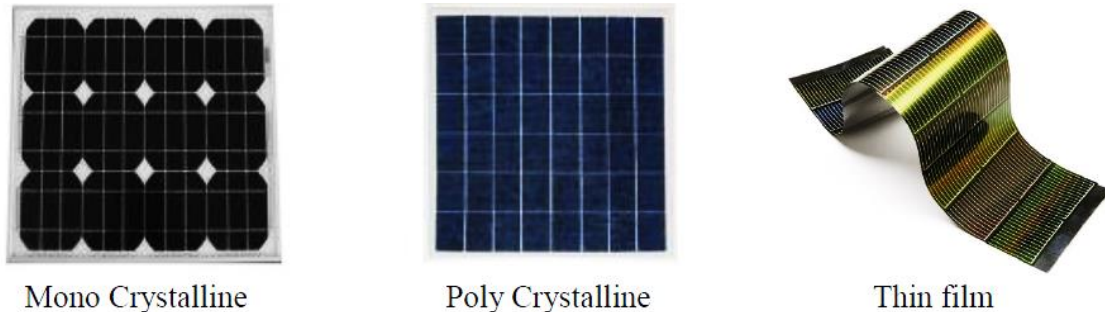


Figure I.15: Types of photovoltaic solar cells [14].

I.5.1.1.Monocrystalline solar cell

These types of solar cells belong from first-generation solar cell technologies. The width of the wafer used in these types of solar cells is up to $200\mu m$. The cell slice is cut from a pure silicon bar, which allows them to more efficiently converting the sunlight radiation energy into electrical energy. Silicon used in monocrystalline is single-crystal silicon. The complete cell is aligned in the same direction, so when the light falls on the cells at the accurate direction, they are very efficient. In a sunny day, photovoltaic cells work best with the sunlight directly falls on accurate direction. They are absorbing most of the solar radiation, so they have a uniform blacker color. Cost of the production of these types of solar cells is more than in the comparison of a polycrystalline cell. In a comparison of polycrystalline, monocrystalline is the most efficient type of photovoltaic solar cells.

I.5.1.2.Polycrystalline solar cell

These types of solar cells also belong from first-generation solar cell technologies. These cells are made up of several silicon cells joined together instead of using a single crystal of silicon. In general, the cost of production of a polycrystalline solar cell is not much higher than monocrystalline. Therefore, they are also more affordable. In comparison with a monocrystalline solar cell, the power conversion efficiency of polycrystalline solar cell is less. Their overall manufacturing design can often make up for the efficiency loss.

I.5.1.3. Amorphous solar cell

Amorphous silicon ($a - Si$) solar cells belong from a thin-film solar cell. In these types of solar cells, one or more layers of photovoltaic materials are deposit on a substrate. In comparison with other technologies, they have low manufacturing cost. To make thin-film photovoltaic solar cells, manufacturers spray a layer of silicon on a substrate. They are produced by placing one or more thin layers of photovoltaic composite on a substrate. Thin film photovoltaic solar cells are different from other types; they are also more flexible than other types. It can be put onto different surfaces i.e. curved and straight.

I.5.2. Other types of solar cell

Above discussed, silicon-based solar cells are most commonly used solar cells. There are some other types such as (*CIGS*) and cadmium telluride (*CdTe*) based solar cells, kesterite and perovskite solar cells, which are also used due to their good conversion capabilities, earth-abundant materials, and enhanced power conversion efficiencies. These types of photovoltaic solar cells are deliberated in detailed in the next section.

I.6. Thin film solar cells

Thin film photovoltaic solar cells belong from second and third generation solar cell technology. These types of solar cells are manufactured by depositing one or more layers of photovoltaic materials on a metal, plastic or glass substrate. Commercially thin film photovoltaic solar cells are used in various technologies, such as copper indium gallium selenide (*CIGS*), cadmium telluride (*CdTe*), kesterite and perovskite solar cell technologies. The film thickness of these types of solar cells varies from few nm to tens of μm , due to this; these types of solar cells are flexible and lower in weight. Thin film technology is cheaper than other technologies because of devices have relatively less material. Thin film photovoltaic technologies are based on various types of light absorbers semiconductor materials. The absorption coefficient of these types of materials is higher than crystalline materials. Therefore, a very thin layer of the absorber layer is sufficient for the effective absorption of sunlight. Historically in the thin film technology, amorphous silicon-based solar cells played a momentous role. Now a day's researchers move towards cadmium telluride (*CdTe*) and copper indium gallium selenide (*CIGS*) based thin film devices because of their high efficiency and good performance and reached in the commercial stage. In research and development scale these technologies have power conversion efficiency up to 18% [40] while commercially they have a conversion efficiency of 14-16 % [41,42]. For the fabrication and development of low cost and

sustainable thin film photovoltaic cells kesterite based absorber materials are intensively studies such as copper zinc tin sulfide Cu_2ZnSnS_4 (CZTS), Copper zinc tin selenide $Cu_2ZnSnSe_4$ (CZTSe) and sulfur-selenium alloy $Cu_2ZnSn(S_xSe_{1-x})_4$ (CZTSSe) [43,44]. These materials drawing attention because of their good optical properties for photovoltaic applications [45]. These absorber materials are copper based nontoxic semiconductor materials [46]. They are the good replacement for the chalcopyrite absorbers by replacing indium (*In*) with comparatively inexpensive zinc (*Zn*) and gallium (*Ga*) with tin (*Sn*) in the *CIGS* absorbers [47,48]. The outstanding features and efficient performance of these kesterite based materials made them very fascinating in the thin film's community [49,50]. Table I.1 lists the current state of the art single junction solar cells for both *p-n* and excitonic junctions under the AM1.5G spectrum [51].

Table I.1. Current state of the art single junction solar cells [51].

Category	Cell	V_{oc} (V)	J_{sc} (mAcm ⁻²)	FF	PCE
<i>p-n</i>					
Silicon	Crystalline	0.696	42.0	0.836	24.4%
Silicon	Multicrystalline	0.664	37.7	0.809	20.3%
Silicon	Amorphous	0.886	16.7	0.670	10.1%
III-V	GaAs thin film	1.111	29.4	0.859	28.1%
III-V	GaAs multicrystalline	0.994	23.2	0.797	18.4%
III-V	InP crystalline	0.878	29.5	0.854	22.1%
Thin Film	CIGS	0.690	35.5	0.812	19.9%
Thin Film	CdTe	0.845	26.1	0.755	16.7%
Thin Film	CZTSS	0.516	28.6	0.654	9.7%
Excitonic					
	Dye-sensitized	0.736	21.7	0.736	10.9%
	Organic polymer	0.816	14.4	0.702	8.3%



Chapter II :

CIGS-based Solar Cells

II.1.Introduction

The usage of photovoltaic solar energy is increasing in recent years. The second generation of thin-film solar cells based on $\text{Cu}(\text{In,Ga})(\text{Se, S})_2$, or CIGS for short, has achieved a record efficiency of 23.3% [52,53], and is one of the main competitors to silicon cells with respect to efficiency and cost. In addition, CIGS is also advantageous for application in multi junction solar cells, since the gap of the different layers can be tuned by varying the ratio of In and Ga, and/or S and Se. Point defects and impurities, which may act as dopants, traps, or recombination centers, play a critical role in the photovoltaic properties of the material [54–55]. CIGS alloys are intrinsically p-type [56]. CuInSe_2 can easily be doped n-type or p-type depending on the dominant defects. Usually, n-type CuInSe_2 is grown under Cu-rich and Se-deficient environment whereas p-type CuInSe_2 is grown under Cu-poor and Se-rich environment [57, 58]. Thus Se vacancy (V_{Se}) and Cu vacancy (V_{Cu}) are believed to be the dominant defects in n- and p-type CuInSe_2 respectively [58]. Effective n-type doping of CuGaSe_2 can be achieved by hydrogen incorporation [56]. This latter does not only passivate intrinsic defects by forming a defect complex with the most abundant native defects $V_{\text{Cu}}, \text{Cu}_{\text{Ga}}$, and Ga_{Cu} , but can produce shallow donors mainly by the formation of shallow donor $V_{\text{Cu}}+2\text{H}$ defects; which turn CuGaSe_2 n-type [56].

In this chapter, we give a short overview on the present knowledge of CIGS-based thin film solar cells. We focus on three points: (i) Description of the basic material properties such as crystal and optical properties. (ii) Description of the classic (standard) CIGS solar cell structure. (iii) Description of the Schottky barrier solar cell based on n-type CIGS material.

II.2. CIGS material properties

II.2.1. Structural and Compositional Properties

CuInSe_2 and CuGaSe_2 , the materials that form the alloy $\text{Cu}(\text{In,Ga})\text{Se}_2$ or CIGS, belong to the semiconducting I-III-VI₂ materials family that crystallize in the tetragonal chalcopyrite structure [59]. The CIGS forms a quaternary compound when Gallium (Ga)

atoms partially substitute Indium (In) atoms in CuInSe_2 ternary system. The CIGS has a chalcopyrite tetragonal structure, which is similar to that of the CuInSe_2 structure as shown in Figure II.1.

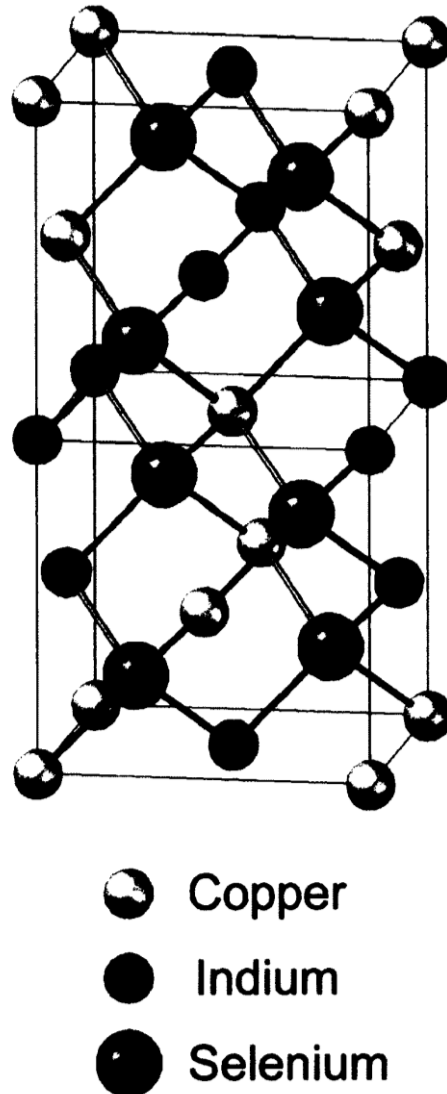


Figure II.1: Chalcopyrite crystal structures of CIGS [after 60].

The tetragonal structure of the chalcopyrite compound can be considered as a super lattice Zinc Blende structure by elongating the unit cube along the z-axis twice the length that becomes the c-axis of the chalcopyrite structure [57,61]. The ratio of the tetragonal lattice parameters c/a , which is called tetragonal deformation, is close to 2 and varies due to the difference in bond strength in Cu-Se, In-Se or Ga-Se. So, the c/a ratio is a function of gallium molar fraction; x where $x = \text{Ga}/(\text{In} + \text{Ga})$, such as $(c/a) > 2$ for $x = 0$ and $(c/a) < 2$ for $x = 1$ [57]. CIGS is formed by alloying CuInSe_2 in any proportion

with CuGaSe_2 . In high performance CIGS cell, the $Ga/(In + Ga)$ and the $Cu/(In + Ga)$ ratios are typically 0.2-0.3 and 0.7-1, respectively [57]. There is the possibility of high defect density in the Cu-poor film but these defect densities should be reasonably low and electronically inactive to avoid adverse effects on solar cells performance [57, 62].

II.2.2. Optical Properties and Band Gap Grading

The system of copper chalcopyrites $\text{Cu(In,Ga,Al)(Se,S)}_2$ includes a wide range of band-gap energies (E_g) from 1.04 eV in CuInSe_2 up to 2.4 eV in CuGaS_2 , and even 2.7 eV in CuAlS_2 , thus, covering most of the visible spectrum. All these compounds have a direct band gap making them suitable for thin film photovoltaic absorber materials. Figure II.2 summarises lattice constants (a) and band-gap energies (E_g) of this system [59].

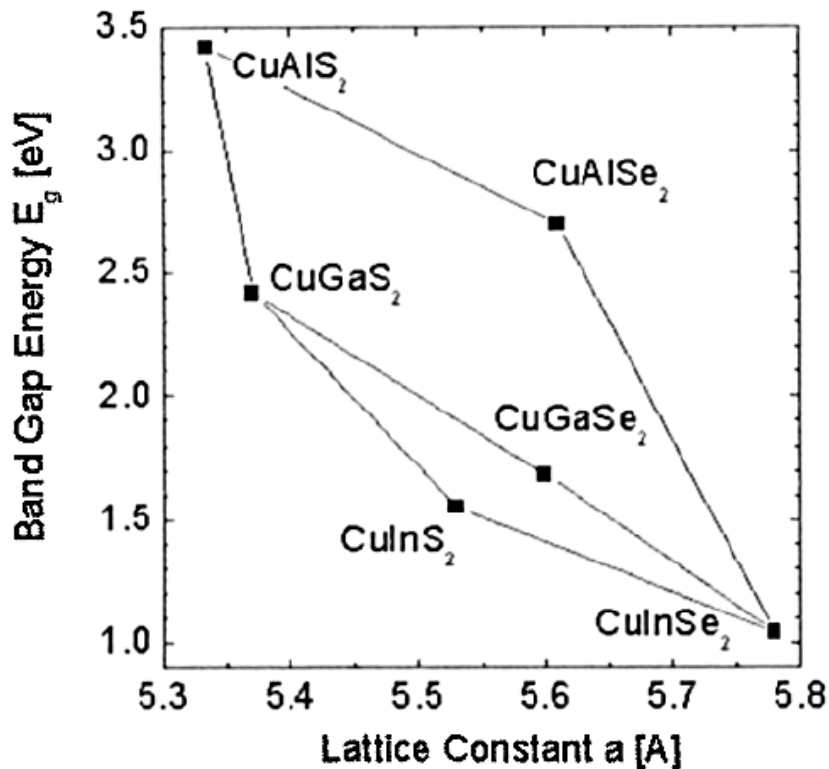


Figure II.2: Band-gap energies (E_g) vs. the lattice constant (a) of the Cu (In, Ga,Al)(S, Se)₂ alloy system [59].

CIGS films have very high absorption coefficient, with values larger than 10^5cm^{-1} for 1.5 eV and higher energy photons [57,63]. So, only a few micrometer thick CIGS film is

needed to absorb most of the incident light. The absorption coefficient, can be calculated from the transmission and reflection coefficients using the following expression [64]:

$$\alpha = \frac{2\ln(1-R) - \ln(T)}{d} \quad (\text{II.1})$$

Where d is the thickness of the thin film, R is the reflection and T is the transmission. Since CIGS is a direct gap semiconductor, the absorption coefficient in the region of strong absorption obeys the following equation [57]:

$$\alpha = \frac{A}{hv} (hv - E_g)^{1/2} \quad (\text{II.2})$$

Where h is the Planck constant, v is the radiation frequency, E_g is the band gap energy and A is a constant, which depends on the nature of the radiation. The extrapolation of the linear portion of the $(\alpha hv)^2$ versus hv graph at $hv = 0$ gives therefore the band gap value of the material. Cu(In,Ga)Se₂ has a tunable band gap that varies with $x = Ga/(In + Ga)$. The relation between the E_g and x can be expressed by the following empirical formula [65]:

$$E_g(x) = (1 - x)E_g(CIS) + xE_g(CGS) - bx(1 - x) \quad (\text{II.3})$$

Where $E_g(CIS)$ is 1.04 eV, the band gap of CuInSe₂; $E_g(CGS)$ is 1.68 eV, the band gap of CuGaSe₂; and b is the bowing parameter that depends on the growth. The mostre producible values of b are around 0.15-0.24 eV [65]. The Ga content in the Cu(In,Ga)Se₂ thin film affects the band-gap primarily in the conduction band. The band gap of Cu(In,Ga)Se₂ increases with increasing Ga content by shifting the conduction band position [65]. So, with an appropriate spatial variation of Ga in the Cu(In,Ga)Se₂, various and gap profiles can be achieved as shown in Figure II.3[57]. Introducing a higher $Ga/(In + Ga)$ ratio near the front surface (Space charge region) and at the back surface region of Cu(In,Ga)Se₂ film will increase the band gap locally. The increase in the band gap, ΔE_g , creates an additional electric field, which is also called quasi electrical field [66]. The Ga gradient in the space charge region (SRC) and at the back surface improves J_{sc} performance due to the additional force created that increases the carrier collection [57].

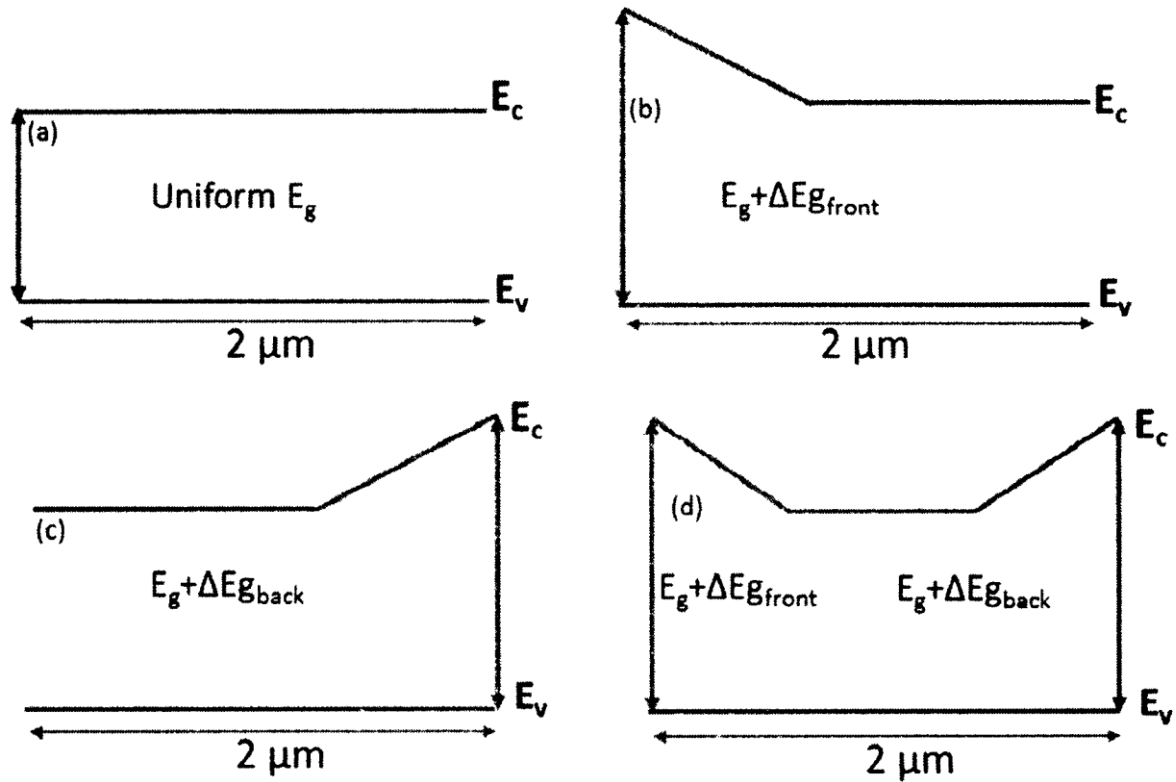


Figure II.3: Different types of absorber band gap profiles: (a) Uniform band gap, (b) Front grading (Space charge region grading), (c) back surface grading, (d) Double grading [57].

The back surface recombination can be reduced significantly due to the back surface grading, which also enhances the voltage by reducing recombination. The SCR grading as an addition to the back surface grading also increases the device voltage since the voltage is also determined by the band gap in the space charge region. In general, a proper band-gap grading in the SCR and back surface are capable of significantly improving the device performance [57].

II.3. The conventional (standard) CIGS solar cell structure

Typically, the conventional (standard) CIGS solar cells are composed by the layers present in Figure II.4 [67]. From bottom to top, it consists of a glass substrate, Mo back contact, CIGS absorber, CdS buffer layer and the window layer. The soda-lime glass (SLG) is as the common substrate to be used in the industry and at the laboratory scale. During the CIGS growth, Na diffuses into the CIGS absorber improving its structural and electrical properties [67, 68,69]. Additional advantages of SLG is its low cost, accessibility and the expansion coefficient being near the CIGS coefficient value [70].

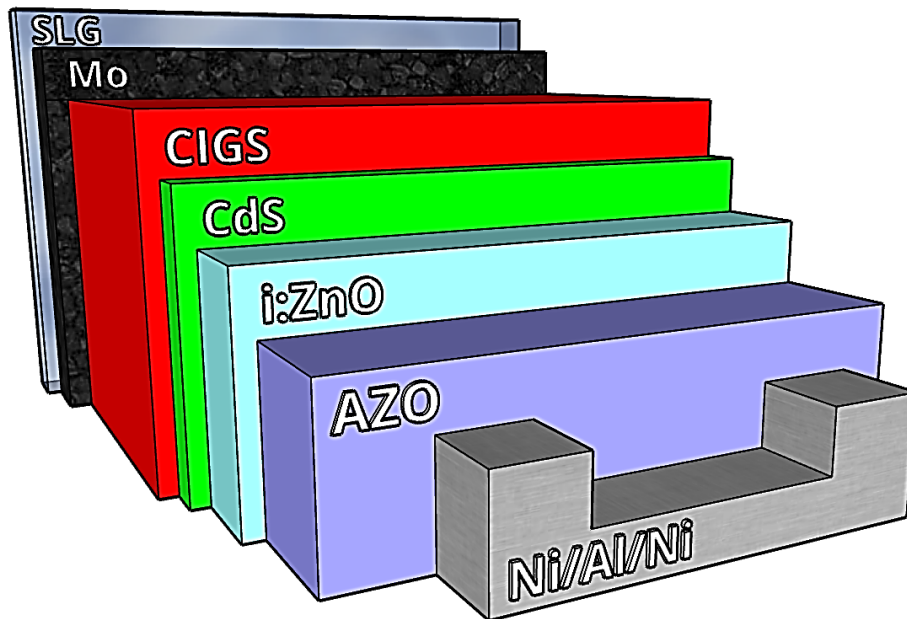


Figure II.4: Standard layer structure of CIGS solar cells, layers not at scale [67]

CIGS solar cells are typically made in substrate configuration, also known as bottom up approach. This means that the cell fabrication starts from the substrate layer (the bottom-most layer in Figure II.4), continues with the formation of the subsequent layers and ends with the light-facing transparent conductive oxide (TCO) layer [71].

The most commonly used back contact for CIGS solar cells is molybdenum (Mo), normally formed by direct current (DC) sputtering [72]. Mo is popular, because it is stable and inert during high-temperature growth of the CIGS layer, it is economical and provides an ohmic contact with CIGS due to a MoSe_2 layer formation [65], [73].

The conventional buffer material for CIGS solar cells is CdS with a few tens of nanometer thickness. CdS is a semiconductor with a band gap of 2.4 eV which promotes a suitable band alignment at the CIGS/CdS interface and lattice match with CIGS [74, 75]. The buffer layer forms the p-n junction with the absorber and is placed between the window layer and the absorber (Figure II.4). The role of the *n*-type buffer layer in CIGS solar cells is manifold: better lattice match between the absorber and the window layer (transparent front contact), protection of the CIGS surface during the sputtering of the window layer and the formation of a low-recombination hetero junction [76], [77].

The window layer is composed by a zinc oxide bi-layer. Near the CdS is deposited an intrinsic ZnO (i:ZnO) to prevent possible shunts, that degrade the cell performance by

providing alternative paths to charge current, due to its high resistivity. Towards the front contact this zinc oxide layer is typically doped with aluminium, ZnO:Al (AZO), due to its high conductivity coupled with high transparency allowing for an effective charge collection [75]. Finally, it is normally deposited a Ni/Al/Ni grid layer as a front contact and connection to the external circuit. The presence of Ni is justified by the encapsulation of Al to prevent it to react with both the AZO window layer and the atmosphere [78].

II.4. Schottky barrier solar cell based on CIGS material

In this last section we give a brief description of the Schottky barrier solar cell based on CIGS material which will be the aim of our study. Figure II.5 (a) displays a schematic diagram of a CIGS-based Schottky solar cell and the corresponding band diagram is shown in Figure II.5 (b) under sunlight illumination. The base layer is n-type CIGS with band gap energy $E_g \cong 1.15 \text{ eV}$. This latter corresponds to a $Ga/(In + Ga)$ ratio $x \cong 0.25$ which is recommended for high performance CIGS solar cells [57]. The Schottky barrier at the metal/semiconductor interface is obtained by making the anode metal (which is situated on the top of the cell) from platinum (Pt). With such a choice; the anode work function (ϕ_m) is higher than the electron affinity (χ_{sc}) of the CIGS material ($\phi_m = 6.35 \text{ eV} > \chi_{sc} = 4.8 \text{ eV}$). However, the cathode (Al) is defined to be neutral (Ohmic contact). The bands of CIGS at the (Pt/ CIGS) interface bend upward at zero bias (Figure II.5 (b)). Once optical absorption occurs in the Schottky solar cell, electron-hole pairs (EHP) are photogenerated in the device and charge separation occurs, at the Schottky interface, by the built-in field of the depletion region, resulting in a photovoltage between the metallic anode and the bulk of the CIGS material. The sweeping effect drifts the minority carriers (holes h) into the metal region; and the majority carriers (electrons e) into the neutral n-type region; where they have to reach the collection electrode (cathode) by diffusion. Incident photon illumination creates electron-hole pairs in the depletion region, as well as in the neutral region of the n-type CIGS material. For the latter, however, only those holes within the diffusion length from the edge of the depletion region have a chance to diffuse to the depletion region, and only those electrons within the diffusion length from the edge of the collection electrode have a chance to diffuse to the cathode electrode. The carriers sweeping effect in the depletion region, and the carrier diffusion in the neutral region, produce the photo-generated current which flows in the opposite direction to the forward current under dark conditions

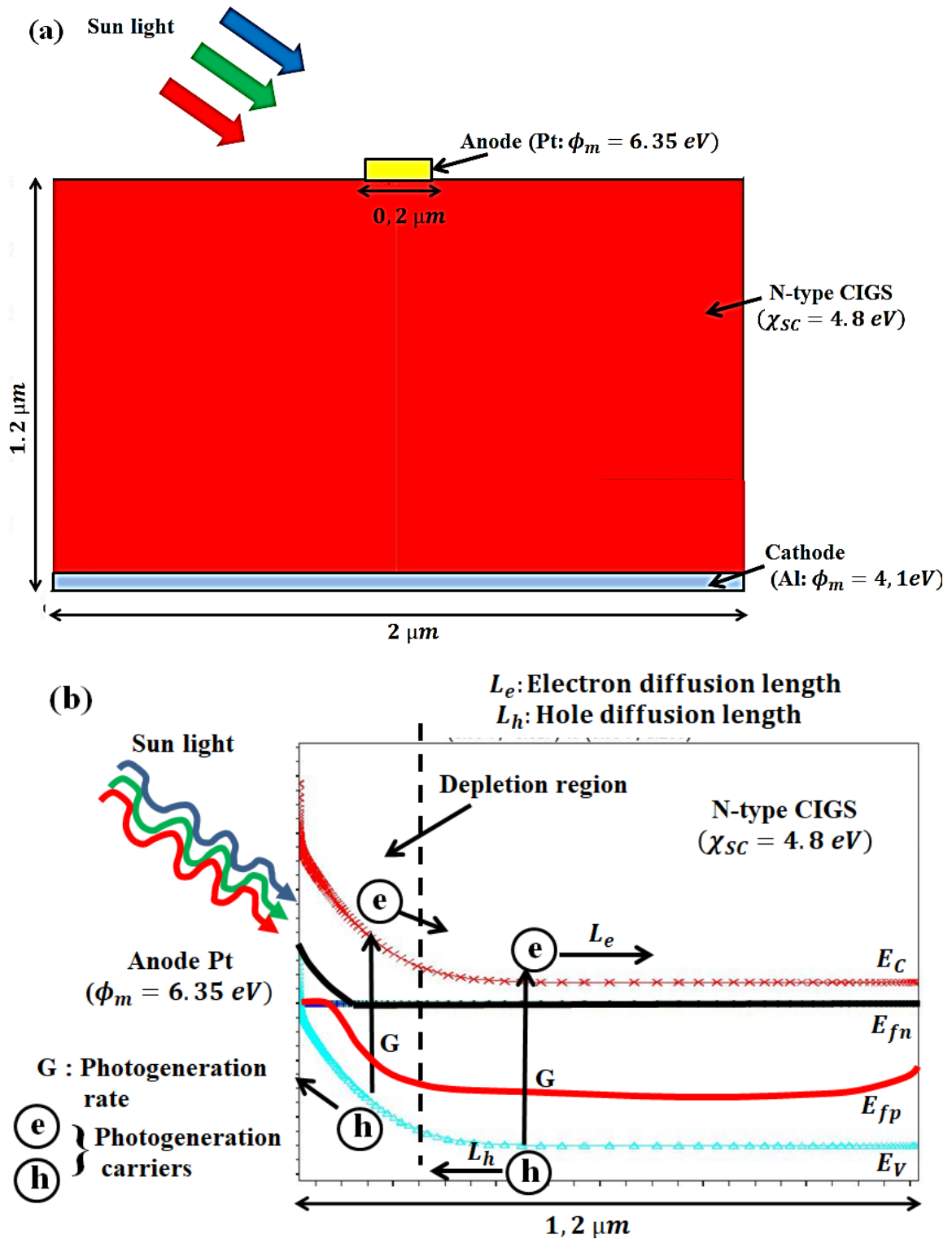


Figure II.5: Schematic diagram of (a) CIGS-based Schottky barrier solar cell, (b) the corresponding band diagram under sunlight illumination and zero bias.



Chapter III :

Silvaco-Atlas Software

III.1 Introduction

SILVACO TCAD is the abbreviation of Silicon Valley Corporation Technology Computer Aided Design. It is a semiconductor process simulation package which consists of several physically based simulators (ATHENA, ATLAS, MERCURY, SSUPREM3 ... etc.) gathered under one environment called DECKBUILD. Each of them simulates different processes [79]. Silvaco Atlas is a software package used to simulate semiconductor devices. It predicts the electrical behavior of a device, which can be modelled in either two dimensions (2D) or three dimensions (3D). The software consists of several integrated programs that work together to achieve the desired results. The main programs are Deckbuild, Devedit, Tonyplot, and Athena, but there are several subprograms that are accessed during simulation that serve more specific functions. These programs give the user the ability to simulate the production process to manufacture a semiconductor device and test its characteristics. There are many models, numerical methods, and types of material built into the program, giving a wide range of functionality to the user. This allows the modeling of anything from simple devices to complex circuits [80, 81].

III.2 Numerical modelling software SILVACO-ATLAS

Atlas is a physically-based device simulator that predicts the electrical characteristics based on physical structures and bias conditions. It does this by applying a set of differential equations based on Maxwell's laws and the semiconductor transport equations to the nodes of a grid overlaid on the device. This allows the simulation of transport carriers through the structure. The three equations derived from Maxwell's laws are Poisson's equation, the continuity equations, and the transport equations. This allows the simulation of transport carriers through the structure [80].

Poisson's Equations relates the electrostatic potential to the space charge density and is given by [80]:

$$\text{div} (\varepsilon \nabla \psi) = -\rho . \quad (\text{III.1})$$

Where ε is the local permittivity, ψ is the electrostatic potential, and ρ is the local space charge. The carrier continuity equations for electrons and holes are defined, respectively, by

$$\frac{\partial n}{\partial t} = \frac{1}{q} \operatorname{div} J_n + G_n - R_n \quad (\text{III.2})$$

$$\frac{\partial p}{\partial t} = -\frac{1}{q} \operatorname{div} J_p + G_p - R_p \quad (\text{III.3})$$

where n and p are the electron and hole concentrations, J_n and J_p are the electron and hole current densities, G_n and G_p are the generation rates for the electrons and holes, R_n and R_p are the recombination rates for electrons and holes, and q is the charge of an electron. The transport equations come from the Boltzmann Transport Equation. Applying approximations and simplifications to this equation results in the drift-diffusion model. For this model [80]:

$$J_n = qn\mu_n E + qD_n \nabla n \quad (\text{III.4})$$

$$J_p = qp\mu_p E - qD_p \nabla p \quad (\text{III.5})$$

where μ_n and μ_p are the electron and hole mobilities, E is the electric field, n is the electron concentration in the conduction band, p is the hole concentration in the valence band, D_n and D_p are the diffusion coefficients for electrons and holes, ∇n and ∇p are the electron and hole concentration gradients.

For the device simulation, Atlas has to solve the total system of equations depending on the models selected. For each model type there are three techniques, decoupled Gummel, fully-coupled Newton, and Block. The Gummel method solves each unknown while keeping the other variables constant. It continues to do this until a stable solution is found. The Newton method solves the total system of equations together to find a solution. The Block method solves the equations using a combination of the Newton and Gummel methods, in that some equations are solved fully coupled and the rest are de-coupled [80, 82].

III.3.DECKBUILD

Deckbuild (see FigureIII.1) is the main program that runs the simulation and calls the associated programs as needed. Deckbuild uses command line code to designate what and how to run. To run Atlas simply type:

Go atlas

This runs the Atlas program within Deckbuild and is usually the first command unless

running one of the other programs, such as Athena, first [80, 82].

The screenshot shows the DeckBuild application window. The title bar reads "DeckBuild - E:/Sujet-masterOctober2021/CIGS_prog-2-2022 - Am2-schottkyCIGS-Cathod-bottom-2carrier.in". The menu bar includes "File", "Edit", "View", "Run", "Tools", "Commands", and "Help". The toolbar contains various icons for file operations and simulation control. The main window is divided into two panes. The top pane, titled "Deck", contains the following code:

```

go atlas

set Xwidth=2
set PDoping=7e15
set Wtunnel=4e-2
set Wsc=1.2
set thickoxi=10
set Woxi=${thickoxi}/1e04

mesh width=0.5e8

x.m l=0      s=0.01
x.m l=${Xwidth}/2  s=0.09
x.m l=${Xwidth}    s=0.01

#y.m loc--$Woxi spa=0.0001
y.m loc=0 s=$Woxi/10

```

The bottom pane shows the output of the simulation, including the version string: "*** this is deckbuild version 4.6.2.R ***" and the command "go atlas". At the bottom center of the window, the word "A T L A S" is displayed in a spaced-out font.

FigureIII.1: Screenshot from Deckbuild.

Once Atlas is initiated, the next step is to set the parameters of the device. Atlas has a specific order (see FigureIII.2) in which the statements must be placed; otherwise the program may not function correctly. Even if it does run, it is possible that certain parameters may not be used, which causes inaccurate results. Generally the format is:

$$\langle \text{STATEMENT} \rangle \langle \text{PARAMETER} \rangle = \langle \text{VALUE} \rangle$$

Statements can have more than one parameter defined. Deckbuild provides many built-in examples of different devices that allow a user to run the simulation and view the results. The examples are helpful to see how the code is written when unsure how it is used [80]

<i>Group</i>		<i>Statements</i>
1. Structure Specification	————	MESH REGION ELECTRODE DOPING
2. Material Models Specification	————	MATERIAL MODELS CONTACT INTERFACE
3. Numerical Method Selection	————	METHOD
4. Solution Specification	————	LOG SOLVE LOAD SAVE
5. Results Analysis	————	EXTRACT TONYPLOT

FigureIII.2: Atlas statement hierarchy, from [82,p.34].

III.4.Main steps of the numerical simulation of Schottky barrier solar cell based on CIGS material using Silvaco-Atlas

In the following sections, we present the main steps applied in Silvaco-Atlas to simulate a Schottky barrier solar cell based on CIGS material. For this example; the total width of the cell is $2\ \mu\text{m}$ and the thickness is $1.2\ \mu\text{m}$. The base layer is n-type CIGS. The Schottky barrier at the metal/semiconductor interface is obtained by making the anode metal (which is situated on the top of the cell) from platinum (Pt). With such a choice; the anode work function (ϕ_m) is higher than the electron affinity (χ_{sc}) of CIGS ($\phi_m = 6.35\ \text{eV} > \chi_{sc} = 4.8\ \text{eV}$). The cathode (from Al) is defined to be neutral (Ohmic contact), and is situated on the bottom of the cell.

III.4.1.Buildingthe device

When building the device to be simulated, the first thing to do is to define the mesh that will be the frame work for the model. A mesh is a collection of triangles that overlays the device (see Figure III.3). Each corner of the triangle is called a node. Nodes are where the equations used to solve for a solution are calculated. When running simulations for a 2D device, there is a limit of 100,000 nodes. A finer mesh results in more triangles, which

give more nodes and increases the resolution of the solution to give more accurate results. The downside to this is that the larger number of calculations require an increase in the time it takes to run the simulation. A coarser mesh has the opposite effect. Fewer triangles, less nodes, and less accuracy, but the run time is shorter. The key to setting up a mesh is to recognize where in the device things are happening (such as at a junction). In these areas a finer mesh is desired so that information is not lost. If the triangles are too big, and the characteristics of the device changes too much, then the calculations will not reflect actual conditions [80].

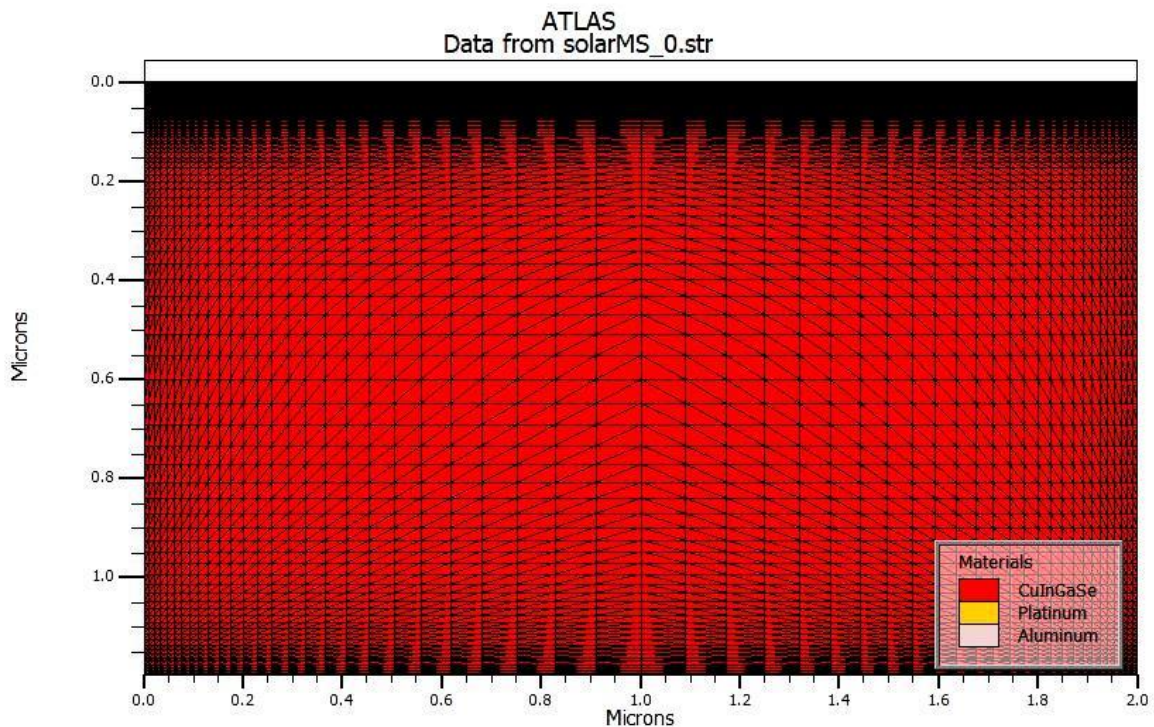


Figure III.3: Mesh example for Schottky barrier solar cell based on n-type CIGS material.

III.4.2. Defining the Structure

There are three ways a structure can be made. The first; is it can be read in by a previously created structure that has been saved in a separate file. This is done by typing the command line:

```
MESHINFILE=<filename>
```

The second way to define a structure is to use the automatic interface feature of Deckbuild. The automatic interface feature allows a user to run Athena or Devedit from within Deckbuild using the “Go Athena” (or “Go Devedit”) command input. Once the structure is built, run Atlas to run the simulation. This is all done within the same window. The automatic part is due to the hand off of structure information between Athena/Devedit and

Atlas. The third way to define a structure is to simply use the command language in Deckbuild to define the structure. The command language for this is:

```
MESHSPACE.MULT=<value>
```

Space.mult is a scaling factor that controls the granularity of the mesh. The default value is one. Any value greater than one gives a coarser mesh, and a value less than one results in a finer mesh. The next statements define where mesh lines in the x and y direction will be:

```
X.MESH LOCATION=<value> SPACING=<value>
```

```
Y.MESHLOCATION=<value>SPACING=<value>
```

These two statements specify the location of the line and the spacing in microns. At least two x and two y statements are needed to define the mesh. If a different spacing is used, Deckbuild automatically inserts extra lines to allow for a gradual transition. An alternate method to the space.mult command is to use the automatic mesh function:

```
MESHAUTO
```

This statement is followed by x.mesh statements. When using the automatic mesh there is no need to use the y.mesh command inputs because the y-axis mesh is automatically determined based on the region statements.

III.4.3.Regions

Once the mesh has been defined, the next step is to define the regions. If a region has been imported from Athena or Devedit, this may not be necessary unless more regions are needed. A typical region statement is:

```
REGIONNUMBER=<integer><material_type><position_parameters>
```

When using the command line, these regions are numbered, starting with one, up to a maximum of 1000 for a device. The user should number the regions; otherwise, Deckbuild automatically numbers them with consecutive numbers. Awkward numbering can be confusing when observing results because the region numbers in the code will not match those in the plots. The material type parameter defines the type of material for the region. The properties for many materials are already stored in the program. They can be changed in a material statement further down in the code once the entire mesh is complete and doping concentrations are defined. The position parameter defines the location in microns of the region. One way to define the location is with x.min, x.max, y.min and y.max statements that look like:

X.MIN=<location>X.MAX=<location>Y.MIN=<location>Y.MAX=<location>

The x.min lists the minimum position in the x-direction, and x.max lists the maximum position in the x-direction. The same holds true for the y-axis. It should be noted that the x-axis starts at zero on the left and is maximum on the right, just like a standard x-y Cartesian coordinate system. The y-axis, however, is opposite what one might expect. The y.min starts at zero on the top, and downward is maximum (see Figure III.4).

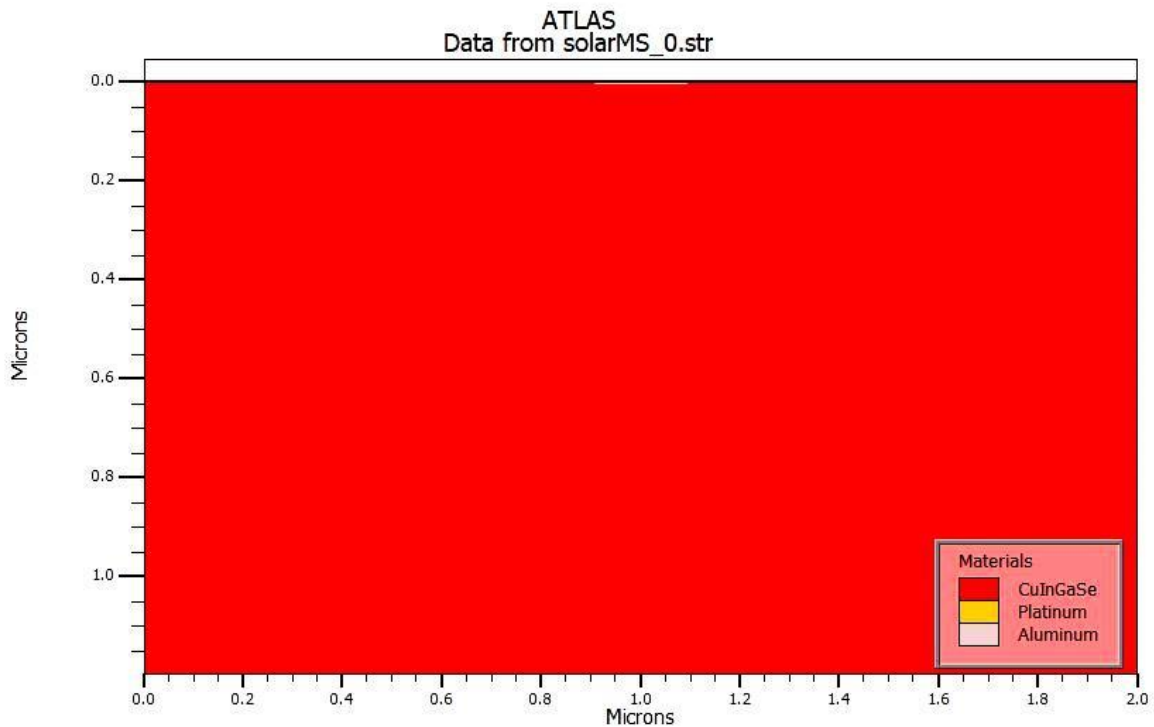


Figure III.4: Tonyplot screenshot showing the layout of the x and y-coordinate system in Atlas for Schottky barrier solar cell based on n-type CIGS material.

It is important to remember the axis convention since many aspects of the program are position dependent and need to be accurate to ensure proper results. It would not be wise to define a light source underneath a solar cell when trying to simulate its output. Likewise, it would prove confusing for others trying to understand the code and simulation if the standard convention is not followed. It is not always necessary to define both a maximum and minimum for a particular direction. Defining only one suffices, and the program extends the region to the dimensions of the mesh. If $x.min=0.9$ was defined but no $x.max$, then the region starts at **0.9** microns and extend all the way to the maximum x-value defined in the mesh. The same thing occurs for they-direction as long as $y.max$ was defined for the mesh, which is not the case when using the auto mesh feature.

III.4.4. Electrodes

Once the regions and materials are specified, the electrodes can be defined. There must be a minimum of one electrode (that touches the semiconductor material) defined for the program to work. Up to 100 electrodes can be specified, and if any of the defined electrodes are given the same name, then the electrodes are considered electrically connected. A typical electrode statement is:

```
ELECTRODENAME=<electrode name><position_parameter>
```

If no y-coordinate is given, then the electrode is placed at the top of the device. The top, bottom, right and left parameters can be used to define the location as well. Figure III.5 shows the electrode positions in the Schottky barrier solar cell based on n-type CIGS material.

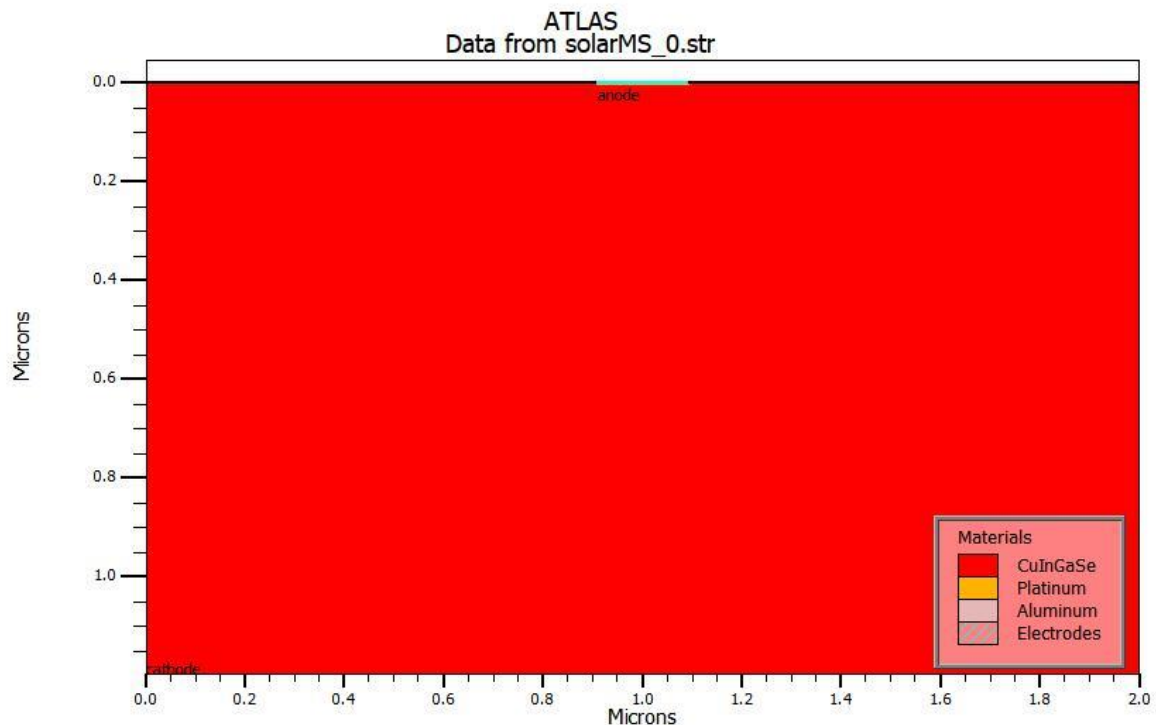


Figure III.5: Electrode positions of the Schottky barrier solar cell based on n-type CIGS material.

The anode metal (platinum: Pt) is placed on the top of the cell; the electrode statement for this is:

```
Electrode name=anode material=platinum top x.min=0.9 length=0.2.
```

The anode metal fulfills the Schottky contact condition. The CONTACT statement is used to specify the metal work function of the anode as follows:

```
contact name=anode WORKFUN=6.35
```

The cathode (from aluminum: Al) is placed on the bottom of the cell and is assumed to be

ohmic (neutral), so the electrode and contact statements are respectively as follow:

```
electrode name=cathode material=Aluminum bot
```

```
contact name=cathode neutral
```

III.4.5.Doping

Doping parameters are specified next and are generally in the form:

```
DOPING<distribution_type><dopant_type><postion_parameter>
```

The distribution type can be uniform, Gaussian, or complementary error function. The dopant type can be specified as n.type or p.type, and the concentration amount can be defined. The position parameter can be specified by region number or the minimum/maximum parameters. For the n-type CIGS base layer with doping concentration $N_d = 7 \times 10^{15} \text{ cm}^{-3}$, the doping statement is :

```
doping region=1 uniform n.type conc=7e15
```

III.4.6.Modifying Parameters

After the mesh, geometry, and doping parameters have been defined, the characteristics of the electrodes can be changed, the material parameters modified, and the physical models chosen. The electrodes in contact with a semiconductor material are ohmic by default. As we indicated in the electrode section (section III.4.4), defining a work function with the contact statement causes it to be treated as a Schottky contact. Using the materials statement allows the user to change properties of the specified material such as electron mobility, band gap, or carrier lifetime. Specifying region after the material statement changes the material properties for the material in only the specified region and is useful when multiple regions are made of the same material but not all of them need to be changed. To specify the physical models, use the models statement followed by the name of the models. Adding print in the model statement displays the models and parameters used during the simulation into the runtime output, and allows the user to ensure the correct parameters were used. The statement of the physical models used in simulation is as follows:

```
models temperature=300 print conmob srh Fermi ni. fermi auger bgn UST.
```

The signification of each model will be presented in chapter IV.

III.4.7.Numerical Solutions

The next thing to define is the numerical solution which tells the program which

numerical methods to use when calculating solutions for the device. There are three methods that Deckbuild uses. They are Gummel, Block, and Newton which are specified after the method statement. Each numerical method uses a different approach to solving the equations. The Gummel method solves for each unknown while keeping the variables constant. It continues doing this until a stable solution is found. The Newton method solves the total system of unknowns together, and the Block method solves some of the equations by the Gummel way and the rest by the Newton way. Generally, the Newton method is preferred and is the default if the method statement is not used. For our example we used Newton method through the statement:

```
method newton carriers=2.
```

which means that Atlas solves both electron and hole continuity equations.

III.4.8.Obtaining Solutions

To obtain solutions for the created device, the user has the options of using DC, AC, small signal, and transient voltages for the calculations. Once the voltages for the electrodes are defined, Atlas calculates the currents and the internal quantities. To set the voltage of an electrode named anode:

```
SOLVEVANODE=1.0
```

This sets the anode voltage to one volt. Multiple solve statements can be used in succession to ramp up the voltage or a sweep can be used:

```
SOLVE VANODE=0 VSTEP=0.01 VFINAL=1 NAME=anode
```

```
SOLVEVSTEP=0.02 VFINAL=1.6NAME=anode
```

This sweeps the voltage from zero volts to one volts in 0.01volt increments. The second solve statement sweeps from one volts to 1.6 volts in 0.02volt increments. Atlas remembers the last voltage of the electrode, one volts after the first solve statement and 1.6volts after the second solve statement. If an anode voltage was stated in the second solve statement, then the starting voltage for the sweep is instead set to this value. When Atlas attempts to find a solution, the program uses an initial guess for the variables to be evaluated at each bias point. The initial guess usually comes from the two previous solutions, and if none are available convergence problems can arise. When previous solutions are not available, Atlas uses the doping profile to make the initial guess for potential and carrier concentration. To do this the initial solution must be made at zero bias which is done by:

SOLVEINIT

If this statement is not included, Atlas automatically evaluates an initial solution prior to the first solve statement.

III.4.9.Results

When running the simulation it is useful to open a log file to save the terminal characteristics calculated by Atlas. To save the terminal characteristics, open a log file prior to any solve statements:

```
LOGOUTFILE=<filename>
```

This opens a log file and saves it under the chosen file name. All outputs from solve statements are saved in this log file until either another log statement is opened under a different file name or the log is closed by using the log statement with the off parameter. Once the simulation is complete, this log file can be used in Tonyplot to view the results. The electrical current values stored in the log file are generally in Amperes per micron, because Atlas is a 2D simulator and sets the z-axis to be one micron. If a width dimension is specified, the cylindrical coordinate system is used, or when simulating a 3D device, then the units are in Amperes. The log file is also useful for extracting parameters by using the extract command:

```
EXTRACTINITINF=<filename>
```

This uses the specified file to perform the extraction. If a log file is currently open, then there is no need to specify a file, as the extract statement defaults to the currently open log file [80]. Calculation can be performed on the extracted data and the results saved in a file for later use such as viewing in Tonyplot. The results from the extraction display in the run-time output and are stored in a file called results.final. The user can also specify a different file in which to store the results by adding a different file at the end of the extract statement:

```
EXTRACT.....DATAFILE=<filename>
```

Another type of file that provides utility is a solution or structure file, which contains an image of the device at a particular bias point and gives the user the ability to view several parameters of the device [80]. Having the ability to view the device parameters allows a user to see what is going on at that particular point in the simulation. These parameters can greatly assist in troubleshooting the simulation by giving the user an idea of what part of the code to examine for problems [80].

III.4.10. Tonyplot

Tonyplot is a graphical tool used to plot data obtained from device simulations. It can be called directly in Deckbuild by typing:

```
TONYPLOT -overlay
```

If the file is a log file, Tonyplot displays the data in an x-y plot. If the file is a structure file, the information is displayed as a 2D mesh plot [80].

III.4.11. Luminous

Luminous is a general purpose program integrated into Atlas that is used for light propagation and absorption. Luminous calculates the optical intensity within a device and uses this to find the photo-generation rates used in the solution equations. There are four physical models for light propagation. Ray tracing is a general method for resolving non planar geometries and is generally the preferred starting point but ignores the effects of diffraction and coherence. The transfer matrix method is a 1D method and is recommended for large area devices that includes interference effects. The beam propagation method is a general 2D method that is computationally intensive because it includes diffraction effects. Finally, the finite-difference, time-domain method is a general 2D and 3D method that is the most computationally intensive because it includes both diffraction and coherence effects [80].

III.4.12. Solar cell simulation

The light propagation and absorption properties of Luminous make it ideal for simulation of solar cells. The user has the ability to define the spectra used in the simulation or to use the built-in spectra for AM0 and AM1.5. To define a beam statement:

```
BEAM NUM=1 AM1.5 X.O=1 Y.O=-1.5 ANGLE=90 \
WAVEL.START=0.200 WAVEL.END=2.5 WAVEL.NUM=200
```

Here the AM1.5 spectrum is specified and is sampled between 0.2 microns and 2.5 microns with 200 samples. The propagation model for the light can also be stated in the beam statement. To get the simulation data, solve statements are used. The first statement is usually:

```
SOLVEB1=1.0
```

This turns on the light beam. In this example, the value one corresponds to full intensity. Values less than one reduce the intensity and larger values increase the intensity, such as

with a solar concentrator. Once the beam is turned on, it is necessary to open a log file to save the current and voltage characteristics and set the voltage of one of the electrodes. Extract statements can also be used to pull pertinent data and solve for common characteristics of solar cells like the fill factor, efficiency, maximum output power, open circuit voltage, and short circuit current, which are shown in the following example:

```
Extract init in file="solarexMS_fwd_light.log"
```

```
extract name="ISC_[mA/cm^2]" y.val from curve(v."anode",i."cathode"*1e3) where
x.val=0.0
```

```
extract name="VOC_[V]" x.val from curve(v."anode",i."cathode"*1e3) where y.val=0.0
```

```
extract name="Vmax_[V]" x.val from curve(v."anode",v."anode"*i."cathode") where
y.val=max(v."anode"*i."cathode")
```

```
extract name="Imax_[mA/cm^2]" x.val from
curve(i."cathode"*1e3,v."anode"*i."cathode") where y.val=max(v."anode"*i."cathode")
```

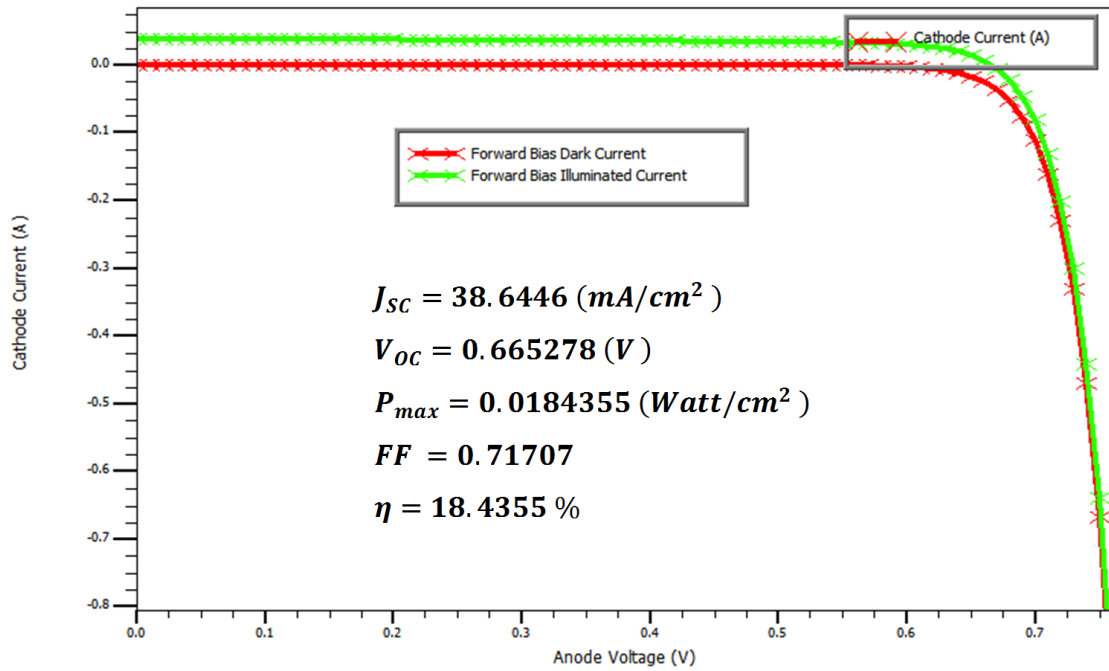
```
extract name="power" curve(v."anode",(v."anode"*i."cathode"))
outfile="powerlight_MS.dat"
```

```
extract name="Pmax" max(curve(v."anode", (v."anode" * i."cathode" )))
```

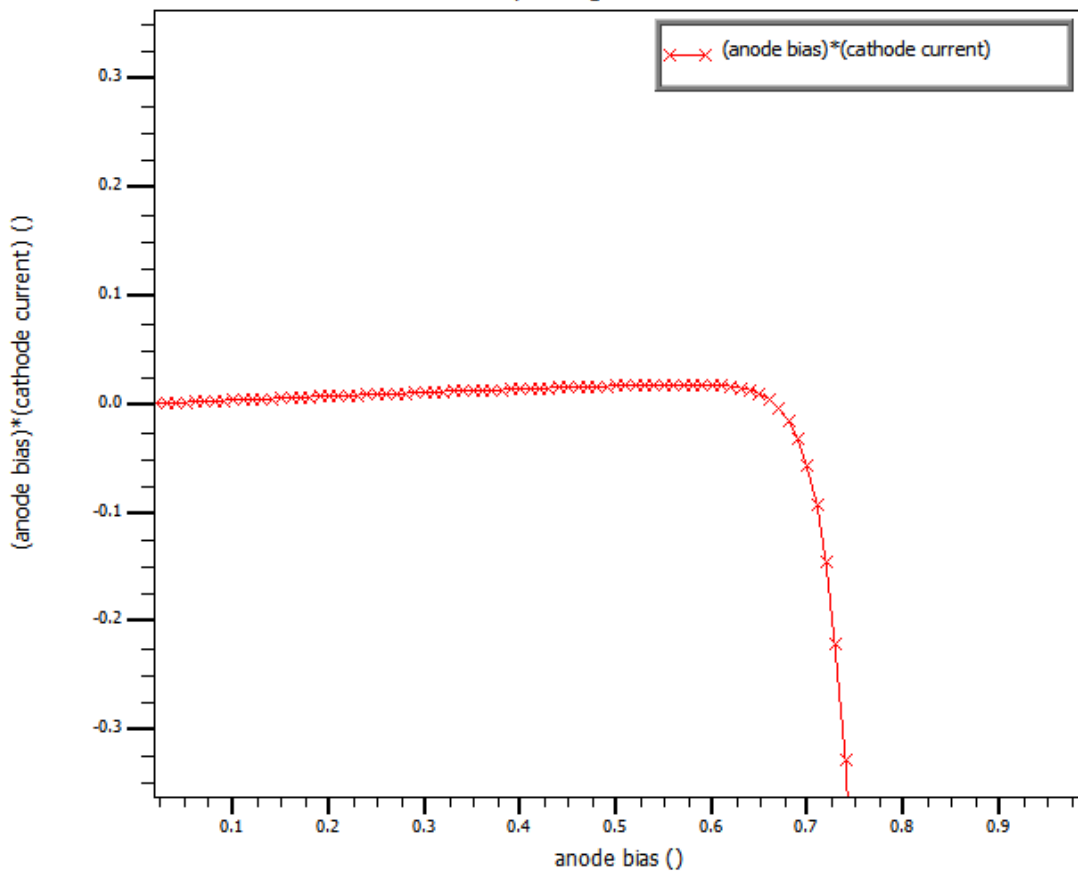
```
extract name="FF"("$Vmax_[V]"*$Imax_[mA/cm^2])/$VOC_[V]"*$ISC_
[mA/cm^2]"
```

```
extract name="EFF_[%]" $Vmax_[V]"*$Imax_[mA/cm^2]"
```

With the graphical tool Tonyplot, we can plot the data obtained from device simulations as shown on Figures III.6 and III.7 which show, respectively, the current density-voltage ($J - V$) and the power-voltage ($P - V$) characteristics obtained from the simulation of the Schottky barrier solar cell based on n-type CIGS material, in the dark and illumination conditions. The values of the photovoltaic output parameters of the cell, computed by Silvaco-Atlas, are also displayed in Figures III.6.



FigureIII.6: Simulated $J - V$ characteristics of the Schottky barrier solar cell based on n-type CIGS material, in the dark and illumination conditions with AM1.5 spectrum.



FigureIII.7: Simulated $P - V$ characteristics of the Schottky barrier solar cell based on n-type CIGS material, in illumination conditions with AM1.5 spectrum.



Chapter IV :

Study Of Schottky Barrier Solar
Cell Based On CIGS Material

IV.1. Introduction

In this chapter, we will investigate the Schottky barrier solar cell based on n-type Copper Indium Gallium Selenide (Cu(In,Ga)Se_2 : CIGS) material, exposed to the AM1.5 standard spectrum at ambient temperature (300°K). The anode metal, situated on the top of the cell, should have a work function (ϕ_m) higher than the electron affinity (χ_{sc}) of the semiconductor (n-type CIGS) to form Schottky contact with appreciable Schottky barrier height. The metals used in this study to satisfy this condition are respectively Pt ($\phi_m = 6.35 \text{ eV}$), Au ($\phi_m = 5.47 \text{ eV}$) and Ni ($\phi_m = 5.22 \text{ eV}$) [83]. The cathode (Al) is defined to be neutral (Ohmic contact). Two solar cells are considered in this study; for the first one (sample A), the cathode is situated on the bottom of the cell giving a sandwich configuration. For the second one (sample B), two cathode electrodes are located on the top of the cell giving a coplanar configuration. The investigation is carried out using the numerical simulation software SILVACO-ATLAS, which allows the calculation of all the internal parameters of the solar cell such as the distribution of the band diagram, the electron and holes concentrations...etc. The external parameters are also be calculated such as the current density-voltage ($J - V$) and the provided power - voltage ($P - V$) characteristics under illumination, which allow the extraction of the photovoltaic output parameters of the solar cell namely the short circuit current density J_{sc} , the open circuit voltage V_{oc} , the fill factor FF , the maximum power P_{max} provided by the cell and the photovoltaic conversion efficiency η of the cell. For the two considered solar cells, we investigate the thickness variation effect of the n-type CIGS layer in the range $[0.5\text{-}8\mu\text{m}]$, the n-type doping concentration (N_d) effect of the CIGS layer in the range $[10^{12} - 10^{19} \text{ cm}^{-3}]$, and the work function (ϕ_m) effect by changing the anode metal (Pt, Au and Ni).

IV.2. Description of the studied Schottky barrier solar cell based on CIGS

The two studied solar cells (samples A and B) are presented respectively in cases (a) and (b) of figure IV.1. The corresponding spatial mesh is shown on figure IV.2.

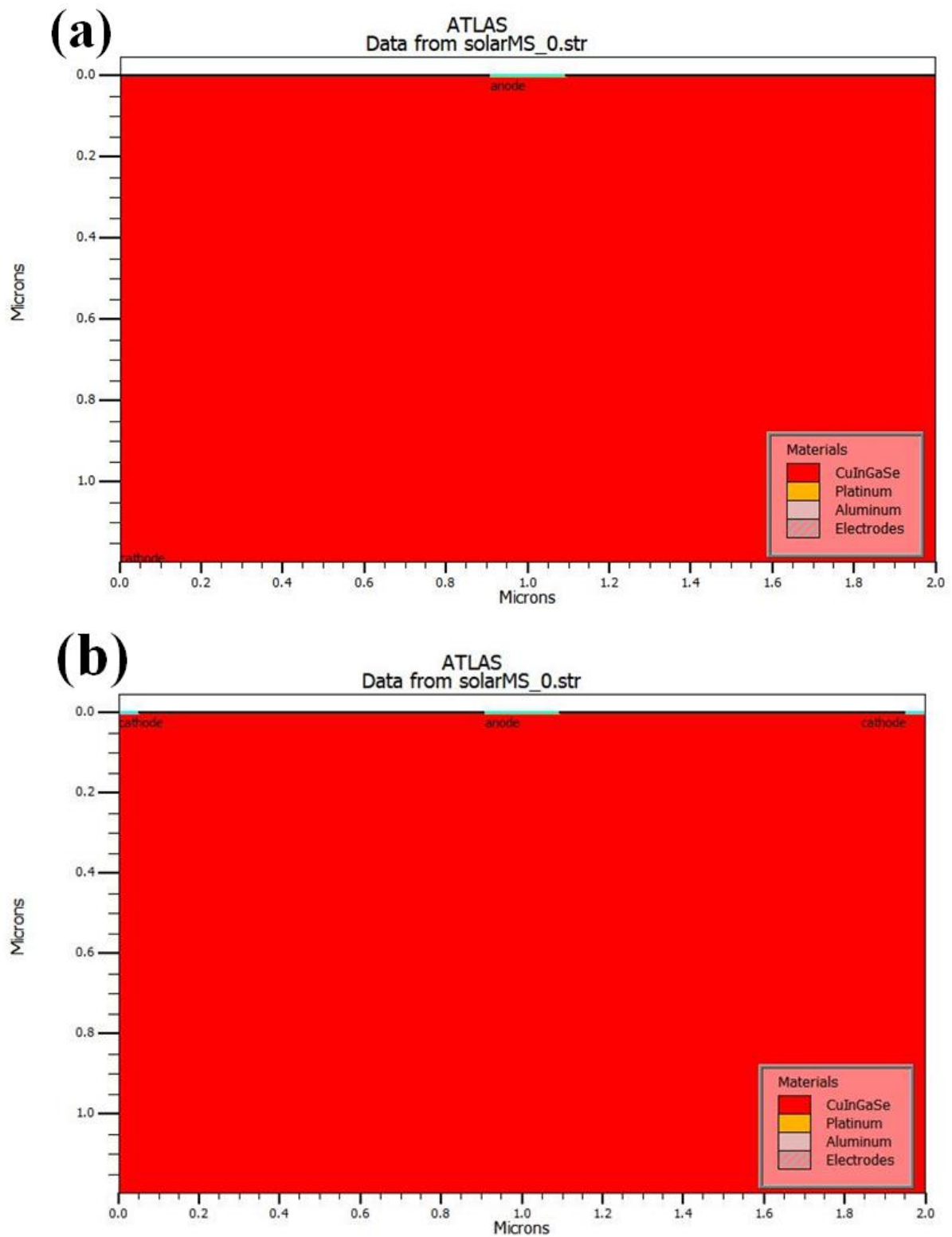


Figure IV.1: Structure of the Schottky barrier solar cell based on CIGS : (a) sandwich configure (sample A), (b) coplanar configuration (sample B).

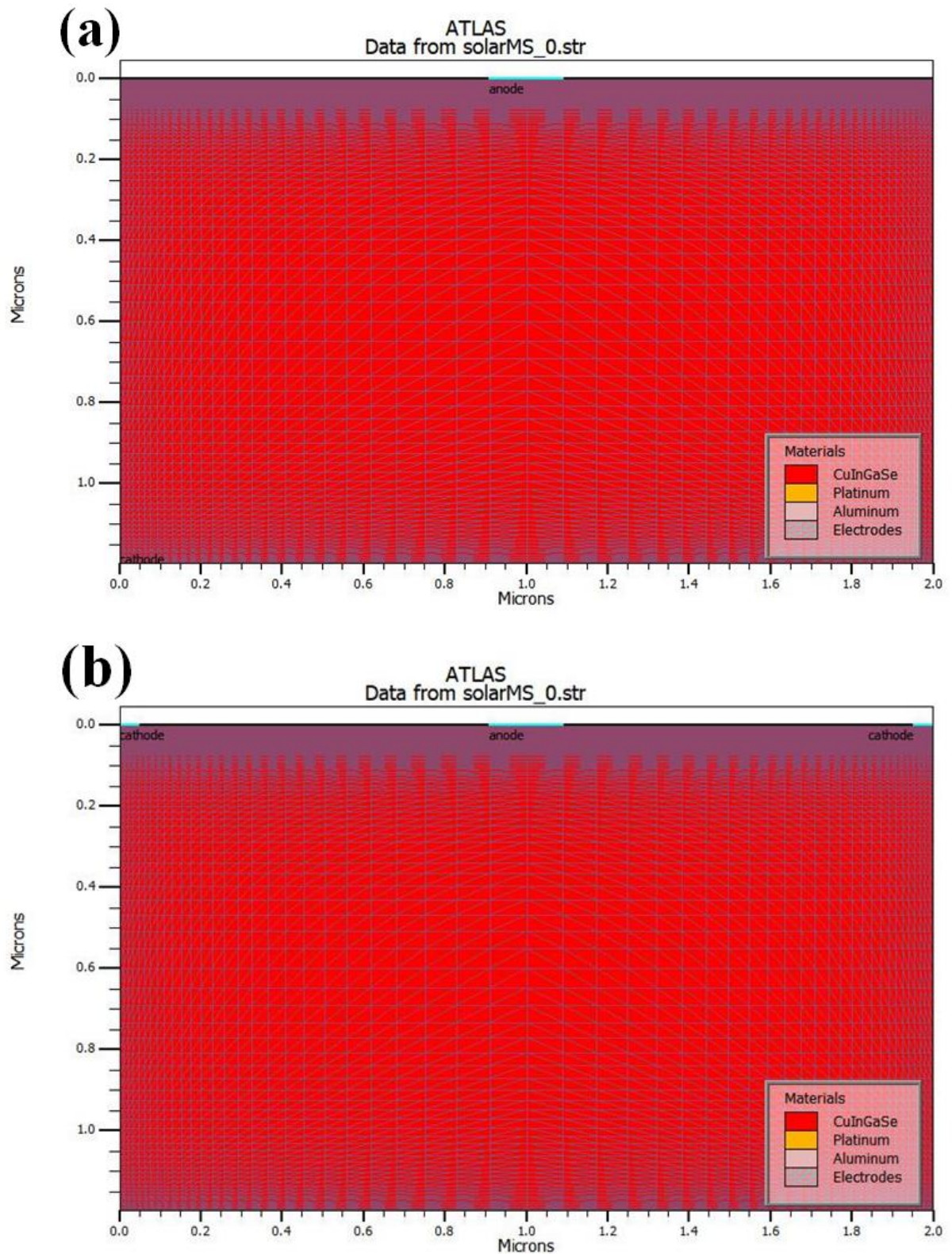


Figure IV.2: Two dimensional (2D) mesh of the Schottky barrier solar cell based on CIGS: (a) sandwich configuration (sample A), (b) coplanar configuration (sample B).

The optical constants, presented by the absorption coefficient (α) and the optical index of refraction (n), are measured data saved in Silvaco data base, and are presented in figure IV.3 (cases (a) and (b) respectively) for the different layers of the studied Schottky barrier solar cell based on CIGS. The anode metal for this case is Pt ($\phi_m = 6.35 \text{ eV}$).

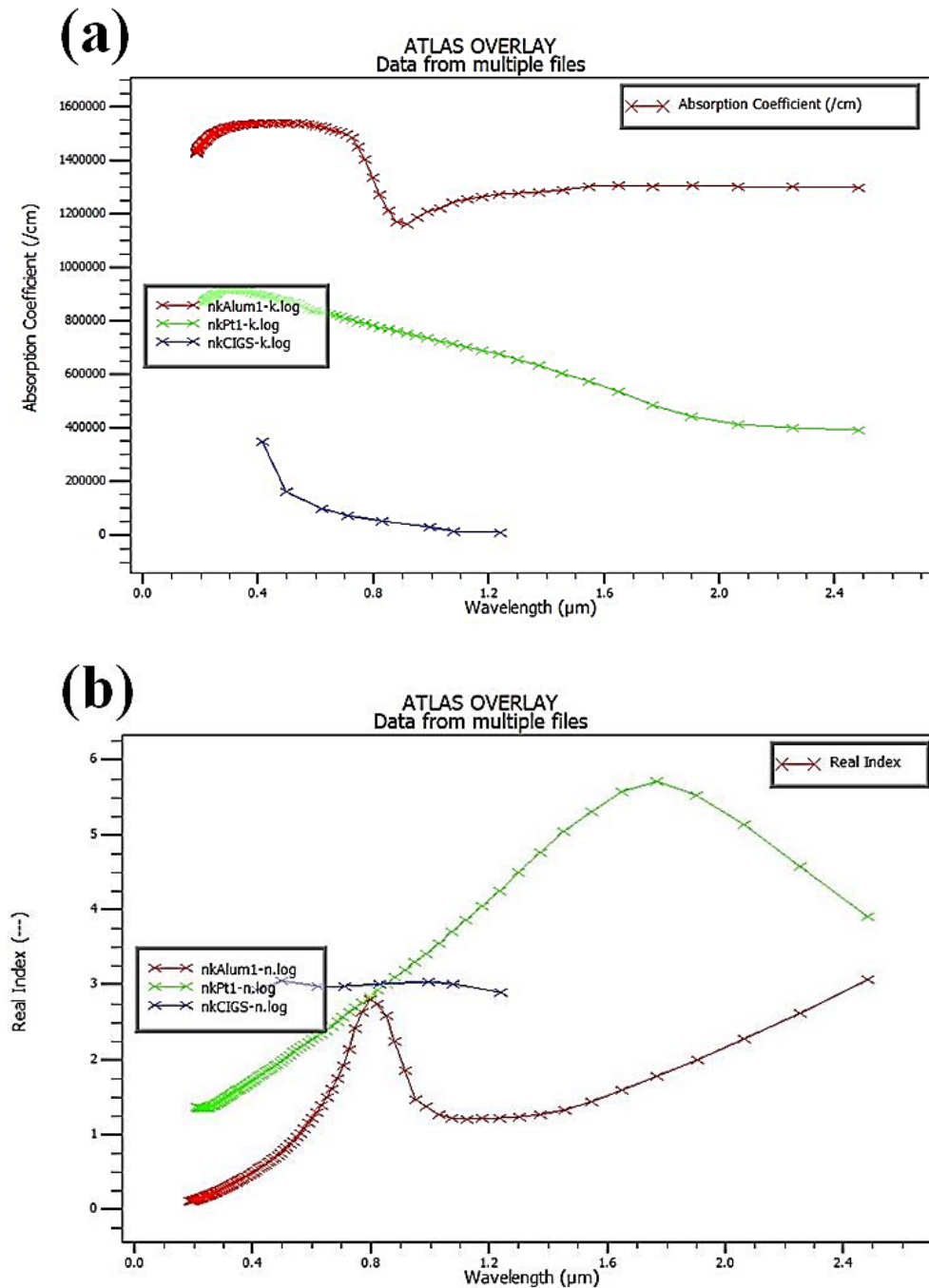


Figure IV.3: Optical spectre of: (a) absorption coefficient (α) and (b) index of refraction (n) in the different layers of the studied Schottky barrier solar cell based on CIGS.

Using Silvaco-Atlas, the Poisson equation, together with current density and continuity equations, are solved simultaneously to obtain the distribution of the electrical potential and carrier density along the solar cell structure; essentially along the base layer (CIGS). The determination of these internal parameter distributions allows the calculation of current density of electrons and holes, and so the current density – voltage ($J - V$) electrical characteristic of the cell, either in dark condition or under illumination.

The physical models that we used to simulate the carrier transport through the device are stated via Silvaco-Atlas as follows:

models temperature=300 print conmob srh fermi ni. Fermi auger bgn UST

Table IV.1 gives a brief description of each employed model [82].

Table IV.1:Brief description of the employed models in simulation[82].

Model	Syntax	Description
Concentration Dependent	conmob	Specifies that a concentration dependent mobility model is used for CIGS. This model is a doping versus mobility table valid for 300K only.
Shockley-Read-Hall	srh	Specifies Shockley-Read-Hall recombination using fixed lifetimes.
Fermi-Dirac	fermi	Specifies that Fermi-Dirac carrier statistics be used.
n_i calculation using Fermi-Dirac statistics	ni.fermi	Includes the effects of Fermi statistics into the calculation of the intrinsic concentration in expressions for SRH recombination.
Auger	Auger	Specifies Auger recombination.
Band gap narrowing	bgn	Specifies band gap narrowing model.
Universal Schottky tunneling model	UST	Enables the universal Schottky tunnelling model .

Chapter IV : Study Of Schottky Barrier Solar Cell Based On CIGS Material

Table IV.2 gives the simulation parameters of the studied Schottky barrier solar cell by Silvaco-Atlas[82]; where mass.tunnel specifies the effective mass for band to band tunneling, me.tunnel and mh.tunnel specify the electron and hole effective masses for tunneling used in the universal Schottky tunneling model, d.tunnel specifies the maximum tunneling distance for the universal Schottky tunneling model.

Table IV.2: Input parameters of the studied Schottky barrier solar cell based on CIGS simulated by Silvaco-Atlas [82].

Parameters		Value
Cell width, x_{tot} (μm)		2
Anode width (μm)		0.2
Cathode width (μm)	Sample (A)	2
	Sample (B) (two electrodes)	0.05 (each one)
Thickness, d (μm)		0.5-8
Doping concentration (n-type), N_d (cm^{-3})		$10^{12} - 10^{19}$
Energy gap, E_g (eV)		1.15
Permittivity, ϵ_r		13.6
Affinity, χ_{sc} (eV)		4.8
Electron mobility, μ_n ($cm^2V^{-1}s^{-1}$)		Conmob
Hole mobility, μ_p ($cm^2V^{-1}s^{-1}$)		Conmob
Effective density at E_C , N_C (cm^{-3})		2.2×10^{18}
Effective density at E_V , N_V (cm^{-3})		1.8×10^{19}
Intrinsic carrier concentration, n_i (cm^{-3})		1.38×10^9
Band-to-band tunnelling Parameters	mass.tunnel	0.25
	me.tunnel	0.197
	mh.tunnel	0.801
	d.tunnel (μm)	0.04
Recombination Parameters	τ_{n0} (s)	10^{-7}
	τ_{p0} (s)	10^{-7}
Anode work function(ϕ_m (eV))	Pt	6.35
	Au	5.47
	Ni	5.22

IV.3. Schottky Contact and the Universal Schottky Tunneling (UST) Model

To specify a Schottky contact [84, 82], we specify a work function (ϕ_m) using the WORKFUN parameter of the CONTACT statement. In practice, the work function (ϕ_m) is defined as :

$$\phi_m = \phi_B + \chi_{sc} \quad (IV.I)$$

Where ϕ_B is the barrier height at the metal/semiconductor interface in eV.

We can enable the thermionic emission model by specifying any of the following parameters

of the CONTACT statement: SURF.REC, E.TUNNEL, VSURFN, VSURFP, or BARRIER.

For example, to specify a the rmoinic emission Schottky contact with tunneling and barrier lowering, the command would be:

CONTACT NAME=ANODE SURF.REC E.TUNNEL BARRIER.

In the Universal Schottky Tunneling (UST) Model [85, 86], the tunneling current is represented by localized tunneling rates at grid locations near the Schottky contact. For electrons, this is illustrated in Figure IV.4.

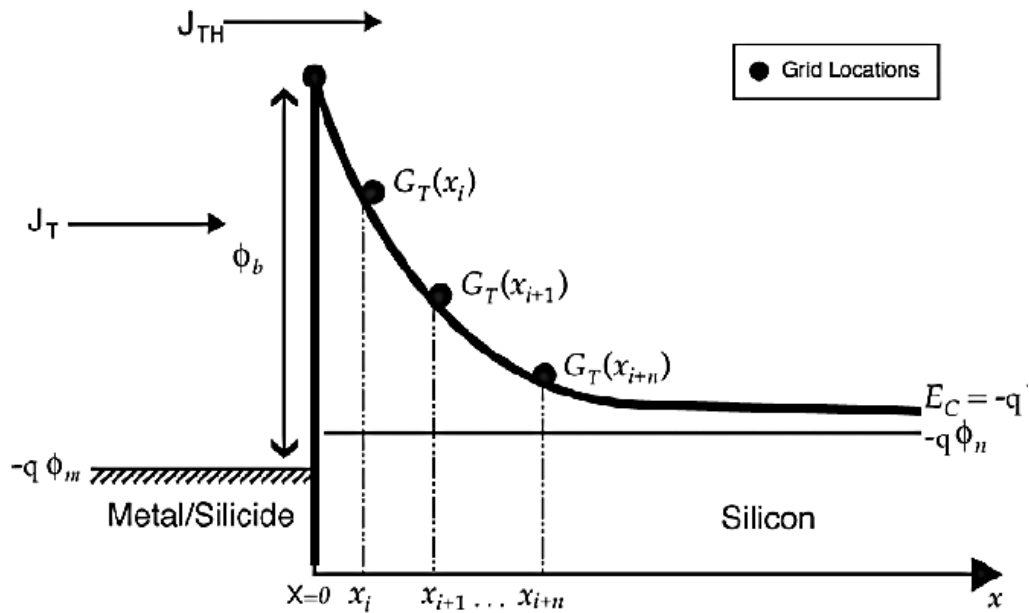


Figure IV.4: Local tunneling generation rate representation of the universal Schottky tunneling model [82].

The tunneling component of current can be described by Eq.(IV.2):

$$J_T = \frac{A^* T_L}{k_B} \int_E^\infty \Gamma(E') \ln \left[\frac{1+f_s(E')}{1+f_m(E')} \right] dE \quad (IV.2)$$

Here, J_T is the tunneling current density, A^* is the effective Richardson's coefficient, T_L is the lattice temperature, $\Gamma(E)$ is the tunneling probability, $f_s(E)$ and $f_m(E)$ are the Maxwell-Boltzmann distribution functions in the semiconductor and metal and E is the carrier energy.

The tunneling probability $\Gamma(x)$ can be described by Eq.(IV.3):

$$\Gamma(x) = \exp\left[\frac{-2\sqrt{2m^*}}{\hbar} \int_0^x (E_C(x') - E_C(x)) dx'\right] \quad (\text{IV.3})$$

In Eq.(IV.3), m^* is the electron effective mass for tunneling, and $E_C(x)$ is the conduction band edge energy as a function of position(x). Assuming linear variation of E_C around a grid location, Eq.(IV.3) can be reduced to Eq.(IV.4)[82]:

$$\Gamma(x) = \exp\left[\frac{-4\sqrt{2m^*}x}{3\hbar} (E_{fm} + q\phi_b - E_C(x))^{1/2}\right] \quad (\text{IV.4})$$

Where E_{fm} is the Fermi level in the contact and ϕ_b is the barrier height.

To enable the universal Schottky tunneling model, we should specify UST on the MODEL Sstatement. We are also required to specify SURF.REC on the CONTACT statement for each contact that we wish the model to apply. Once enabled, this model automatically applies to both electrons and holes. For a given grid point, however, the model will only apply to one carrier according to the relative direction of the local electric field [82].

Once we enable the model, for each electrode with thermionic emission, the model will be applied to all grid points within a specified distance of the electrode, To specify this distance,

We use D.TUNNEL parameter of the MATERIAL statement. The default value of D.TUNNEL is 10^{-6} in units of cm [82].

IV.4.Results and discussion:

Figure IV.5 shows, the band diagram of the Schottky barrier solar cell based on CIGS (sample A) with platinum (Pt) anode metal ($\phi_m = 6.35 \text{ eV}$). The cell thickness is $d = 1.2 \mu\text{m}$ and the doping concentration of the CIGS base layer is $N_d = 7 \times 10^{15} \text{ cm}^{-3}$.

Case (a) of figure IV.5 corresponds to the thermal equilibrium; case (b) corresponds to the short – circuit condition under AM1.5 spectrum illumination.

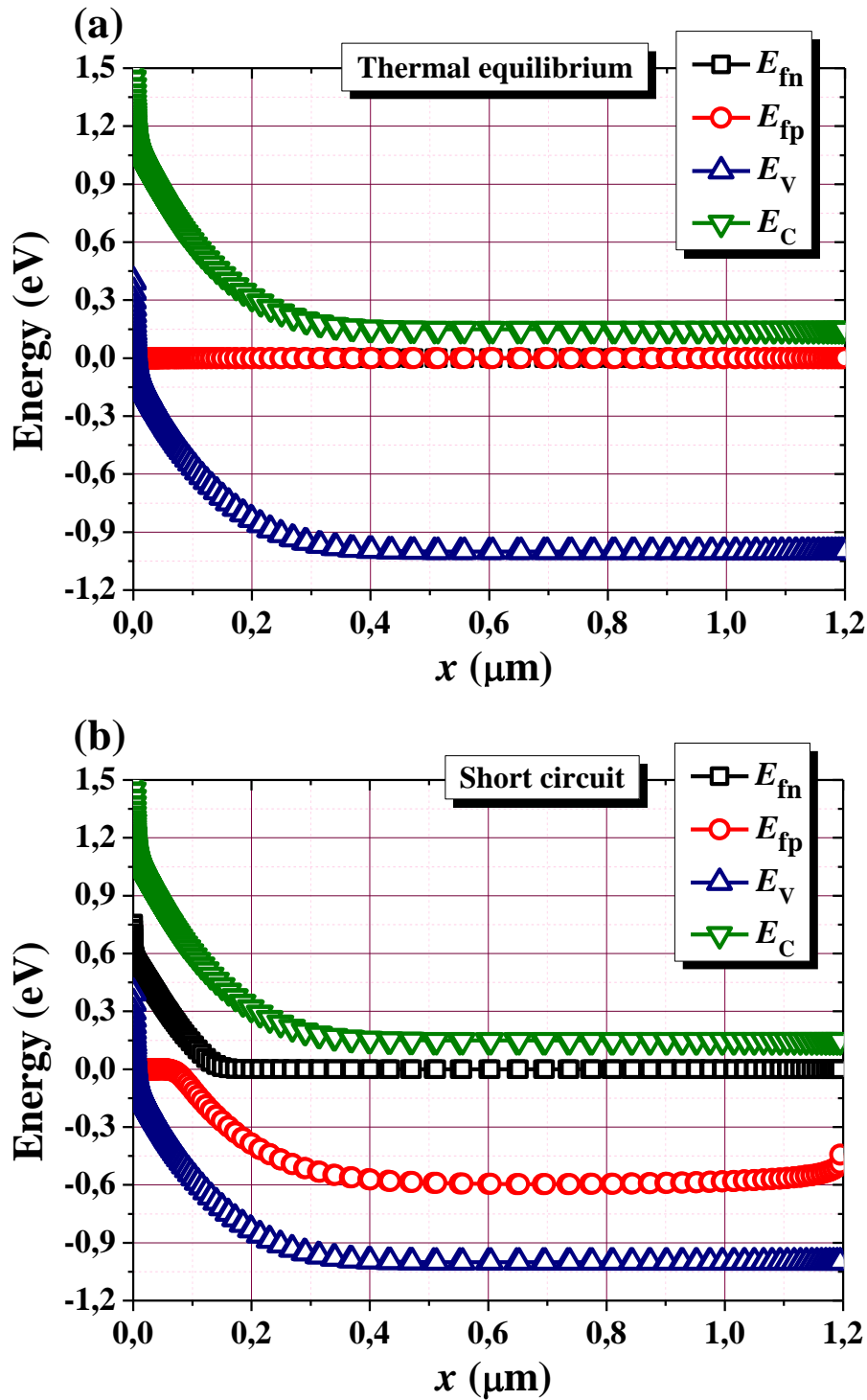


Figure IV.5 Band diagram of the Schottky barrier solar cell based on CIGS (sample A) with platinum (Pt) anode metal ($\phi_m = 6.35 \text{ eV}$): (a) at thermal equilibrium, (b) at short circuit condition.

As the anode work function is higher than the electron affinity of CIGS ($\phi_m = 6.35 \text{ eV} > \chi_{sc} = 4.8 \text{ eV}$), the bands of CIGS at the (Pt/ CIGS) interface bend up ward at zero bias. The splitting of the quasi-Fermi levels, at short-circuit condition, shows a significant

increase, by photo-generation, of the electron carrier density in the depletion region of Schottky barrier. However, the hole carrier density increases significantly almost along the neutral region of the base layer (n-type CIGS). This is clearly showed by FigureIV.6 which displays, the carrier density distributions in the Schottky barrier solar cell based on CIGS, at thermal equilibrium and short-circuit condition.

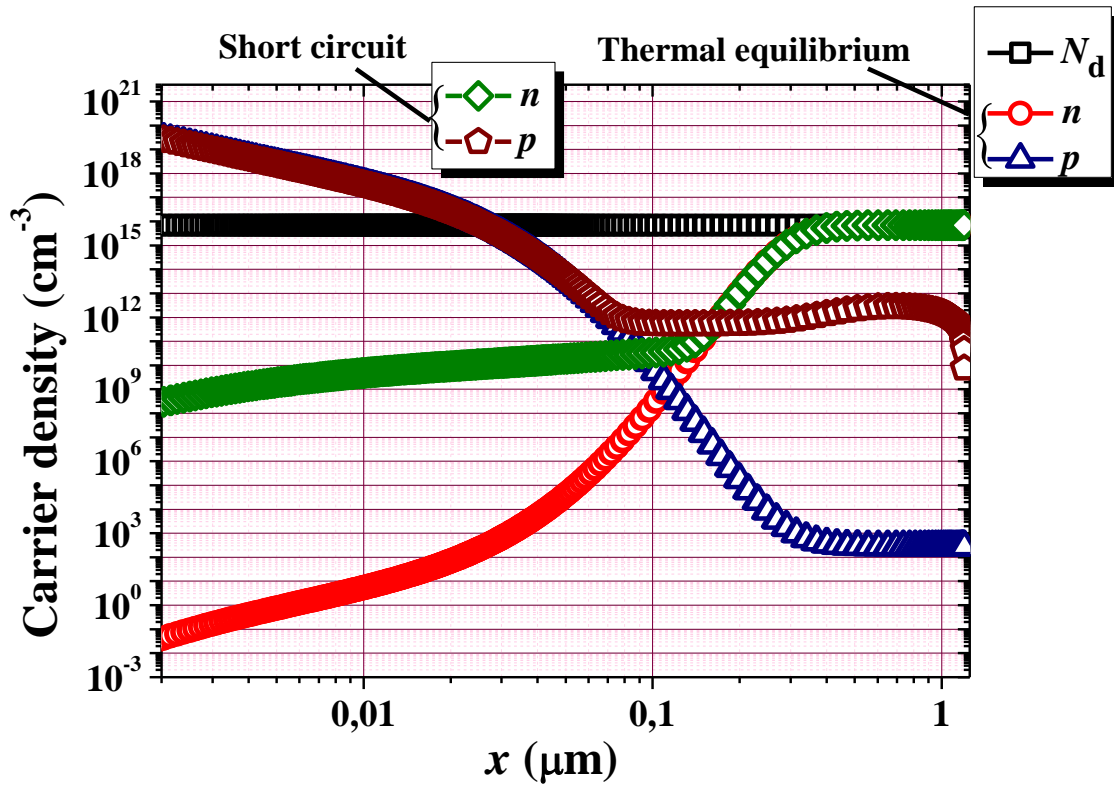


Figure IV.6: Carrier density distributions in the Schottky barrier solar cell based on CIGS (sample A) at thermal equilibrium and short circuit condition.

Figure IV.7 presents the simulated current density – voltage ($J - V$) and the provided power – voltage ($P - V$) characteristics of the Schottky barrier solar cell based on CIGS with platinum (Pt) anode metal ($\phi_m = 6.35 eV$), under the AM1.5 standard spectrum and $T = 300^{\circ}K$. The cell thickness is $d = 1.2 \mu m$ and the doping concentration of the CIGS base layer is $N_d = 7 \times 10^{15} cm^{-3}$. Case (a) of Figure IV.7 corresponds to the sample (A), case (b) of Figure IV.7 corresponds to the sample (B). The photovoltaic output parameters of the cell (samples A and B) are also shown on Figure IV.7 and Table IV.3.

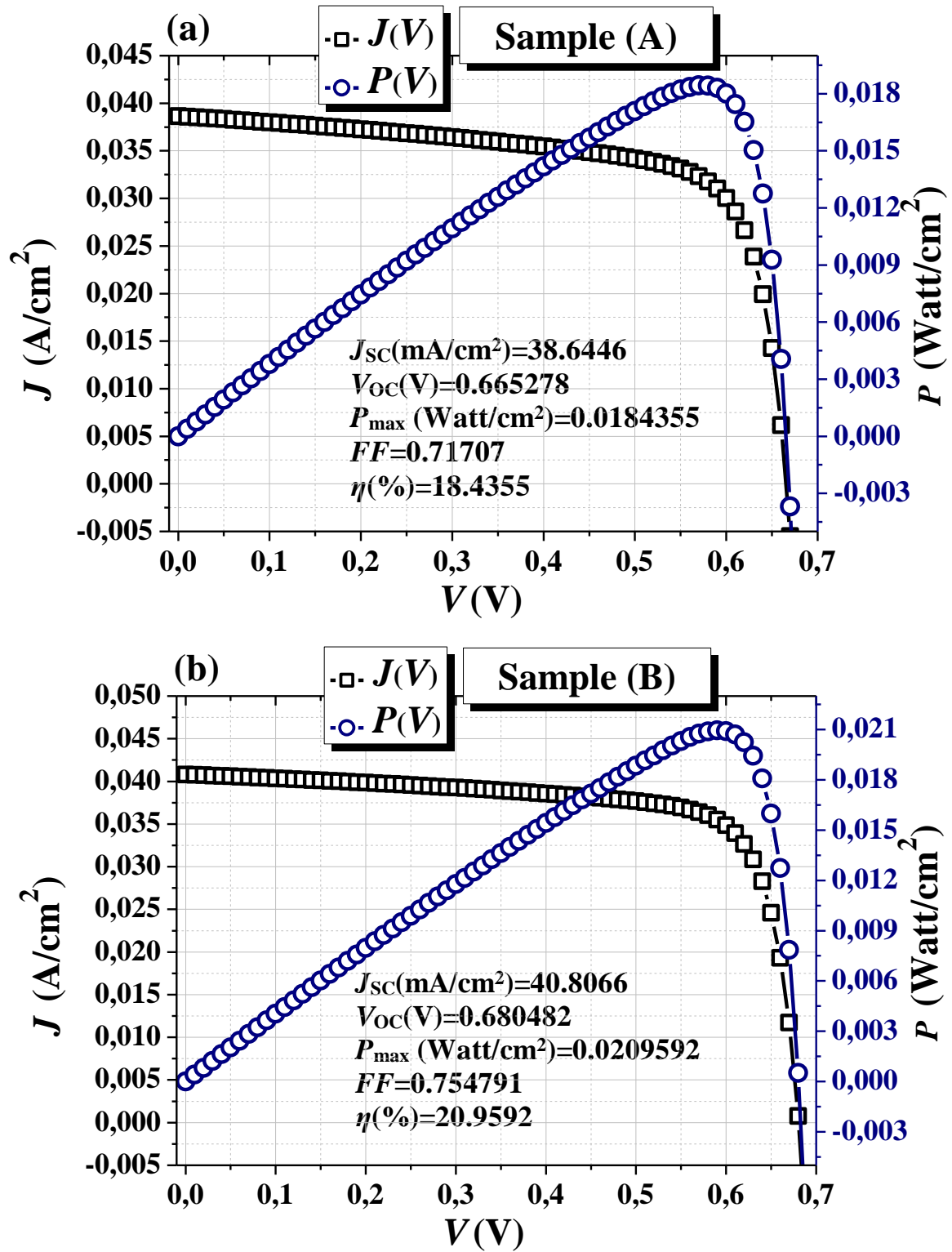


Figure IV.7: Simulated $J - V$ and $P - V$ characteristics of the Schottky barrier solar cell based on CIGS with platinum (Pt) anode metal ($\phi_m = 6.35 \text{ eV}$), under the AM1.5 standard spectrum and $T = 300^\circ\text{K}$: (a) sample (A), (b) sample (B).

Table IV.3: Comparison between the photovoltaic output parameters of the samples (A) and (B) of the simulated Schottky barrier solar cell based on CIGS with platinum (Pt) anode metal ($\phi_m = 6.35 eV$).

Cell	J_{sc} (mA/cm ²)	V_{oc} (V)	P_{max} (Watt/cm ²)	FF	η (%)
Sample (A)	38.64	0.6652	0.01	0.71	18.43
Sample (B)	40.80	0.6804	0.02	0.75	20.95

We notify an enhancement in the photovoltaic output parameters of the sample (B) relatively to the sample (A). Indeed, the J_{sc} is improved from $\sim 38.64 \text{ mA/cm}^2$ to 40.80 mA/cm^2 , the V_{oc} is improved from $\sim 0.66 \text{ V}$ to $\sim 0.68 \text{ V}$, the FF is enhanced from ~ 0.71 to ~ 0.754 and the conversion efficiency η is enhanced from $\sim 18.43 \%$ to $\sim 20.95 \%$. This performance improvement of the sample (B) relatively to sample (A) is related to the $\frac{x_{tot}}{d}$ ratio where $x_{tot} = 2\mu m$ is the total width of the cell and d is the cell thickness. When the $\frac{x_{tot}}{d}$ ratio is significant ($\frac{x_{tot}}{d} > 1$), this favours the performance enhancement of the sample (B) relatively to the sample (A). In the opposite case when the $\frac{x_{tot}}{d}$ ratio is less significant ($\frac{x_{tot}}{d} < 1$), this favours the performance enhancement of the sample (A) relatively to the sample (B). This is clearly showed in Figure IV.8 and Table IV.4.

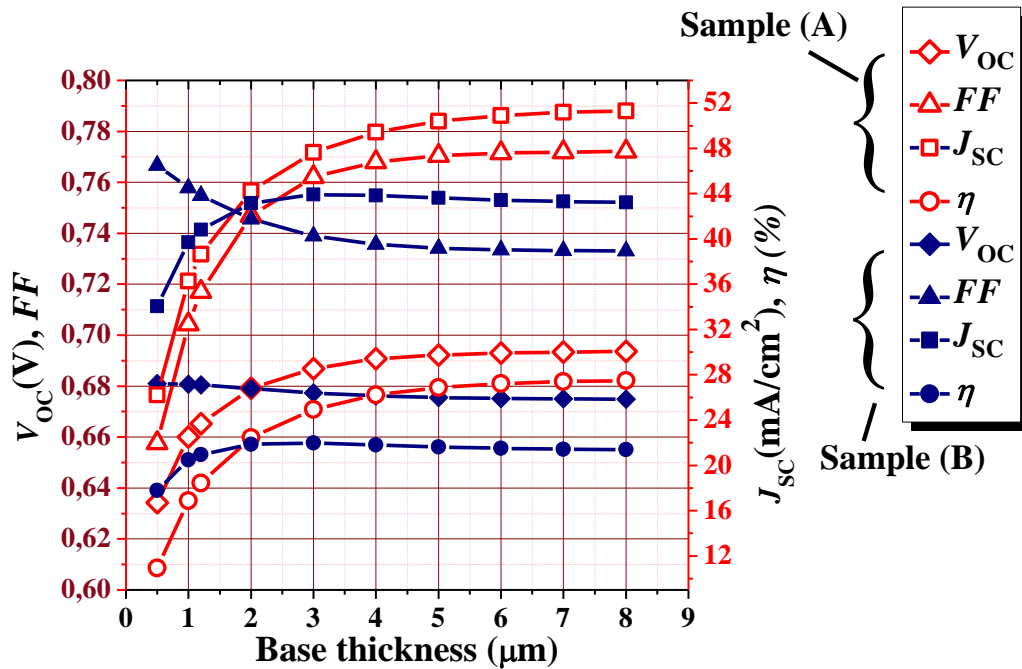


Figure IV.8: Photovoltaic output parameters evolution with the cell thickness increase for the two samples (A) and (B) of the simulated Schottky barrier solar cell based on CIGS.

Table IV.4: Photovoltaic output parameters evolution with the cell thickness increase for the two samples (A) and (B) of the simulated Schottky barrier solar cell based on CIGS.

Thickness (μm)		J_{sc} (mA/cm^2)	V_{oc} (V)	FF	η (%)
0.5	Sample (A)	26,2133	0,63429	0,65763	10,9344
	Sample (B)	34,0605	0,68097	0,76662	17,7811
1	Sample (A)	36,2876	0,66007	0,70427	16,8687
	Sample (B)	39,691	0,68068	0,75785	20,4748
1.2	Sample (A)	38,6446	0,66528	0,71707	18,4355
	Sample (B)	40,8066	0,68048	0,75479	20,9592
2	Sample (A)	44,2454	0,67922	0,74688	22,4454
	Sample (B)	43,1632	0,67908	0,74558	21,8538
3	Sample (A)	47,6519	0,68683	0,76211	24,9427
	Sample (B)	43,9183	0,67729	0,73897	21,9809
4	Sample (A)	49,4263	0,69071	0,76791	26,2158
	Sample (B)	43,8485	0,67614	0,73567	21,8111
5	Sample (A)	50,3843	0,69224	0,7705	26,8735
	Sample (B)	43,6199	0,67549	0,73414	21,6315
6	Sample (A)	50,8999	0,693	0,77153	27,2149
	Sample (B)	43,4283	0,67515	0,73347	21,5056
7	Sample (A)	51,1741	0,69338	0,77194	27,3908
	Sample (B)	43,3026	0,67497	0,73317	21,429
8	Sample (A)	51,3177	0,69356	0,77209	27,4802
	Sample (B)	43,2284	0,67487	0,73307	21,3865

These latter display the photovoltaic output parameters evolution with the cell thickness increase in the range [0.5- 8 μm] where the total width of the cell (x_{tot}) is kept fixed to 2 μm ($x_{tot} = 2\mu\text{m}$) for both samples (A and B). The optimal conversion efficiency η is around 21,98% for the sample (B) with thickness of $d \sim 3\mu\text{m}$, for the sample (A) however, the better η is around 27,48 % for a thickness more larger ($d \sim 8 \mu\text{m}$).

Figure IV.9 and Table IV.5 show the n-type doping concentration effect of the CIGS base layer (N_d) in the range [$10^{12} - 10^{19}\text{cm}^{-3}$] with the cell thickness d of 1.2 μm and platinum (Pt) anode metal ($\phi_m = 6.35 \text{ eV}$) for the two samples (A) and (B) of the simulated Schottky barrier solar cell.

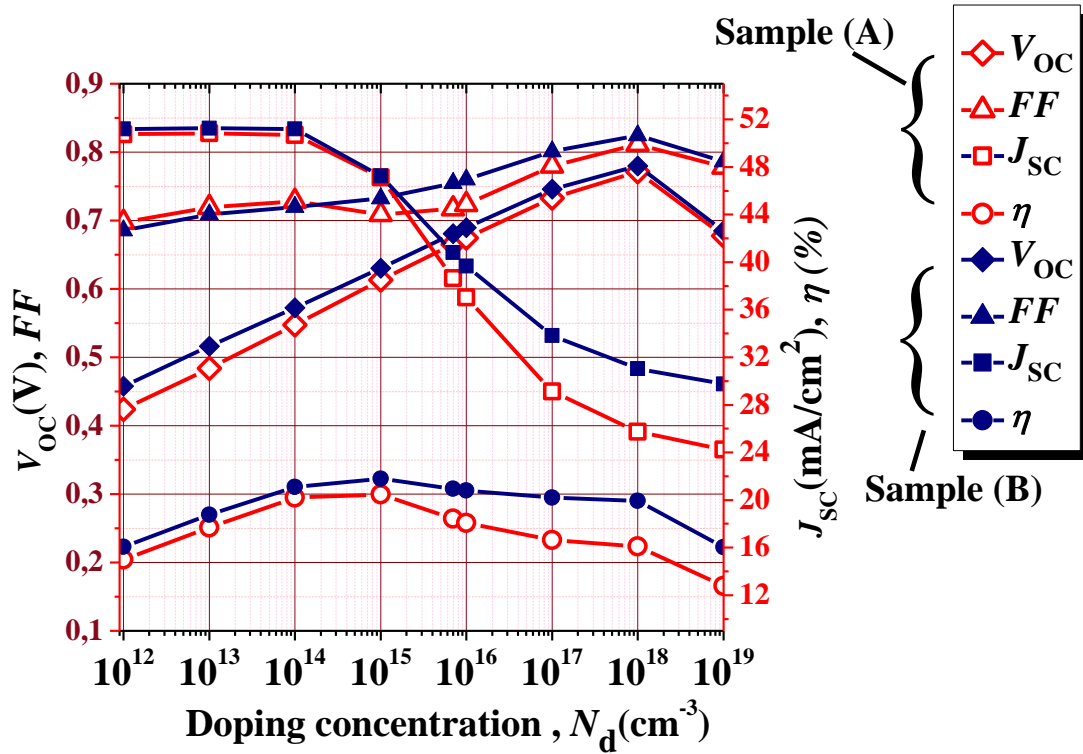


Figure IV.9: Doping concentration effect of the CIGS base layer on the photovoltaic output parameters of the simulated Schottky barrier solar cell with (Pt) anode metal for the two samples (A) and (B).

Table IV.5: Doping concentration effect of the CIGS base layer on the photovoltaic output parameters of the simulated Schottky barrier solar cell with (Pt) anode metal for the two samples (A) and (B).

Doping, $N_d (cm^{-3})$		$J_{sc} (mA/cm^2)$	$V_{oc} (V)$	FF	$\eta (%)$
10^{12}	Sample (A)	50,7622	0,4238	0,69733	15,0017
	Sample (B)	51,2028	0,45767	0,6853	16,0593
10^{13}	Sample (A)	50,8265	0,48389	0,7195	17,6956
	Sample (B)	51,2447	0,51629	0,70903	18,759
10^{14}	Sample (A)	50,6775	0,54759	0,72834	20,2118
	Sample (B)	51,1904	0,57261	0,71959	21,0926
10^{15}	Sample (A)	47,1208	0,61302	0,70903	20,4812
	Sample (B)	47,2438	0,63028	0,73215	21,8013
10^{16}	Sample (A)	37,0309	0,67467	0,72367	18,0801
	Sample (B)	39,6814	0,68975	0,75992	20,7994
10^{17}	Sample (A)	29,1125	0,73267	0,7797	16,6308
	Sample (B)	33,8161	0,7457	0,80107	20,2004
10^{18}	Sample (A)	25,7314	0,77122	0,81161	16,1062
	Sample (B)	31,0336	0,77948	0,82427	19,9392
10^{19}	Sample (A)	24,2496	0,67758	0,77803	12,7837
	Sample (B)	29,7582	0,68503	0,78639	16,0307

The optimal value of doping is about $N_d \cong 10^{15} \text{ cm}^{-3}$ which gives a conversion efficiency $\eta \cong 20/48\%$ for sample (A) and $\eta \cong 21.80\%$ for sample (B). The V_{oc} is significantly enhanced from $\sim 0.42 \text{ V}$ to 0.77 V for sample (A) and from $\sim 0.45 \text{ V}$ to $\sim 0.78 \text{ V}$ for sample (B) as the doping concentration increases from 10^{12} cm^{-3} to 10^{18} cm^{-3} .

For the solar cell, V_{oc} can be derived by setting the net current density (J) to zero and is given by :

$$V_{oc} = \frac{nk_B T}{q} \ln \left(\frac{J_{sc}}{J_s} + 1 \right) \text{ at } J = 0 \quad (\text{IV.5})$$

From the above equation (Eq.(IV.5)), it is clear that open circuit voltage depends on J_s (the saturation current density) and J_{sc} , (the short circuit current density). J_s in the solar cell may be limited by diffusion, recombination or thermionic emission [87]. So, V_{oc} is a measure of the amount of the dominant mechanism in the solar cell (diffusion, recombination or thermionic emission).

Usually for the Schottky barrier solar cell, V_{oc} is dependent on the Schottky barrier height (ϕ_B) through the reverse bias saturation current density J_s which is limited by thermionic emission:

$$J_s = A^* T^2 \exp \left(-\frac{\phi_B}{k_B T} \right) \quad (\text{IV.6})$$

where A^* is the effective Richardson constant for the semiconductor. For n-type CIGS, $A^* = 23.7 A \text{ cm}^{-2} \text{ K}^{-2}$ [82].

But we can see from Figure IV.9 and Table IV.5 that an increase in doping levels results in larger open circuit voltage and smaller short circuit current. This means that V_{oc} is noticeably dependent on the doping levels which can occur only if the Schottky barrier solar cell behaves as an ideal p⁺-n junction diode in the voltage range of solar cell operation [88]. This is satisfied when the Schottky barrier height is high enough which is the case with the Pt as anode metal. Indeed, the high work function of the anode ($\phi_m = 6.35 \text{ eV}$), relatively to the electronic affinity of the n-type CIGS ($\chi_{sc} = 4.8 \text{ eV}$), ensures the establishment of a Schottky barrier relatively high at the semiconductor surface such as:

$$\phi_B = \phi_m - \chi_{sc} = 1.55 \text{ eV} \quad (\text{IV.7})$$

With this structure it is possible to produce minority carrier dominated diodes with the appropriate type of semiconductor and metal contact which are chosen [88]. This means the dark current approaching the ideal value with a saturation current density J_s limited by diffusion.

So if the doping density increases the saturation current density J_S will decrease according to Eq.(IV.8) and hence V_{oc} increases according to Eq.(IV.5).

$$J_S = qn_i^2 \left(\frac{1}{N_A} \sqrt{\frac{D_n}{\tau_n}} + \frac{1}{N_D} \sqrt{\frac{D_p}{\tau_p}} \right) \quad (IV.8)$$

This means that the limiting open circuit voltages reached in such a structure are those of ideal p⁺-n junctions and their characteristics are determined solely by the base layer (n-type CIGS) properties and do not depend critically on the barrier height (ϕ_B) at the metal/semiconductor interface. Hence V_{oc} is determined only by the saturation current J_S given by Eq.(IV.8). Once the minority carrier Schottky barrier solar cell is obtained, the limiting open circuit voltage reached is that of ideal p-n junctions. Its characteristics are determined solely by the base layer bulk properties and do not depend critically on the barrier height at the metal/semiconductor interface. In other words, the dominant current is governed by the transport properties in the semiconductor via drift-diffusion of minority carriers.

Unfortunately the drawback for higher doping density is the decrease in short circuit current density J_{SC} due to the decrease in the minority carrier diffusion length L_D [88].

Figure IV.10 and Table IV.6 show the n-type doping concentration effect of the CIGS base layer (N_d) in the range $[10^{12} - 10^{19} \text{ cm}^{-3}]$ with the cell thickness d of $1.2 \mu\text{m}$ for the sample (B) of the simulated Schottky barrier solar cell. Three cases are taken into account for comparison where the anode metal is respectively: Pt ($\phi_m = 6.35 \text{ eV}$), Au ($\phi_m = 5.47 \text{ eV}$) and Ni ($\phi_m = 5.22 \text{ eV}$). As the anode metal work function (ϕ_m) decreases, we notice that V_{oc} becomes less dependent on the doping levels and do not show a significant increase with the doping density augmentation. This means that, as the anode metal work function (ϕ_m) decreases, the Schottky barrier height decreases as well, and V_{oc} becomes more limited by the barrier height at the metal/semiconductor interface through the saturation current density J_S which will be limited by thermionic emission rather than diffusion. Consequently, with the first choice of Pt as anode metal, the Schottky barrier height is high enough to reduce the thermionic emission and gives a very low saturation current limited by diffusion so that the cell approaches the ideal case of p⁺-n junction where the dominant mechanism in the solar cell is drift-diffusion of minority carriers. The second choice of Au as anode metal can present an example of a standard Schottky barrier solar cell where the transport properties are moderately limited by the barrier height effect at the metal/semiconductor interface and thermionic emission. That is to say such barrier height ensures a low saturation current even if this latter is limited by thermionic emission.

The optimal conversion efficiency reached in that case is typical to Schottky barrier solar cell, and is about $\eta \cong 9.63\%$ for doping density $N_d \cong 10^{14} \text{ cm}^{-3}$. However, the third choice of Ni as anode metal is the worst choice for the Schottky barrier solar cell operation because it establishes a low barrier height at the metal/semiconductor interface which gives, via thermionic emission, a saturation current relatively high. This latter will reduce significantly the solar cell performances.

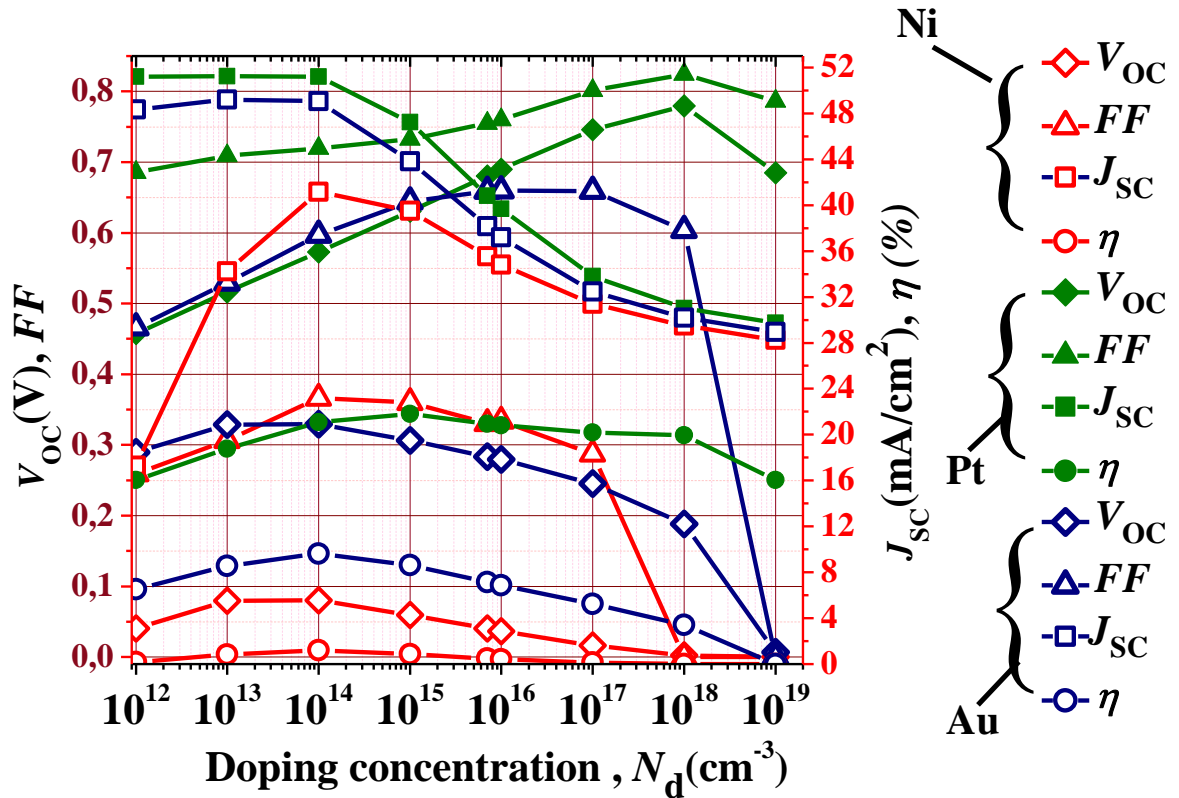


Figure IV.10: Doping concentration effect of the CIGS base layer on the photovoltaic output parameters of the simulated Schottky barrier solar cell (sample B) for three cases of the anode metal: Pt ($\phi_m = 6.35 \text{ eV}$), Au ($\phi_m = 5.47 \text{ eV}$) and Ni ($\phi_m = 5.22 \text{ eV}$).

Table IV.7 gives an estimation of the thermionic emission current density (J_{th}) versus the Schottky barrier height ($\phi_B = \phi_m - \chi_{sc}$) at $T = 300^\circ\text{K}$ according to Eq. (IV.6).

Table IV.6: Doping concentration effect of the CIGS base layer on the photovoltaic output parameters of the simulated Schottky barrier solar cell (sample B) for three cases of the anode metal: Pt ($\phi_m = 6.35 \text{ eV}$), Au ($\phi_m = 5.47 \text{ eV}$) and Ni ($\phi_m = 5.22 \text{ eV}$).

Doping, $N_d(\text{cm}^{-3})$		$J_{sc}(\text{mA}/\text{cm}^2)$	$V_{oc}(V)$	FF	$\eta (\%)$
10^{12}	Pt ($\phi_m = 6.35 \text{ eV}$)	51,2028	0,45767	0,6853	16,0539
	Au ($\phi_m = 5.47 \text{ eV}$)	48,3562	0,28949	0,46596	6,52291
	Ni ($\phi_m = 5.22 \text{ eV}$).	17,2747	0,04025	0,25936	0,18034
10^{13}	Pt ($\phi_m = 6.35 \text{ eV}$)	51,2447	0,51629	0,70903	18,759
	Au ($\phi_m = 5.47 \text{ eV}$)	49,1914	0,32891	0,52933	8,5644
	Ni ($\phi_m = 5.22 \text{ eV}$).	34,216	0,07974	0,30635	0,83585
10^{14}	Pt ($\phi_m = 6.35 \text{ eV}$)	51,1904	0,57261	0,71959	21,0926
	Au ($\phi_m = 5.47 \text{ eV}$)	49,0572	0,32902	0,59698	9,63585
	Ni ($\phi_m = 5.22 \text{ eV}$).	41,1578	0,0804	0,36626	1,21195
10^{15}	Pt ($\phi_m = 6.35 \text{ eV}$)	47,2438	0,63028	0,73215	21,8013
	Au ($\phi_m = 5.47 \text{ eV}$)	43,8194	0,30618	0,6438	8,63758
	Ni ($\phi_m = 5.22 \text{ eV}$).	39,4942	0,05951	0,35986	0,84573
10^{16}	Pt ($\phi_m = 6.35 \text{ eV}$)	39,6814	0,68975	0,75992	20,7994
	Au ($\phi_m = 5.47 \text{ eV}$)	37,2028	0,27941	0,65936	6,85395
	Ni ($\phi_m = 5.22 \text{ eV}$).	34,8286	0,03671	0,33356	0,42647
10^{17}	Pt ($\phi_m = 6.35 \text{ eV}$)	33,8161	0,7457	0,80107	20,2004
	Au ($\phi_m = 5.47 \text{ eV}$)	32,4716	0,24555	0,65909	5,25513
	Ni ($\phi_m = 5.22 \text{ eV}$).	31,3864	0,01612	0,28758	0,14549
10^{18}	Pt ($\phi_m = 6.35 \text{ eV}$)	31,0336	0,77948	0,82427	19,9392
	Au ($\phi_m = 5.47 \text{ eV}$)	30,2042	0,18818	0,60383	3,43207
	Ni ($\phi_m = 5.22 \text{ eV}$).	29,4965	0,0025	0	0
10^{19}	Pt ($\phi_m = 6.35 \text{ eV}$)	29,7582	0,68503	0,78639	16,0307
	Au ($\phi_m = 5.47 \text{ eV}$)	28,9369	0,00654	0	0
	Ni ($\phi_m = 5.22 \text{ eV}$).	28,255	$1,15 \times 10^{-5}$	0	0

Table IV.7: Estimation of the thermionic emission current density (J_{th}) versus the Schottky barrier height (ϕ_B)

Anode metal	Barrier height ($\phi_B = \phi_m - \chi_{sc}$)	Thermionic emission current density, $J_{th} (\text{A}/\text{cm}^2)$
Pt ($\phi_m = 6.35 \text{ eV}$)	1.55 eV	$\cong 2 \times 10^{-20}$
Au ($\phi_m = 5.47 \text{ eV}$)	0.67 eV	$\cong 1.2 \times 10^{-5}$
Ni ($\phi_m = 5.22 \text{ eV}$).	0.42 eV	$\cong 0.19$

IV.5.Conclusion:

In this study, we have investigated the Schottky barrier solar cell based on n-type Copper Indium Gallium Selenide (Cu(In,Ga)Se₂ : CIGS) material, exposed to the AM1.5 standard spectrum at ambient temperature (300°K°).The investigation was carried out using the numerical simulation software SILVACO-ATLAS, which allows the calculation of all the internal parameters of the solar cell such as the distribution of the band diagram, the electron and holes concentrations...etc. The external parameters are also be calculated such as the current density-voltage ($J - V$) and the provided power – voltage ($P - V$) characteristics under illumination, which allow the extraction of the photovoltaic output parameters of the solar cell namely the short circuit current density J_{sc} , the open circuit voltage V_{oc} , the fill factor FF , the maximum power P_{max} provided by the cell and the photovoltaic conversion efficiency η of the cell.

Two solar cells were investigated in this study; for the first one (sample A), the cathode is situated on the bottom of the cell giving a sandwich configuration. For the second one (sample B), the two cathode electrodes are located on the top of the cell giving a coplanar configuration. For both samples of the cell, the anode metal, situated on the top of the cell, should have a work function (ϕ_m) higher than the electron affinity (χ_{sc}) of the semiconductor (n-type CIGS) to form Schottky contact with significant Schottky barrier height. The metals used in this study to satisfy this condition were respectively Pt ($\phi_m = 6.35 eV$), Au ($\phi_m = 5.47 eV$) and Ni ($\phi_m = 5.22 eV$). However, the cathode (Al) is defined to be neutral (Ohmic contact).

An improvement was notified in the photovoltaic output parameters of the sample (B) relatively to the sample (A) for the cell thickness = $1.2 \mu m$, a doping concentration of the CIGS base layer $N_d = 7 \times 10^{15} cm^{-3}$, and platinum (Pt) as anode metal ($\phi_m = 6.35 eV$). Indeed, the J_{sc} is improved from $\sim 38.64 mA/cm^2$ to $40.80 mA/cm^2$, the V_{oc} is improved from $\sim 0.66 V$ to $\sim 0.68 V$, the FF is enhanced from ~ 0.71 to ~ 0.754 and the conversion efficiency η is enhanced from $\sim 18.43 \%$ to $\sim 20.95 \%$. This performance improvement of the sample (B) relatively to sample (A) is related to the $\frac{x_{tot}}{d}$ ratio where $x_{tot} = 2 \mu m$ is the total width of the cell and d is the cell thickness. When the $\frac{x_{tot}}{d}$ ratio is significant ($\frac{x_{tot}}{d} > 1$), this favours the performance enhancement of the sample (B) relatively to the

sample (A). In the opposite case when the $\frac{x_{tot}}{d}$ ratio is less significant ($\frac{x_{tot}}{d} < 1$), this favours the performance enhancement of the sample (A) relatively to the sample (B).

The cell thickness increase in the range [0.5- 8 μ m] shows an optimal conversion efficiency η around 21,98% for the sample (B) with thickness of $d \sim 3\mu$ m, for the sample (A) however, the better η is around 27,48 % for a thickness more larger ($d \sim 8 \mu$ m).

The doping concentration effect of the CIGS base layer (N_d) in the range [$10^{12} - 10^{19}cm^{-3}$], with the cell thickness d of 1.2 μ m and platinum (Pt) anode metal ($\phi_m = 6.35 eV$), shows that the optimal value of doping is about $N_d \cong 10^{15}cm^{-3}$ which gives a conversion efficiency $\eta \cong 20/48\%$ for sample (A), and $\eta \cong 21.80\%$ for sample (B). The V_{oc} is significantly enhanced from $\sim 0.42 V$ to $0.77 V$ for sample (A) and from $\sim 0.45 V$ to $\sim 0.78 V$ for sample (B) as the doping concentration increases from $10^{12}cm^{-3}$ to $10^{18}cm^{-3}$.

V_{oc} is a measure of the amount of the dominant mechanism in the solar cell (diffusion, recombination or thermionic emission). For that purpose, three cases of the anode metal were taken into account for comparison: Pt ($\phi_m = 6.35 eV$), Au ($\phi_m = 5.47 eV$) and Ni ($\phi_m = 5.22 eV$) in sample (B) as example. With the first choice of Pt as anode metal, the Schottky barrier height is high enough ($\phi_B = 1.55 eV$) to reduce the thermionic emission and gives a very low saturation current limited by diffusion so that the cell approaches the ideal case of p⁺-n junction where the dominant mechanism in the solar cell is drift-diffusion of minority carriers. The second choice of Au, as anode metal, has presented an example of a standard Schottky barrier solar cell where the transport properties are moderately limited by the barrier height effect at the metal/semiconductor interface and thermionic emission. That is to say such barrier height ($\phi_B = 0.67 eV$) provides a low saturation current even if this latter is limited by thermionic emission. The optimal conversion efficiency reached in that case is typical to Schottky barrier solar cell, and is about $\eta \cong 9.63\%$ for doping density $N_d \cong 10^{14}cm^{-3}$. The third choice of Ni, as anode metal however, is the worst choice for the Schottky barrier solar cell operation because it establishes a low barrier height ($\phi_B = 0.42 eV$) at the metal/semiconductor interface which gives, via thermionic emission, a saturation current relatively high. This latter has reduced significantly the solar cell performances.

General conclusion

General conclusion

Among the thin-film solar cell technology, the Copper Indium Gallium Selenide, Cu(In,Ga)Se_2 , (CIGS) photovoltaic cell has a preeminent pace both in the current photovoltaic industry and at the research level. Such cells have already achieved high efficiencies of 23.3% and are attractive for use in photovoltaic technology because of their band gap, which has a value near optimal and the broad choice of hetero-junctive partners available, allowing additional degrees of freedom for optimizing performance. The extensive study of CIGS to date has revealed many of their properties and characteristics. The most important are the thickness of the cell, which is flexible, resulting in cost reduction because of the use of less material and their tunable energy-gap, which enables the efficient exploitation of different parts of the solar spectrum, yielding high record efficiencies among photovoltaic cells to date.

In this study, we have investigated the Schottky barrier solar cell based on n-type Copper Indium Gallium Selenide (Cu(In,Ga)Se_2 : CIGS) material, exposed to the AM1.5 standard spectrum at ambient temperature (300°K°). The investigation was carried out using the numerical simulation software SILVACO-ATLAS, which allows the calculation of all the internal parameters of the solar cell such as the distribution of the band diagram, the electron and holes concentrations...etc. The external parameters are also be calculated such as the current density-voltage ($J - V$) and the provided power – voltage ($P - V$) characteristics under illumination, which allow the extraction of the photovoltaic output parameters of the solar cell namely the short circuit current density J_{sc} , the open circuit voltage V_{oc} , the fill factor FF , the maximum power P_{max} provided by the cell and the photovoltaic conversion efficiency η of the cell.

Two solar cells were investigated in this study; for the first one (sample A), the cathode is situated on the bottom of the cell giving a sandwich configuration. For the second one (sample B), the two cathode electrodes are located on the top of the cell giving a coplanar configuration. For both samples of the cell, the anode metal, situated on the top of the cell, should have a work function (ϕ_m) higher than the electron affinity (χ_{sc}) of the semiconductor (n-type CIGS) to form Schottky contact with significant Schottky barrier height. The metals used in this study to satisfy this condition were respectively Pt ($\phi_m =$

6.35 eV), Au ($\phi_m = 5.47$ eV) and Ni ($\phi_m = 5.22$ eV). However, the cathode (Al) is defined to be neutral (Ohmic contact).

An improvement was notified in the photovoltaic output parameters of the sample (B) relatively to the sample (A) for the cell thickness = $1.2 \mu m$, a doping concentration of the CIGS base layer $N_d = 7 \times 10^{15} cm^{-3}$, and platinum (Pt) as anode metal ($\phi_m = 6.35$ eV). Indeed, the J_{sc} is improved from ~ 38.64 mA/cm² to 40.80 mA/cm², the V_{oc} is improved from ~ 0.66 V to ~ 0.68 V, the FF is enhanced from ~ 0.71 to ~ 0.754 and the conversion efficiency η is enhanced from ~ 18.43 % to ~ 20.95 %. This performance improvement of the sample (B) relatively to sample (A) is related to the $\frac{x_{tot}}{d}$ ratio where $x_{tot} = 2 \mu m$ is the total width of the cell and d is the cell thickness. When the $\frac{x_{tot}}{d}$ ratio is significant ($\frac{x_{tot}}{d} > 1$), this favours the performance enhancement of the sample (B) relatively to the sample (A). In the opposite case when the $\frac{x_{tot}}{d}$ ratio is less significant ($\frac{x_{tot}}{d} < 1$), this favours the performance enhancement of the sample (A) relatively to the sample (B).

The cell thickness increase in the range [0.5- $8 \mu m$] shows an optimal conversion efficiency η around 21,98% for the sample (B) with thickness of $d \sim 3 \mu m$, for the sample (A) however, the better η is around 27,48 % for a thickness more larger ($d \sim 8 \mu m$).

The doping concentration effect of the CIGS base layer (N_d) in the range [$10^{12} - 10^{19} cm^{-3}$], with the cell thickness d of $1.2 \mu m$ and platinum (Pt) anode metal ($\phi_m = 6.35$ eV), shows that the optimal value of doping is about $N_d \cong 10^{15} cm^{-3}$ which gives a conversion efficiency $\eta \cong 20.48\%$ for sample (A), and $\eta \cong 21.80\%$ for sample (B). The V_{oc} is significantly enhanced from ~ 0.42 V to 0.77 V for sample (A) and from ~ 0.45 V to ~ 0.78 V for sample (B) as the doping concentration increases from $10^{12} cm^{-3}$ to $10^{18} cm^{-3}$.

V_{oc} is a measure of the amount of the dominant mechanism in the solar cell (diffusion, recombination or thermionic emission). For that purpose, three cases of the anode metal were taken into account for comparison: Pt ($\phi_m = 6.35$ eV), Au ($\phi_m = 5.47$ eV) and Ni ($\phi_m = 5.22$ eV) in sample (B) as example. With the first choice of Pt as anode metal, the Schottky barrier height is high enough ($\phi_B = 1.55$ eV) to reduce the thermionic emission and gives a very low saturation current limited by diffusion so that the cell approaches the ideal case of p⁺-n junction where the dominant mechanism in the solar cell is drift-

diffusion of minority carriers. The second choice of Au, as anode metal, has presented an example of a standard Schottky barrier solar cell where the transport properties are moderately limited by the barrier height effect at the metal/semiconductor interface and thermionic emission. That is to say such barrier height ($\phi_B = 0.67 \text{ eV}$) provides a low saturation current even if this latter is limited by thermionic emission. The optimal conversion efficiency reached in that case is typical to Schottky barrier solar cell, and is about $\eta \cong 9.63\%$ for doping density $N_d \cong 10^{14} \text{ cm}^{-3}$. The third choice of Ni, as anode metal however, is the worst choice for the Schottky barrier solar cell operation because it establishes a low barrier height ($\phi_B = 0.42 \text{ eV}$) at the metal/semiconductor interface which gives, via thermionic emission, a saturation current relatively high. This latter has reduced significantly the solar cell performances.

References

- [1] M. Bronzoni, L. Colace, A. De Iacovo, A. Laudani, G. M. Lozito, V. Lucaferri, M. Radicioni, and S. Rampino, "Equivalent circuit model for Cu(In,Ga)Se₂ solar cells operating at different temperatures and irradiance," *Electronics*, vol. 7, no. 11, 2018.
- [2] Gregory M Wilson et al, The 2020 photovoltaic technologies roadmap, *J. Phys. D: Appl. Phys.* 53 493001(2020).
- [3] Abou-Ras D et al 2017 Innovation highway: breakthrough milestones and key developments in chalcopyrite photovoltaics from a retrospective viewpoint *Thin Solid Films* 633 2–12
- [4] Solar Frontier Achieves: World Record Thin-Film Solar Cell Efficiency of 23.35%. http://www.solar-frontier.com/eng/news/2019/0117_press.html.
- [5] P. Jackson, R. Wuerz, D. Hariskos, E. Lotter, W. Witte, and M. Powalla, Effects of heavy alkali elements in Cu(In,Ga)Se₂ solar cells with efficiencies up to 22.6%, *Phys. Status Solidi RRL* 10, 583 (2016).
- [6]: Amina Benslim, Amjad Meftah, Madani Labed, Afak Meftah, Nouredine Sengouga, Study and optimization of InGaNSchottky solar cell performance, *Optik - International Journal for Light and Electron Optics* 247 (2021) 167984
- [7] P. Hersch and K. Zweibel, "Basic photovoltaic principles and methods (No. SERI/SP-290-1448), Solar Energy Research Inst., Golden, CO (USA), pp: 9, 1982.
- [8] S. Sharma, K. K. Jain and A. Sharma, "Solar cells: in research and applications— a review", *Materials Sciences and Applications*, 6(12), 1145, 2015.
- [9] Kai Maraun and Akane Yamiya. Solar Frontier Achieves World Record Thin-Film Solar Cell Efficiency: 22.3 <http://www.solar-frontier.com/eng/news/2015/C051171.html>, December 2015.
- [10] Hu C. PN and Metal-semiconductor Junctions. UC, Berkeley, EE Class Note, Chapter 4.2009. pp. 89-156

- [11] V. Foncrose, « Nanocristaux, films et cellules photovoltaïques de Cu_2ZnSn (S,Se) 4 par impression d'encre », Doctoral dissertation, Université de Toulouse, Université Toulouse III Paul Sabatier, 2015.
- [12] Belalem Abdeldjabar et Sandali Walid, “Simulation d’une cellule solaire photovoltaïque à base de Cu_2ZnSn (S,Se) 4”, these de doctorat, Université de Ouargla, 06/06/2017.
- [13] M. Naidu, Engineering Physics, Pearson Education India, 2009.
- [14] Yousaf Hameed Khattak, Modeling of High Power Conversion Efficiency Thin Film Solar Cells, PhD Thesis (2019), Universitat Politècnica de València.
- [15] P. Jayakumar, “Solar Energy Resource Assessment Handbook”, p 117, September 2009.
- [16] S.S. Li, Semiconductor Physical Electronics, Springer US, Boston, MA, 1993.
doi:10.1007/978-1-4613-0489-0.
- [17] W. Tress, Organic Solar Cells, Springer International Publishing, Cham, 2014.
doi:10.1007/978-3-319-10097-5.
- [18] NREL, *Reference solar spectral irradiance: air mass 1.5*. [Online]. Available: <https://www.nrel.gov/grid/solar-resource/spectra.html> (visited on 06/02/2020).
- [19] Hu, C., and R. M. White. Solar Cells. New York: McGraw Hill, 1983.
- [20] A. Ortiz-Conde, F. García-Sánchez, J. Muci, A. Sucre-González, A review of diode and solar cell equivalent circuit model lumped parameter extraction procedures, Facta Univ. - Ser. Electron. Energ. 27 (2014) 57–102. doi:10.2298/FUEE1401057O.
- [21] P. Salomé. “Chalcogenide Thin Films for Solar Cells: Growth and Properties.” Doctoral dissertation. University of Aveiro, 2011, pp. 1–161. url: <http://hdl.handle.net/10773/3723>.

- [22] André Filipe Ferreira Violas, Novel Rear Contact Architectures in CIGS Solar Cells: Modelling and Experimental Fabrication, Master Dissertation, NOVA School of Science and Technology, NOVA University Lisbon, 2020.
- [23] Y. Tao. "Screen-Printed Front Junction n-Type Silicon Solar Cells." In: Printed Electronics- Current Trends and Applications. 2016, pp. 47–73. doi: 10.5772/63198.
- [24] Rezaei, N. (2020). Opto-electrical modelling of CIGS solar cells, Master Dissertation, Delft University of Technology.
- [25] C. J. Chen, "Physics of solar energy", John Wiley & Sons, 2011.
- [26] A J McEvoy; Luis Castaner; T Markvart, "Solar cells: materials, manufacture and operation", Amsterdam : Academic Press, 2012.
- [27] Asiel Neftalí Corpus Mendoza, Influence of the p-type layer on the performance and stability of thin film silicon solar cells, PhD dissertation, University of Sheffield, 2017.
- [28] Abayomi Stephen, Optimisation of charge carrier mobility and lifetime in silicon nanowire solar cells growth by Plasma Enhanced Chemical Vapour Deposition (PECVD) technique at low temperatures, PhD Dissertation, Emerging Technologies Research Centre De Montfort University, Leicester, UK, 2020.
- [29] D.B. Klaassen. "A Unified Mobility Model for Device Simulation– I. Model Equations and Concentration Dependence" Solid-State Electronics, vol.35, pp.953-959, 1992.
- [30] N.D. Arora, et al, Electron and Hole Mobilities in Silicon as a Function of Concentration and Temperature. IEEE Trans. Electron Devices, vol.29, pp.292-295, 1982.
- [31] D. M. Caughey, et al, Carrier Mobilities in Silicon Empirically Related to Doping and Field. Proc. IEEE, vol.55, pp.2192-2193, 1967.
- [32] V. Chakrapani et al, Semiconductor Junctions, Solid-Solid Junctions. Encyclopaedia of Applied Electrochemistry vol.1, pp. 1882-1887, 2014.
- [33] A. Feroz et al., Influence of Front and Back Contacts on Photovoltaic Performances of PN homo-junction silicon solar cell, International J. of Photo-Energy, pp.1-6, 2017.

- [34]:H. Search, C. Journals, A. Contact, M. Iopscience, C. Phys, I.P. Address, Au / Pt / InGaN / GaN Heterostructure Schottky Prototype Solar Cell, 098102 (2009) 2007–2010. <https://doi.org/10.1088/0256-307X/26/9/098102>.
- [35]: I.M. Dharmadasa, *Advances in Thin-Film Solar Cells, Second Edi*, Jenny Stanford Publishing, Boulevard, 2018. <https://doi.org/10.1201/9780429020841>.
- [36] Solar cells -the three generations, (n.d.).<http://plasticphotovoltaics.org/lc/lcsolarcells/lc-introduction.html>.
- [37] Solar facts and advice, (n.d.).www.solar-facts-and-advice.com/solar-cells.html.
- [38] F.C. Krebs, M. Hösel, M. Corazza, B. Roth, M. V. Madsen, S.A. Gevorgyan, R.R. Søndergaard, D. Karg, M. Jørgensen, *Freely available OPV-The fast way to progress, Energy Technol.* 1 (2013) 378–381. doi:10.1002/ente.201300057.
- [39]R.A Street, *Hydrogenated Amorphous Silicon (Cambridge Solid State Science Series) 1st Edition*, Cambridge University Press. 1991, pp. 238-432,.
- [40]M.A. Green, Y. Hishikawa, W. Warta, E.D. Dunlop, D.H. Levi, J. Hohl-Ebinger, A.W.H. Ho-Baillie, *Solar cell efficiency tables (version 50)*, *Prog. Photovoltaics Res. Appl.* 25 (2017) 668–676. doi:10.1002/pip.2909.
- [41]First Solar website, (n.d.).<http://www.firstsolar.com>.
- [42]White paper for CIGS thinfilm solar cell technology, (n.d.).<http://cigs-pv.net/cigswhite-paper-initiative/>.
- [43]E.S. JüriKrustok, TaaviRaadik, MaarjaGrossberg, Sergio Giraldo, MarkusNeuschitzer, Simon López-Marino, *Temperature dependent electroreflectance study of Cu₂ZnSnS₄ solar cells*, *Mater. Sci. Semicond. Process.* 39 (2015) 251–254. doi:10.1016/j.mssp.2015.04.055.
- [44]C. Persson, *Electronic and optical properties of Cu₂ZnSnS₄ and Cu₂ZnSnSe₄*, *J. Appl. Phys.* 107 (2010) 1–8. doi:10.1063/1.3318468.
- [45]M. Dimitrievska, A. Fairbrother, E. Saucedo, A. Pérez-Rodríguez, V. Izquierdo-Roca, *Influence of compositionally induced defects on the vibrational properties of device*

- grade $\text{Cu}_{0.2}\text{ZnSnSe}_{0.4}$ absorbers for kesterite based solar cells, *Appl. Phys. Lett.* 106 (2015) 1–5. doi:10.1063/1.4913262.
- [46]. J.K. E. Kask, M. Grossberg, R. Josepson, P. Salu, K. Timmo, Defect studies in $\text{Cu}_2\text{ZnSnSe}_4$ and $\text{Cu}_2\text{ZnSn}(\text{Se}_{0.75}\text{S}_{0.25})_4$ by admittance and photoluminescencespectroscopy, *Mater. Sci. Semicond. Process.* 16 (2013) 992–996. doi:10.1016/j.mssp.2013.02.009.
- [47] I.L. Repins, M.J. Romero, J. V. Li, S.-H. Wei, D. Kuciauskas, C.-S. Jiang, C. Beall, C. DeHart, J. Mann, W.-C. Hsu, G. Teeter, A. Goodrich, R. Noufi, Kesterite Successes, Ongoing Work, and Challenges: A Perspective From Vacuum Deposition, *IEEE J. Photovoltaics*. 3 (2013) 439–445. doi:10.1109/JPHOTOV.2012.2215842.
- [48] H. Zhou, W.-C. Hsu, H.-S. Duan, B. Bob, W. Yang, T.-B. Song, C.-J. Hsu, Y. Yang, CZTS nanocrystals: a promising approach for next generation thin film photovoltaics, *Energy Environ. Sci.* 6 (2013) 2822. doi:10.1039/c3ee41627e.
- [49] J.-K.K. and D.-H.K. Kee-Jeong Yang, Dae-Ho Son, Shi-Joon Sung, Jun-Hyoung Sim, Young-Ill Kim, Si-Nae Park, Dong-Hwan Jeon, JungSik Kim, Dae-KueHwang, Chan-Wook Jeon, Dahyun Nam, Hyeonsik Cheong, A band-gap-graded CZTS_{Se} solar cell with 12.3% efficiency, *J. Mater. Chem. A*. 4 (2016) 10151–10158. doi:10.1039/C6TA01558A.
- [50] L.X.J. and F.Y.L. Fang Qin Zeng, Yan Qing Lai, Zi Li Han, Boon K. Ng, ZhiAn Zhang, Hong Liang Zhang, Fabrication of earth-abundant $\text{Cu}_2\text{ZnSn}(\text{S},\text{Se})_4$ light absorbers by a sol-gel and selenization route for thin film solar cells, *RCS Adv.* 6(2016) 6562–6570. doi:10.1039/C5RA18975F.
- [51] Shawn Willis and Oriel College, Advanced Optoelectronic Characterisation of Solar Cells, PhD Dissertation, University of Oxford, 2011.
- [52] Solar Frontier Achieves: World Record Thin-Film Solar Cell Efficiency of 23.35%. http://www.solar-frontier.com/eng/news/2019/0117_press.html.
- [53] P. Jackson, R. Wuerz, D. Hariskos, E. Lotter, W. Witte, and M. Powalla, Effects of heavy alkali elements in $\text{Cu}(\text{In},\text{Ga})\text{Se}_2$ solar cells with efficiencies up to 22.6%, *Phys. Status Solidi RRL* 10, 583 (2016).

- [54] G. Leibfried and N. Breuer, *Point Defects in Metals I: Introduction to the Theory*, Springer Tracts in Modern Physics (Springer-Verlag, New York, 1978).
- [55] C. Freysoldt, B. Grabowski, T. Hickel, J. Neugebauer, G. Kresse, A. Janotti, and C. G. Van de Walle, First-principles calculations for point defects in solids, *Rev. Mod. Phys.* **86**, 253 (2014).
- [56] Miaomiao Han, Peter Deák, Zhi Zeng, and Thomas Frauenheim, Possibility of Doping CuGaSe₂ n-Type by Hydrogen, *Physical Review Applied* **15**, 044021 (2021)
- [57]: Krishna Prasad Aryal, High Efficiency Ultrathin CIGS Solar Cells, PhD thesis, Old Dominion University (2015).
- [58] U. Rau and H. W. Schock, in *Solar Cells: Materials, Manufacture and Operation*, eds. T. Markvart and L. Castaner, Elsevier, Great Britain, (2005).
- [59]: Tom Markvart & Luis Castañer, *Solar Cells: Materials, Manufacture and Operation*, Elsevier (2006)
- [60]: D. Hebert, "Optical characterization of copper indium gallium diselenide thinfilms", Ph.D. thesis, University of Illinois at Urbana-Champaign, (2012).
- [61]: M. Belhadj, T. Tadjer, B. Abbar, Z. Bousahla, B. Bouhafs and H. Aourag, "Structural, electronic and optical calculations of Cu(In,Ga)Se₂ ternary Chalcopyrites", *Phys. Stat. Sol.* **241**, 2516-2528 (2004).
- [62]: H. Schock, "Properties of Chalcopyrite-based Materials and Film Deposition for Thin-Film Solar cells", In: Y. Hamakawa, (eds.), "Thin Film Solar Cells: Next Generation Photovoltaics and its Applications", Springer, Berlin, pp. 106, (2004).
- [63] B. J. Stanbery, "Copper Indium Selenides and Related Materials for Photovoltaic Devices, *Critical Reviews in Solid State and Materials Science* **27**, 73 (2002).

- [64] D. K. Schroder, "Semiconductor Material and Device Characterization", 3rd edition, Wiley, New York, (2006).
- [65] S.-H. Wei, S.B. Zhang, A. Zunger, "Effects of Ga addition to CuInSe₂ on its electronic, structural, and defect properties", *Appl. Phys. Lett.* 72, 3199 (1998).
- [66] N. Amin, "Promises of Cu (In, Ga)Se₂ Thin Film Solar Cells from the Perspective of Material Properties, Fabrication Methods and Current Research Challenges", *J. of Appl. Sci.*, 11; 401-410 (2011).
- [67]: André Filipe Ferreira Violas, Novel Rear Contact Architectures in CIGS Solar Cells: Modelling and Experimental Fabrication, Master Dissertation, NOVA School of Science and Technology, NOVA University Lisbon (2020).
- [68] M. Bodegård, L. Stolt, and J. Hedström. "The influence of sodium on the grain structure of CuInSe₂ films for photovoltaic applications." In: *12th European Photovoltaic Solar Energy Conference*. Amsterdam, The Netherlands, 1994, pp. 1743–1746.
- [69] D. Rudmann, D. Brémaud, A. F. Da Cunha, G. Bilger, A. Strohm, M. Kaelin, H. Zogg, and A. N. Tiwari. "Sodium incorporation strategies for CIGS growth at different temperatures." In: *Thin Solid Films* 480-481 (2005), pp. 55–60. doi: 10.1016/j.tsf.2004.11.071.
- [70] D. Abou-Ras, S. Wagner, B. J. Stanbery, H. W. Schock, R. Scheer, L. Stolt, S. Siebentritt, D. Lincot, C. Eberspacher, K. Kushiya, and A. N. Tiwari. "Innovation highway: Breakthrough milestones and key developments in chalcopyrite photovoltaics from a retrospective viewpoint." In: *Thin Solid Films* 633 (2017), pp. 2–12. doi: 10.1016/j.tsf.2017.01.005.
- [71]: Rezaei, Nasim, Opto-electrical modelling of CIGS solar cells, Master Dissertation, Delft University of Technology (2020).
- [72] J. Trieschmann, S. Ries, N. Bibinov, P. Awakowicz, S. Mráz, J. M. Schneider, and T. Mussenbrock, "Combined experimental and theoretical description of direct current magnetron sputtering of Al by Ar and Ar/N₂ plasma," *Plasma Sources Science and Technology*, vol. 27, no. 5, p. 54 003, 2018.

- [73]: K. Orgassa, H. W. Schock, and J. H. Werner, “Alternative back contact materials for thin film Cu(In,Ga)Se₂ solar cells,” *Thin Solid Films*, vol. 431, pp. 387–391, 2003.
- [74]: J. Shay, S. Wagner, and H. Kasper. “Efficient CuInSe₂/CdS solar cells.” In: *Applied Physics Letters* 27.2 (1975), pp. 89–90. doi: 10.1063/1.88372.
- [75]: R. Scheer and H.-W. Schock. *Chalcogenide photovoltaics: physics, technologies, and thin film devices*. John Wiley & Sons, 2011.
- [76] S. Siebentritt, “Alternative buffers for chalcopyrite solar cells,” *Solar energy*, vol. 77, no. 6, pp. 767–775, 2004.
- [77] S. Lee, E. S. Lee, T. Y. Kim, J. S. Cho, Y. J. Eo, J. H. Yun, and A. Cho, “Effect of annealing treatment on CdS/CIGS thin film solar cells depending on different CdS deposition temperatures,” *Solar Energy Materials and Solar Cells*, vol. 141, pp. 299–308, 2015.
- [78] J. Lindahl, U. Zimmermann, P. Szaniawski, T. Torndahl, A. Hultqvist, P. Salomé, C. Platzer-Björkman, and M. Edoff. “Inline Cu(In,Ga)Se₂ co-evaporation for high-efficiency solar cells and modules.” In: *IEEE Journal of Photovoltaics* 3.3 (2013), pp. 1100–1105. doi: 10.1109/JPHOTOV.2013.2256232.
- [79] about SILVACO. Available from:
<http://www.silvaco.com/company/profile/profile.html>
- [80]: Green, Shawn E., *Interdigitated back-surface-contact solar cell modeling using Silvaco Atlas*, Master dissertation, NAVAL POSTGRADUATE SCHOOL of CALIFORNIA, 2015
- [81]: Semmari Maroua & Atawa Monira, *Study of a Metal- Insulator- Semiconductor (MIS) solar cell*, Master dissertation, University of Biskra, 2021.
- [82]: ATLAS User ’ s Manual, (2015). www.silvaco.com.
- [83]: Amina Benslim, Amjad Meftah, Madani Labed, Afak Meftah, Nouredine Sengouga, *Study and optimization of InGaNSchottky solar cell performance*, *Optik - International Journal for Light and Electron Optics* 247 (2021) 167984

- [84]:Rhoderick, E.H. and R.H. Williams. *Metal-Semiconductor Contacts*, 2nd ed. OxfordScience Publications, 1988.
- [85]. Jeong, M., Solomon, P., Laux, S., Wong, H., and Chidambarro, D., "Comparison of Raised and Schottky Source/Drain MOSFETs Using a Novel Tunneling Contact Model", *Proceedings of IEDM* (1998): 733-736.
- [86]. Matsuzawa, K., K. Uchida, and A. Nishiyama, "A Unified Simulation of Schottky and Ohmic Contacts", *IEEE Trans. Electron Devices*, Vol. 47, No. 1 (Jan. 2000): 103-108.
- [87]O.M. Nielsen, Current mechanism of tunnel m.i.s, solar cells, IEEPROC, Vol. 127, Pt. I, No. 6, December 1980
- [88] ChanchaiVithsupalertB.E., Theory Of Metal-Insulator-Semiconductor (MIS) Solar Cells, Thesis (1977), University of New South Wales.

Abstract

We have investigated a Schottky barrier solar cell based on n-type CIGS material. The anode metal; situated on the top of the cell, satisfy the Schottky contact condition. The cathode (Al), however, is defined to be Ohmic contact. Two samples were investigated; in the sample (A), the cathode is situated on the bottom of the cell, and in sample (B), the two cathode electrodes are located on the top of the cell. With using platinum (Pt) as anode metal ($\phi_m = 6.35 \text{ eV}$), the cell thickness increase in the range $[0.5- 8 \mu\text{m}]$ showed an optimal conversion efficiency η around 21,98% for the sample (B) with thickness $d \sim 3 \mu\text{m}$, for the sample (A), the better η is around 27,48 % for a thickness more larger ($d \sim 8 \mu\text{m}$). The doping concentration effect of the CIGS base layer (N_d) in the range $[10^{12} - 10^{19} \text{ cm}^{-3}]$, with the cell thickness d of $1.2 \mu\text{m}$, showed an optimal value of doping $N_d \cong 10^{15} \text{ cm}^{-3}$ which provided a conversion efficiency $\eta \cong 20.48\%$ for sample (A), and $\eta \cong 21.80\%$ for sample (B). Three choices were considered for the anode metal: Pt ($\phi_m = 6.35 \text{ eV}$), Au ($\phi_m = 5.47 \text{ eV}$) and Ni ($\phi_m = 5.22 \text{ eV}$), showing that the cell approached the ideal case of p⁺-n junction for the first choice. The second choice made the cell operating as standard Schottky barrier solar cell. The third choice, however, was the worst choice because it reduced significantly the solar cell performances.

ملخص

درسنا خلية شمسية ذات حاجز شوتكي مع مادة CIGS مطعمة نوع N. معدن الأنود متموضع على الجهة العليا للخلية و يحقق تماس شوتكي. في حين الكاتود (من Al) معرف على كونه تماس أومي. درسنا عينتين ؛ في العينة (A) الكاتود متموضع على الجهة السفلى للخلية ، و في العينة (B) إلكترودي الكاتود متموضعان على الجهة العليا للخلية. باستخدام البلاتينوم (Pt) كمعدن للأنود ($\phi_m = 6.35 \text{ eV}$) ، زيادة سمك الخلية في المجال $[0.5- 8 \mu\text{m}]$ أظهر قيمة جيدة لمردود التحول الفوتوفولطائي η حول 21,98% من أجل العينة (B) ذات سمك $d \sim 3 \mu\text{m}$ ، من أجل العينة (A) أحسن مردود في حدود 27,48 % مع سمك أكبر $d \sim 8 \mu\text{m}$. تأثير تركيز التطعيم (N_d) لطبقة القاعدة CIGS في المجال $[10^{12} - 10^{19} \text{ cm}^{-3}]$ ، مع سمك الخلية $d = 1.2 \mu\text{m}$ ، أظهر أن أحسن قيمة للتطعيم هي $N_d \cong 10^{15} \text{ cm}^{-3}$ و التي تعطي مردود تحول فوتوفولطائي $\eta \cong 20.48\%$ من أجل العينة (A) ، و $\eta \cong 21.80\%$ من أجل العينة (B). ثلاث اختيارات أخذت بعين الاعتبار من أجل معدن الأنود : Pt ($\phi_m = 6.35 \text{ eV}$) ، Au ($\phi_m = 5.47 \text{ eV}$) ، و Ni ($\phi_m = 5.22 \text{ eV}$) ، و التي أظهرت أن الخلية اقتربت من الحالة المثالية لوصلة p⁺-n من أجل الاختيار الأول. الإختيار الثاني جعل الخلية تشتغل كخلية شمسية معيارية ذات حاجز شوتكي. في حين الاختيار الثالث كان أسوأ إختيار لأنه خفض بشكل معتبر أداء الخلية الشمسية .